Active and passive microrheology to quantify the mechanical properties of biomolecular condensates and the cytoplasm

Magda Giovanna Sánchez Sánchez

Department of Bioengineering

McGill University, Montréal

August, 2024

A thesis submitted to McGill University in partial fulfillment of the requirements of the degree of Master of Engineering in Biological and Biomedical Engineering

Contents

Abstract

Microrheology encompasses techniques that allow scientists to study how soft materials flow and deform over time under the application of micro-scale forces. By examining the movement of micro- or nano-sized probes embedded in the material in response to external and thermal forces, we can deduce the material properties, making it a fundamental technique to study biological materials. There are two main approaches: active, when an external force is applied to the probe particles to deform the material; and passive, when the forces on the probe are only due to thermal fluctuations. Here, we illustrate how the use of passive and active microrheology techniques provide valuable information on the rheological properties of biopolymeric samples. By comparing their application on two samples with different environments and conditions we show that, although the considerations required experimentally in each case differ, the information obtained can be related to the structure and function of the sample. We focus on two biological systems where transient intermolecular interactions result in tunable viscoelastic properties: biomolecular condensates and the eukaryotic cytoplasm.

Biomolecular condensates are formed through liquid-liquid phase separation (LLPS), which is a thermodynamically driven process where a homogeneous aqueous solution divides into two liquid phases, a dense protein rich phase equilibrated with a dilute phase. We focused on mussel foot protein (Mfp) condensates. Marine mussels produce protein-based fibers, called byssal threads, to tightly anchor to surfaces underwater. Due to their stiffness and extensibility, byssal threads are an important model for bio-inspired materials like coatings and adhesives. Current models of byssus production indicate condensation of different adhesive proteins as the mechanism to fabricate and assemble the

adhesive material outside the mussel's body. To elucidate the nature of Mfp condensates rheology, we used an optical trap-based active microrheology approach to investigate the mechanical changes of recombinant mussel foot protein 1 (rMfp-1) condensation triggered by two different anions: chloride and sulfate. In parallel, we performed passive microrheology to validate the active method. We varied the pH from $\sim$ 2-8 to emulate the conditions inside and outside the mussel environment. The rMfp-1 condensates exhibited a behavior described by a Jeffrey's fluid model, where a fluid behaves more fluid-like at low frequencies and more elastic-like at intermediate frequencies, plus an additional elastic term that could come from surface tension effects. We found a proportional relation with the pH and viscosity for both salts and observed that sulfate induced condensates showed a higher viscosity and a slower liquid to solid transition, than condensates formed with chloride.

On the other hand, the cytoplasm contains the cytoskeleton, a set of polymers whose mechanical properties and organization determine the cell's shape and structure. It consists of three filaments: microtubules (MTs), actin, and intermediate filaments; that change their organization in response to mechanical and biochemical signals to modify the cell elasticity and viscosity. Thus, the mechanical properties of the cell can be tuned to allow different processes to take place, such as cellular division, migration, and adhesion. Therefore, alterations of those mechanical properties of the cell significantly impact human health. We aimed to assess the role of microtubule acetylation on the mechanics of the cytoplasm using optical trap-based active microrheology. Acetylation is a post-translational modification known to produce long-lived and stable microtubules Preliminary results showed a decrease in the elasticity across the frequency range studied.

Our results illustrate the advantages of using complementary microrheology techniques to uncover important relations of biological samples *in vitro* and *in vivo*.

Résumé

La microrhéologie englobe les techniques permettant d'étudier la déformation de la matière molle sous l'application de forces à l'échelle microscopique, et constitue donc une technique fondamentale dans l'étude des matériaux biologiques. Ces techniques consistent à mesurer la position de microparticules intégrées dans le matériau étudié pour obtenir leur réponse à des forces externes ou thermiques, ce qui permet d'en déduire les propriétés mécaniques. Il existe deux approches: active, lorsqu'une force externe est appliquée, et passive, lorsque la force provient uniquement des fluctuations thermiques. Dans ce projet, nous montrons qu'indépendamment de la nature de l'échantillon, les deux approches fournissent des informations importantes sur les propriétés rhéologiques des biopolymères qui peuvent être liées à leur structure et à leur fonction. Nous nous concentrons sur deux systèmes biologiques où les interactions intermoléculaires transitoires donnent lieu à des propriétés viscoélastiques accordables: les condensats biomoléculaires et le cytoplasme eucaryote.

Les condensats biomoléculaires sont formés par séparation de phase liquide-liquide, un processus thermodynamique dans lequel une solution homogène se sépare en deux phases en équilibre: une phase dense, riche en protéines, et une phase diluée. Dans le cadre de cette étude, nous nous concentrons sur les condensats de protéines sécrétées par les moules (Mfp). Les moules produisent le byssus, une fibre naturelle composée de filaments protéiques, qui leur permet d'adhérer solidement aux surfaces sous-marines. Le byssus est un modèle important pour les biomatériaux car il est à la fois rigide et extensible. Les modèles de la formation du byssus suggèrent que la condensation des protéines adhésives sécrétées par la moule est un mécanisme important dans son assemblage. Afin de comprendre les propriétés mécaniques des condensats de rMfp-1 formés en présence de chlorure de sodium et de sulfate,

nous avons utilisé la microrhéologie active implémentée avec des pinces optiques. Nous avons ensuite utilisé la microrhéologie passive pour valider la méthode active. Nous avons fait varier le pH entre 2 et 8 pour simuler les conditions internes et externes de la moule. Nous avons constaté que les condensats se comportent selon le modèle rhéologique de Jeffrey plus un terme élastique qui peut être expliqué par la tension de surface. Selon ce modèle, les condensats se comportent comme un liquide à basse fréquence et comme un solide élastique à des fréquences intermédiaires. Nous avons également observé une relation proportionnelle entre le pH et la viscosité pour les deux sels, la présence de sulfate induisant une viscosité plus élevée et une transition plus lente vers le solide par rapport au chlorure de sodium.

D'autre part, le cytoplasme de la cellule contient le cytosquelette, un groupe de polymères qui assure le soutien et l'organisation interne de la cellule. Il se compose de trois filaments: les microtubules, les filaments d'actine et les filaments intermédiaires. Ceux-ci répondent à des signaux mécaniques et biochimiques pour se réorganiser et modifier la viscoélasticité de la cellule. Ainsi, les propriétés mécaniques de la cellule changent pour s'adapter à des processus tels que la division cellulaire, la migration ou l'adhésion. Les altérations de ces propriétés ont donc un impact majeur sur la santé. Dans ce projet, nous utilisons la microrhéologie avec des pinces optiques pour étudier le rôle de l'acétylation, une modification post-traductionnelle contribuant à la stabilité des microtubules, dans la régulation des propriétés mécaniques du cytoplasme. Les résultats préliminaires révèlent une diminution de l'élasticité du cytoplasme aux fréquences étudiées. Nos résultats illustrent les avantages de l'utilisation de techniques complémentaires de microrhéologie pour étudier des relations importantes dans des spécimens biologiques *in vitro* et *in vivo*.

Acknowledgements

First I would like to thank my supervisor Dr. Adam Hendricks, for giving me the opportunity of being part of this program, an invaluable experience that has helped me to grow both academically, and personally. Moreover, I am greatly thankful for his patience, support and encouragement during the academic and personal challenges I faced along my graduate studies, which undoubtedly encouraged me to be able to complete this process successfully.

I also would like to thank all the members of the Hendricks lab, present and past, that besides always offering support with their particular expertise, made the lab a fun and nice space to share laughs, culture and encouragement: Sahil Nagpal, Zhu Liu, Emily Prowse, Brooke Turkalj, Sofia Cruz, Karthikeyan Swaminathan, Samuel Wang, Benjamin Guérin, Lilian Ferotin, Lale Gursu, Chengqian Zhou and Daniel Beaudet. My special gratitude to Hamideh Rezvani for her support and contributions to this project, and for her constant academic and personal inspiration.

I am thankful to all the new friends in Montreal that were always very supportive and filled my journey with incredible moments, offering me a second family. Also to my friends in México, that even in the distance never stopped cheering me. More specially, I thank to my greatest source of support and love in Montreal, Francis Lemyre, who was always for me, in the best and hardest moments, and whose every day motivation was determinant for me to succeed. I deeply thank my family, specially to my little sister Liz, for always being there for me, for their endless love and care, I owe who I am to them.

Finally, I would like to express my gratitude to the different agencies that funded my project and stay in the BBME program: to the Natural Sciences and Engineering Research Council (RGPIN/04608-2020) and New Frontiers in Research Fund Exploration Grant that

funded this project; to Mitacs for granting me the Mitacs Globalink Graduate Fellowship Award to pursue my graduate studies in Canada; to the Centre de Recherche en Biologie Structurale (CRBS) that grant me a CRBS Studentship Award funded by Fonds de Recherche de Québec (Health Sector) Research Centres Grant #288558; and to the Secretaría de Educación Pública de México (SEP) as a recipient of the Programa de Beca Complemento de apoyo al posgrado, Ciclo 2021.

Contribution of Authors

This study was designed and supervised by Dr. Adam Hendricks (Dept. of Bioengineering, McGill University). This thesis was written by Magda Giovanna Sánchez Sánchez and reviewed by Dr. Adam Hendricks.

Chapter 1 Some figures part of the literature review are not original work; credits and permissions can be found in the figure descriptions.

Chapter 2 rMfp-1 protein purification and microrheology experiments in condensates were performed by Dr. Hamideh R. Alanagh (Dept. of Chemistry, McGill University), co-supervised by Dr. Matthew J. Harrington (Dept. of Chemistry, McGill University). Plasmid to produce rMfp-1 was a gift from Dr. Dong Soo Hwang (Pohang University of Science and Technology). MATLAB codes to analyze the mechanical measurements were adapted for the experiment from codes developed by Dr. Adam Hendricks and previous lab members: Loïc Chaubet and Ora Cohen. All the data analysis and figures related to results were done by Magda Giovanna Sánchez Sánchez. Images and schematics for the byssus overview are not original work; credits and permissions can be found in the figure descriptions.

Chapter 3 Previously experimental protocol for cell mechanics established by Loïc Chaubet and Dr. Adam Hendricks was modified for the study of cell acetylation. MATLAB codes to analyze the cell mechanical measurements were modified from codes developed by Dr. Adam Hendricks and previous lab members: Loïc Chaubet and Ora Cohen. Plasmid used was a gift from Kristen Verhey (University of Michigan). All experiments, data analysis, and figures obtained for results were done by Magda Giovanna Sánchez

Sánchez. Images for the cell overview are not original work; credits and permissions can be found in the figure descriptions.

Chapter 4 Written by Magda Giovanna Sánchez Sánchez and reviewed by Dr. Adam Hendricks.

Chapter 5 Written by Magda Giovanna Sánchez Sánchez and reviewed by Dr. Adam Hendricks.

List of Figures

List of Tables

List of Abbreviations

AFM	Atomic force microscopy
AOD	Acousto-optic deflector
DLS	Dynamic light scattering
DOPA	3,4-dihydroxyphenylalanine
DWS	Diffusing wave spectroscopy
GESR	Generalized Einstein-Stokes relation
G'	Storage modulus
G"	Loss modulus
HA	Hyperacetylation
HDAC6	histone deacetylase 6
LLPS	Liquid-liquid phase separation
LOV	Light-Oxygen-Voltage
LVE	Linear viscoelastic
Mfp	Mussel foot protein
MSD	Mean square displacement
MT	Microubule
NaCl	Sodium chloride
Na_2SO_4	Sodium sulfate
OT	Optical tweezers
PEG	Polyethyleneglycol

preCols	Prepolymerized collagens
PTM	Post-translational modification
VPT	Video particle tracking
QPD	Quadrant photodiode
rMfp-1	Recombinant mussel foot protein-1
SFA	Surface force apparatus
SIRT2	Sirtuin 2
TMP	Thread matrix proteins

Introduction

The field of Rheology studies how materials flow and deform over time under the application of a force, providing models about their mechanical response that can be related to their internal structure. It has been of special importance in the study of soft materials which includes colloidal suspensions, polymer networks, liquid crystals, and biological materials [1]. In particular, rheological characterization of biomaterials such as cells or tissues is necessary to understand their complex structure and dynamics. Moreover, by understanding better their mechanical response to different physical and chemical stimuli, insights about their biological functions can be uncovered. Ultimately, this information can be used in the development of new treatments for diseases, or in the design of bio-inspired materials.

However, because biological samples can be very small or difficult to obtain in large quantities, rheological techniques at the microscale are necessary. Microrheology refers to the set of techniques that probe a material response to deformation on micrometer length scales under the application of microscale forces. These techniques usually involve the use of embedded micron- and nano-sized probes to locally deform a sample, and can be classified in two classes: active, when an external force is applied to the probe particles to deform the material; and passive, when the forces on the probe are only due to thermal fluctuations. In contrast to bulk rheology measurements, microrheology probes small samples and volumes at molecular and cellular scales, uses shorter acquisition times, and obtains information over a wider frequency range, making it a fundamental technique to study mechanical properties of biological materials. Currently, a wide range of microrheology techniques are available for rheological characterization of biological samples; the technique of choice will depend on the nature of the sample and the research question to be addressed.

For instance, a well established technique for the study of cellular mechanics is optical tweezers-based microrheology, which uses a focused laser beam to manipulate entire cells or probes inside them. Cell's mechanical behavior is highly determined by the cytoskeleton, a network formed by three types of dynamic filaments: microtubules, actin, and intermediate filaments [2]. Optical tweezers microrheology permits us to measure the deformation of the cell cytoplasm as a function of frequency, obtaining its viscoelastic modulus, which provides information about the remodeling timescales of the polymeric network. Then, by varying the conditions at which the cell is measured, the response of the cytoskeletal network to particular stimuli can be obtained.

Moreover, the cell cytoplasm is filled with several proteins and organelles that coexist with the cytoskeleton. Among those elements, are the membraneless organelles like the stress granules and P-bodies. In the last decade, it has been shown that membraneless organelles are the result of a process called liquid-liquid phase separation (LLPS), where they can coexist with the cytoplasm as liquid-like protein droplets named biomolecular condensates [3]. They have emerged as an important mechanism in the organization and regulation of biochemical activity inside cells, being fundamental in various biological processes such as gene expression. The protein chains inside the condensates interact via weak electrostatic interactions, forming a biopolymeric network able to rearrange [4]. Due to their compatibility with spatial and temporal resolution of optical tweezers-based microrheology, in the past decade this method has become a popular technique for their rheological characterization [5, 6, 7]. In analogy with measurements of the cytoskeletal network, a probe inside a protein condensate can be used to obtain its viscoelastic moduli, which serves to find the network relevant timescales.

Optical tweezers-based microrheology in biomolecular condensates has been broadly used to study condensates of intracellular nature. However, LLPS occurs extracellularly as well. For instance, some organisms produce extracellularly fluid precursor phases to fabricate high-performance polymeric materials such as the spider silk, or the mussel byssus. Nevertheless,

the use of optical traps to perform a rheological characterization of these type of extracellular condensed phases is largely unexplored.

To explore the application of optical tweezers microrheology in the rheological characterization of extracellular protein condensates, we introduce for the first time (to our knowledge) their use to investigate a mussel byssus condensate system. By adapting a previously developed optical tweezers-based microrheology technique, originally used in cell mechanics [8], we investigated biomolecular condensates of a recombinant mussel foot protein *in vitro*. Additionally, we used video particle tracking, a passive microrheology method that offers complementary information at low frequencies for samples in thermal equilibrium. Then, to illustrate the use of the optical tweezers microrheology technique in cells, we investigated how post-translational modifications of the microtubule cytoskeleton affect the mechanical properties of the cytoplasm in mammalian (U2OS) cells *in vivo*.

Despite coming from different organisms, both materials are composed of biopolymeric networks. In the case of the cell cytoplasm, the network is formed by semiflexible filaments that tend to be straight [9], in contrast to the mussel foot polymer molecules that are intrinsically disordered [10]. However, both are transiently crossliked, which means their network crosslinks attach and detach at particular rates providing them with the ability of rearrange, showing rich viscoelastic behaviors that can be characterized by measuring their deformation as a function of frequency. The same microrheology technique allows to obtain the viscoelastic response across relevant frequencies for both systems, which will be exploited to address a research question relevant to the system under study.

First, marine mussels produce high performance polymeric fibers from fluid protein condensed phases to tightly anchor to underwater surfaces. To better understand the chemical stimuli driving those transitions, our objective is to investigate the role of pH with sulfate and chloride ions, in the condensation, and potencially the assembly of polymers, of a recombinant mussel foot protein 1 (rMfp-1). By measuring their viscoelastic moduli we sought to uncover their effect in condensates dynamics at different conditions.

Second, as the cell's cytoskeleton determines in large quantity its mechanical behavior, we investigate in particular one of their filaments, the microtubules. To understand better their role in the mechanical regulation of the cell we target a post-translational modification, acetylation, known to modify their rigidity. Our objective is to investigate if microtubule acetylation has an effect in the dynamics of the intracellular network.

The thesis is organized in five chapters. The first chapter is dedicated to the basic physical concepts, theories, and description of the methods necessary to understand the rheological characterization of a material at microscale. The second chapter corresponds to the characterization of the mussel foot protein sample, offering a description about their nature and biological importance, theories about their fibers formation and the methodology and results from our characterization. The third chapter pertains to the cell, containing a more detailed description of the known effects of microtubule acetylation and our findings along with a description of the methodology followed. Chapter four covers the discussion of the implications of the findings in the context of each sample, as well as the future work to be done in each case. Finally, chapter five offers a summary of the results and closing remarks.

Chapter 1

The study of deformation

In this chapter the fundamental physical concepts and quantities used to perform a rheological characterization of a material in general will be described. Followed by the basic mechanical models used to establish a relation between force and deformation, which will be required to obtain important parameters during our posterior mechanical analysis. Then, given that our samples can be described as biopolymeric networks, a theory based in polymer networks will be introduced, to serve as a baseline to understand the relation between the molecular rearrangement of a material with their mechanical response to deformation. Finally, as we will use microrheology to study our samples, a review of the most popular microrheology techniques will be presented, along with their technical considerations, advantages and disadvantages, which will be necessary to understand how and why we selected the techniques presented in the study of our particular samples.

1.1 Essential principles

If we attempt to classify as solid or liquid the materials that surround our everyday life, we will soon realize that several of them behave as a mixture of both. A simple example is toothpaste, while it flows as a liquid-like material when squeezed out from the tube, it remains in a solid-like manner when placed on the toothbrush. The concepts, terminology and methods needed to describe many real materials that show a superposition of liquid-like and solid-like behavior constitute the field of Rheology.

The term itself derives from the ancient Greek words *rheo* (flow), and *logia* (study of).

However, rheological studies go beyond flow study only; they focus on the properties of matter that determine the reaction of a material to applied forces at different time scales; they analyze materials whose main characteristics are non-linear dependencies between forces and deformations or rates of deformation; and materials with structure changes under the application of a force [1]. As a result, rheological analysis had been essential to understand and develop an extensive number of different materials such as alloys, cosmetics, glass, polymers, food, plastics, etc., providing not only models to predict materials behavior but also ways to find information about their internal molecular structure and interaction [1].

To introduce the main concepts of a rheological analysis let us explore a classical study of deformation: the pure shear. Consider a material squeezed between two parallel surfaces placed at a fixed distance (h) from each other (Figure 1.1a). When one of the surfaces moves relative to the other, a tangent force (F) will be applied on the material. The ratio between F and the area of contact (A) represents the force applied per unit of surface area and is called the *shear stress* (σ) with units of pressure, Pascal (Pa). Additionally, the ratio of the relative displacement between the two surfaces in the direction of movement (x), with their distance of separation h, is defined as the *shear strain* (γ) and represents the deformation, which is the change in distance between two points inside the material and it is dimensionless. Finally, the rate of the deformation, or *strain rate*, can be defined as the derivative of the shear strain, $d\gamma/dt = \dot{\gamma}$. For forces applied perpendicularly to the surface the stress is called normal or tensile. As a force in any other orientation can be decomposed on tangent and normal forces it follows that in general, the concept of stress and strain can be applied to forces in any direction under the coordinate system of choice.

Next, we shall explore the relation between the stress applied on a material, and the resulting strain. Two ideal models are fundamental in rheology: the elastic solid and the viscous fluid. The first was published by Hooke in 1678[12] and states that strain of a so-called elastic material will be proportional to the stress applied and independent on the strain rate. This means that a solid material will deform instantaneously in a linear manner

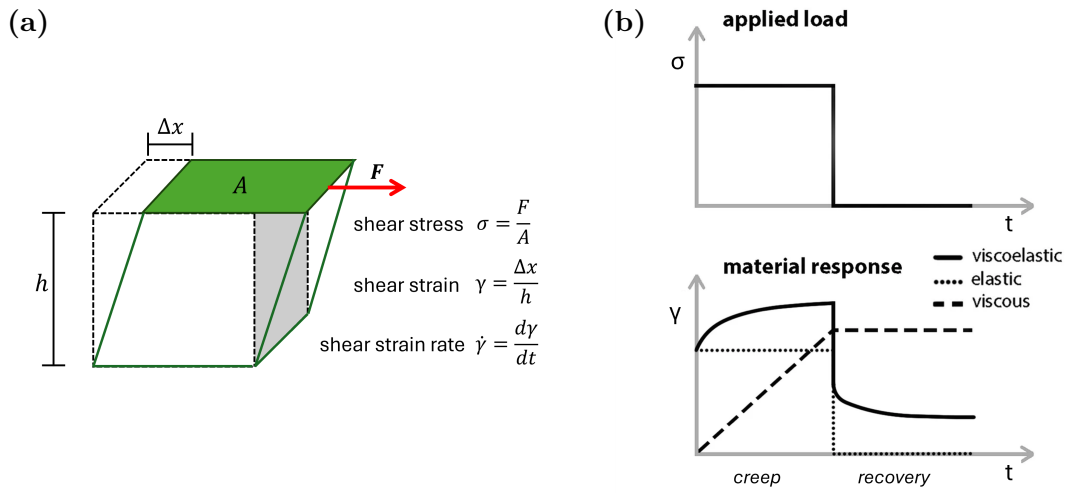

Figure 1.1: (a) Shear flow deformation. (b) Creep-recovery test (Figure (b) Reproduced from [11] with permission from Springer Nature, Copyright ©2021; permission conveyed through Copyright Clearance Center, Inc.).

when a stress is applied on it, and will return to its original shape once the stress is removed. In mathematical terms:

$$\sigma = E\,\frac{\Delta x}{h} = E\gamma \tag{1.1}$$

Where E is a constant proportional to the elastic modulus with units of Pa.

On the other hand, the viscous fluid model, introduced by Newton in 1687 [12] and complemented later by Stokes, establishes the flow of a viscous liquid to be proportional to the shear strain rate. In this case the material's deformation remains constant after removing the stress which is described by equation 1.2. The proportionality constant η is the viscosity of the material with units of Pa·s.

$$\sigma = \eta\frac{d\gamma}{dt} \tag{1.2}$$

Then, according to these descriptions, if we apply a constant load to a elastic solid or to a viscous liquid, and then remove it, the corresponding behaviors over time will be the ones shown in figure 1.1b. This experiment is known as a creep-recovery test. The continuous plot in the same figure, describes the materials that behave as a combination of

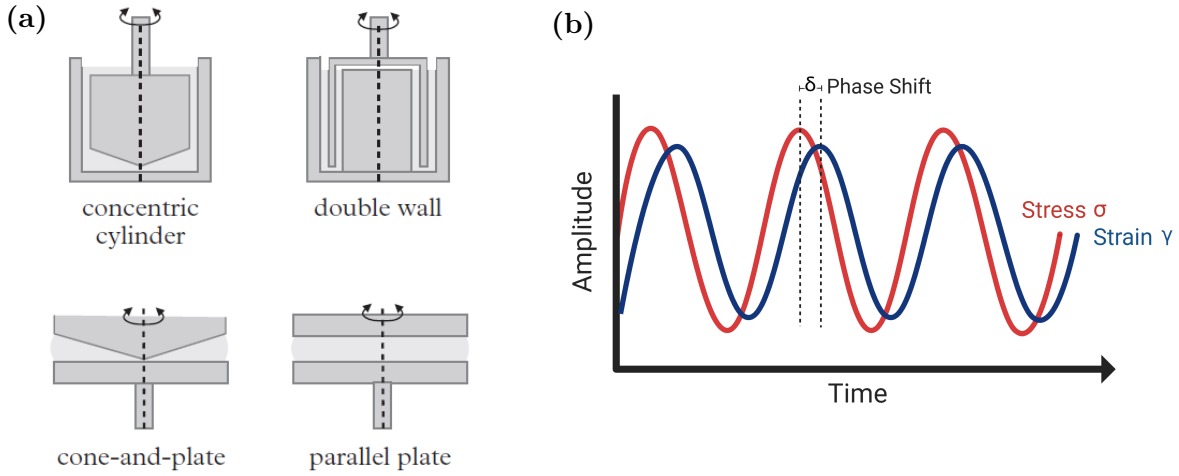

Figure 1.2: Oscillatory rheometry: (a) Common geometries for rotational rheometry. (b) Sinusoidally varying stress and strain; the phase difference and amplitude contain the rheological information of the material. (Figure (a) Reproduced from [14] with permission of Oxford University Press through PLSclear, Copyright ©2017; and figure (b) created with BioRender.com)

the aforementioned two models, which are known as viscoelastic. Comparing the material responses of figure 1.1b, it is visible that when the force is removed, the deformation is not maintained as in the liquid case, but it does not come back to its original shape either, as in the case of a solid. Instead, it relaxes until an intermediate strain value. The deformation of a viscoelastic material will depend strongly on the way the deformation is performed, the timescales of the experiment, and the magnitude of the forces applied [1].

In general, viscoelastic materials behave as solid-like or liquid-like depending on the deformation timescales. To account for the dynamical behavior of a material, a periodic oscillatory stress can be applied to measure its deformation as a function of time. The same information can be obtained by applying an oscillatory strain and measure the corresponding stress. These measurements are performed within the linear range of the system in which the deformations are small enough to have a linear relation between stress and strain that does not depend on amplitudes, which is called the linear viscoelastic (LVE) regime [13].

Commonly, mechanical rheometers are used to perform oscillatory deformations with a rotary system. By controlling the torque, they produce a shear stress on a sample placed

between two surfaces, which can have different geometries, such as concentric cylinders, parallel plates, a plate and a cone, etc. (Fig. 1.2a). The particular geometry determines the flow kinematics description, which is used to obtain the material's rheological properties[14]. Each rheometer has advantages and disadvantages to consider. For example, the cone-plate geometry offers a constant shear rate in the entire conical gap but it has a fixed gap that limits the particle size of the sample, whereas in the parallel plate configuration, the shear rate increases from the center to the edges of the plate, but the gap can be modified as the experiment requires it, allowing to test larger and stiffer samples. A shared disadvantage of these mentioned geometries is that low viscous samples can flow off of the gap, which can be prevented by using a concentric cylinder or double wall system, however, a larger amount of sample is required [15].

To understand better the oscillatory test, consider an oscillatory strain described by the equation 1.3. Then, the amplitude of the strain is γ_0 with an angular frequency ω.

$$\gamma(t) = \gamma_0 e^{i\omega t} \tag{1.3}$$

Where Euler's formula $e^{i\omega t} = \cos(\omega t) + i\sin(\omega t)$ was used.

In a linear regime, an oscillatory input will result in an oscillatory response at the same frequency. Then, the corresponding stress can be written as,

$$\sigma(t) = \sigma_0 e^{i(\omega t+\delta)} \tag{1.4}$$

with σ_0 the amplitude of the stress and δ its phase lag. These two quantities contain the rheological information from the material. Under this conditions, a phase lag of $\delta = 0$ will describe a purely elastic material, where the proportional relation of stress and strain from equation 1.1 is recovered. If $\delta = \frac{\pi}{2}$ this results in a function proportional to the derivative of the original oscillation as *sin* and *cos* derivatives are out of phase by $\frac{\pi}{2}$. This means that the

proportional relation of stress and strain rate from equation 1.1 is recovered and this phase corresponds to a purely viscous material.

Taking measurements over a wide range of frequencies allows to compute the *complex shear modulus* $G^*(\omega)$, a frequency dependent equivalent of the shear strain that can be defined as the ratio of $\sigma(t)$ and $\gamma(t)$ [14]:

$$G^*(\omega) = \frac{\sigma(t)}{\gamma(t)} = \frac{\sigma_0 e^{i\delta}}{\gamma_0} \tag{1.5}$$

The, also called, *complex modulus* or $G^*(\omega)$ is a complex number that can be written as:

$$G^*(\omega) = G'(\omega) + iG(\omega)'' \tag{1.6}$$

The real part G' is known as the *storage* or *elastic modulus* and describes the energy stored and returned by the material during the oscillation, thus measuring its elastic nature. On the other hand, the imaginary part G'' is known as the *loss* or *viscous modulus* because it measures the energy dissipation during the periodic oscillation [1]. Since $G^*(\omega)$ provides the viscous and elastic modulus, it is often refer as the *viscoelastic moduli*.

The phase shift δ for a frequency ω can be obtained by

$$\tan\delta(\omega) = \frac{G''(\omega)}{G'(\omega)} \tag{1.7}$$

The term $\tan\delta$, also known as the *loss tangent* is commonly used as a parameter to determine of how elastic ($\tan\delta < 1$) or viscous ($\tan\delta > 1$) a material is.

Additionally, from dividing $\sigma(t)$ by the $\dot{\gamma}(t)$ instead $G^*(\omega)$ we can obtain another parameter to describe the rheological material properties, the complex viscosity $\eta^*(\omega)$ [14], given by:

$$\eta^*(\omega) = \frac{\sigma_0 e^{i(\omega t+\delta)}}{i\omega\gamma_0 e^{i\omega t}} = \frac{G^*(\omega)}{i\omega} = \eta'(\omega) + i\eta''(\omega) \tag{1.8}$$

which contains the same information as the complex modulus, and particularly, relates the loss modulus with the real part of the complex viscosity,

$$G''(\omega) = \omega\eta'(\omega) \tag{1.9}$$

Finally, an alternative representation of a material's viscoelastic properties arise from the case where a stress of one unit of magnitude is suddenly applied on a material. The resulting strain is called the *creep compliance* of the material $J(t)$, whose Fourier transform $\widetilde{J}(\omega)$, is related to the complex modulus by the relation [14]:

$$G^*(\omega) \cdot \widetilde{J}(\omega) = \frac{1}{i\omega} \tag{1.10}$$

Therefore, the three time independent functions $G^*(\omega)$, $\widetilde{J}(\omega)$, and $\eta^*(\omega)$ will provide the rheological dynamic information of the material, which will help us understanding its structure and behavior to take a better advantage of their properties and functionality.

1.1.1 Basic viscoelastic models

To illustrate the viscoelastic behavior of materials, it is common to use the mechanical analogues of liquid and solid: the spring and dashpot (Fig.1.3). A dashpot is a piston moving inside a cylinder containing liquid. Then, the speed of the piston $v = dx/dt$ is proportional to the applied force, F [1]:

$$F = \eta v = \eta \frac{dx}{dt} \tag{1.11}$$

which is clearly analogous to the Newtonian law of liquids 1.2, assuming strain rate equivalent to velocity, stress correspondent to force, and the η coefficient analogue to viscosity. On the other hand, a spring is described by Hook's law, which states that the force required to

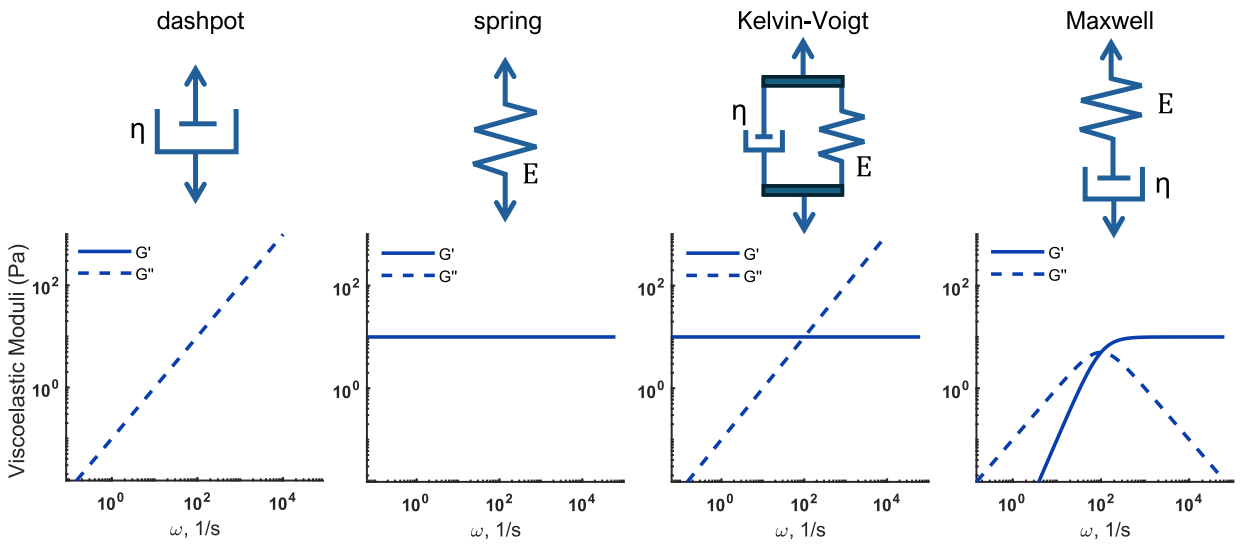

Figure 1.3: Basic mechanical elements to model viscoelastic materials and their corresponding storage and loss modulus with parameters $\eta = 0.1$ Pa·s and $E = 10$ Pa. The crossover frequency for the Kelvin-Voigt and Maxwell model corresponds to $\omega_c = E/\eta = 100s^{-1}$ in angular frequency.

compress, or extend, a spring a distance Δx is proportional to that distance:

$$F = -k\Delta x \tag{1.12}$$

where k represents the spring constant. This equation is analogous to the elastic behavior of a solid given by equation 1.1 considering k equivalent to the elastic modulus E, stress analogue to force and the distance equivalent to the displacement of the material under deformation [1].

Thus, to model the behavior of a viscoelastic material in the linear regime, a combination of springs and dashpots can be used to provide a mechanical model that shows an analogous behavior [13]. In particular, there are two basic combinations that can be joined to describe models of higher complexity: the Kelvin-Voigt model, formed by a spring and dashpot connected in parallel; and the Maxwell model, composed by a spring and dashpot connected in series (Fig.1.3).

Viscous fluid and elastic solid

In the frequency domain, the complex modulus of a viscous fluid with viscosity η consists of the loss modulus only, i.e, it is purely imaginary. Moreover, considering its relation to the complex viscosity (Eq. 1.9), the complex modulus of the viscous fluid will be:

$$G^*(\omega) = iG''(\omega) = i\omega\eta \tag{1.13}$$

Therefore, the shear complex modulus of a viscous liquid is proportional to the frequency with proportionality constant η. On the contrary, the complex modulus of a elastic solid will be purely real and equal to its elastic modulus E:

$$G^*(\omega) = G'(\omega) = E \tag{1.14}$$

Kelvin-Voigt model

The Kelvin-Voigt model assumes its elements remain parallel when a stress is applied. Hence, the strain of both, the spring and the dashpot, will be the same and the total stress will be the sum of the stresses in each element [12]. If a force is applied to a Kelvin-Voigt model, the dashpot will delay the response of the spring, thus the system behaves at first like a viscous liquid, and then at longer times when the spring gets more stretched, like a elastic solid. In consequence, it represents a viscoelastic solid. Writing the total stress in terms of Eqs. 1.2 and 1.1, we obtain:

$$\sigma(t) = E\gamma(t) + \eta\dot{\gamma}(t) \tag{1.15}$$

The Fourier transform of Eq. 1.15 is:

$$\sigma(\omega) = E\gamma(\omega) + i\omega\eta\gamma(\omega) \tag{1.16}$$

Therefore,

$$G^*(\omega) = \frac{\sigma(\omega)}{\gamma(\omega)} = E + i\omega\eta \tag{1.17}$$

which corresponds to a material with constant elastic modulus ($G'(\omega) = E$), and a loss modulus linearly related to the frequency ($G''(\omega) = i\omega\eta$)[13]. The crossover frequency, from where $G''(\omega)$ becomes larger than $G'(\omega)$, occurs at $\omega_c = E/\eta$.

Maxwell model

When a force is applied to a Maxwell material where the spring and dashpot are in series, it will stretch the spring immediately, thus behaving like an elastic solid. Right after, the spring will gradually pull out the piston, which responds slowly in comparison to the spring, and will result in a viscous-like behavior at long timescales. In this case, the applied stress will remain the same but the two elements will have a different strain. Mathematically, the stress of the system will be described by [13]:

$$\sigma(t) = \sigma_0 e^{-\frac{t}{\tau_c}} \tag{1.18}$$

where the term $\tau_c = \eta/E$ is the relaxation time of the Maxwell model, with η and E the elements constants. Correspondingly, the complex shear modulus is [14]:

$$G^*(\omega) = \frac{i\omega\eta}{1 + i\omega\tau_c} \tag{1.19}$$

The Maxwell relaxation time is related to the crossover frequency as $\omega_c = 1/\tau_c$. In general, Eq. 1.19 can be interpreted as follows: the deformation of the material at times $t < \tau_c$, or frequencies $\omega > \omega_c$, will be mainly elastic. On the contrary, for times $t > \tau_c$ and frequencies $\omega < \omega_c$, the deformation will be predominantly viscous and behave like a liquid. Interestingly, in the limit $\tau_c \to 0$, the Maxwell fluid reduces to a Newtonian fluid (Eq.1.13) with viscosity η.

The storage and loss modulus can then be obtained from 1.19 as [14]:

$$G'(\omega) = \frac{\omega^2 \tau_c \eta}{1 + \omega^2 \tau_c^2} \tag{1.20}$$

$$G''(\omega) = \frac{\omega \eta}{1 + \omega^2 \tau_c^2} \tag{1.21}$$

Jeffrey's model

As mentioned already, more complex behaviors can be modelled by the addition of multiple Maxwell and/or Kelvin-Voigt elements. A relevant model for this project is the Jeffrey's viscoelastic fluid. This model can be obtained either from the addition of a Kelvin-Voigt element and a dashpot in series, or equivalently by the addition of a Maxwell element and a dashpot in parallel [12]. Hence, it can be written as a linear combination of a Newtonian fluid of viscosity η_0 and a Maxwell fluid [16] with parameters E, η_1 and τ_1, resulting in the complex modulus:

$$G^*(\omega) = i\omega\eta_0 + \frac{i\omega\eta_1}{1 + i\omega\tau_1} \tag{1.22}$$

This model represents a viscoelastic fluid with two transitions, starting with a liquid-like behavior at low frequencies, reaching a elastic-solid like behavior at intermediate frequencies, and transitioning to a viscous behavior again at the highest frequencies.

1.1.2 Viscoelasticity and reversible crosslinks

Living organisms synthesize carbon-containing macromolecules as the building blocks to construct cells and the necessary components to perform their living functions. These macromolecules are polymers formed by small organic molecules linked together via covalent bonds, thus producing long chains, like proteins or nucleic acids. Their covalent bonds allow rotation of the joined atoms, providing the chain with a great flexibility, which

allows it to adopt different shapes and conformations under the effect of thermal forces. Nevertheless, different parts of the same molecule can form noncovalent bonds, such as electrostatic interactions, hydrogen bonds or van der Waals forces, thus constraining the polymer shape and producing attraction to other molecules [17]. Moreover, in many situations the energy of the non covalent bonds formed is comparable to the energy from thermal fluctuations so they can be reversed, for example by a change in temperature or concentration [18]. Thus, these bonds are known as reversible crosslinks.

In general, crosslinks have a finite lifetime; hence, they continuously associate and dissociate. In consequence, when polymers form networks via reversible crosslinks, known as *transient networks*, the resulting materials show rich viscoelastic properties [19]. A first theory to relate viscoeasticity and molecular structure of transient networks relate the viscoleastic behavior with the lifetime (τ_b) of the reversible crosslinks, so that the system shows elastic behavior at faster deformations than τ_b, and a fluid behavior at slower deformations that τ_b [20]. In other words, if we apply a stress to a material at times longer that the bond dissociation rate, the chains would diffuse inside the material, i.e, they will flow [21].

A posterior model proposed by Tanaka and Edwards [18, 22], considers two kinds of chains in the network: elastically active, a chain connected by its two ends to the junctions (through sticky functional groups), that can transmit stresses; and dangling chains, with only one end attach to a junction, thus being free of external forces. In this model, the viscoelasticity depends on the combination of two molecular parameters: the chain breakage rate $\beta(r)$, which is the probability of a crosslink to break and form a dangling chain under a stress; and p, the chain recombination rate, which is the probability of a dangling chain to capture a junction and form a elastic chain. In the particular case were $\beta(r) = \beta_0$ is constant, the model reduces to a Maxwell model (Eq.1.19) with a single relaxation time of $\tau_c = 1/\beta_0$ [22].

These models show the important contribution of crosslinking dynamics in the viscoelastic

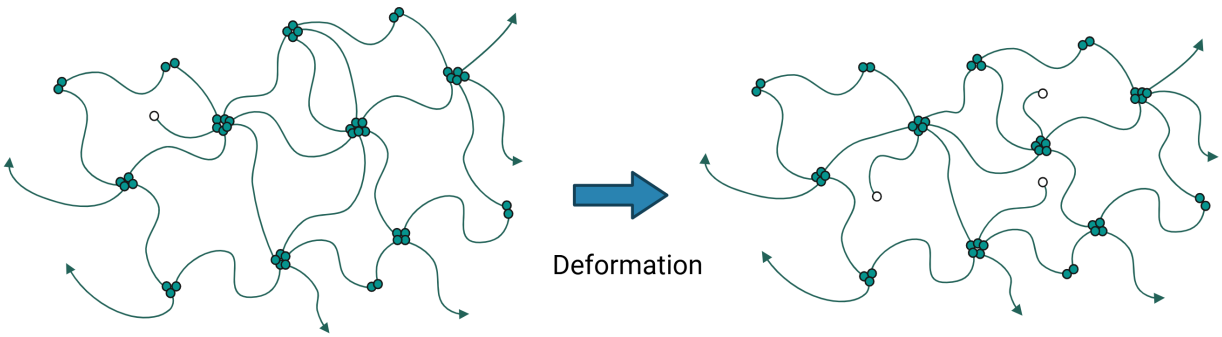

Figure 1.4: Transient network model. Polymer chains with "sticky" functional groups at both chain ends form a network through reversible crosslinks. When both chain ends are attached to other chain they can transmit a stress upon deformation, so they are called elastic chains. When one end of the chain is loose, it is called a dangling chain (the attached state between functional groups is represented by filled circles whereas the open circles represent the unassociated functional groups). Deformation increases the probability β of a elastic chain to separate from the junction, whereas a dangling chain can be captured by a junction and form a elastic chain at a rate p. Hence, the viscoelastic properties of the material will depend on the breakage rate β (unbinding) and the recombination rate p (binding), which determine the proportion of elastic and dangling chains present in the network (Figure created with BioRender.com).

behavior of a material. However, they consider only one type of junction present whereas in reality, the available interactions in a molecule can be very large; they also assume a regime were there are no other molecules entangled in the network, which is not always the case. Nevertheless, they have served as a baseline to model several biological systems as they are composed of networks of biopolymers. For instance, the protein networks that give support to the cell behave like a transient network of semiflexible polymers, thus several models describing their viscoelastic behavior rely in crosslinks unbinding and binding rates as the main system parameters [9].

Another example can be found in the dynamics of some biopolymeric solution mixtures. Considering two polymer solutions brought together, if the attractive groups in the polymer chains of one solution can form noncovalent bonds with groups present in the polymer molecule of the other solution, named associative polymers. The interaction can lead to the formation of a two-component dense mixture, thus undergoing a phase transition to a

dense phase that will coexist with a dilute phase with low polymer concentration [4]. Further, as the new fluid phase was formed by reversible crosslinks, it will exhibit a rich viscoelastic behavior, like a transient network, given its bonds finite lifetime. This scenario is particularly relevant in the context of condensed protein phases that exist in the cell cytoplasm, where an important molecule known to drive phase transitions with other macromolecules is the RNA [4].

Overall, viscoelastic measurements of a polymeric material, including those of biological nature, can provide information about the rates at which its internal components rearrange, as well as offer insights relating the interactions of the macromolecules that comprise it, the density and nature of the crosslinks present and the response of the material to external stimuli.

1.2 Microrheology

Biological samples are built from different biopolymers, in consequence there are several biological specimens showing a viscoelastic behavior, such as blood, cells, or even some cell organelles [23]. Hence, understanding their dynamic rheological properties, and what affects them, could provide essential information about their function, the stimuli they respond to, the chemical cues involved, etc. In addition, understanding the rheological complexity of biological materials could open new paths for prevention and treatment of different diseases that affect peoples' quality of life by uncovering the determinant conditions that lead to a healthy or unhealthy state.

Nevertheless, being familiar with the basic concepts related to basic rheological analysis in the linear regime, the limitations of using a mechanical rheometer become evident. For instance, even the most modern rheometers require a minimum sample size in the range of tens of microliters to milliliters [23]. This is a disadvantage if we want to study micron-sized samples like cells, or proteins that are very difficult to obtain in large amounts. Moreover,

in order to acquire relevant information, rheological measurements should be performed at relevant physiological scales in time ($\sim \mu$s), and space ($\sim$nm). Thus, alternative rheological tests are required to explore and understand micron-sized biological samples.

Microrheology is the branch of rheology encompassing techniques that allow scientists to study rheological properties of materials at the microscale. Typically, microrheology techniques involve the use of *micro* or *nano* sized probes embedded in the material of interest, studying their movement in response to external and internal surrounding forces to deduce the material's rheological properties.

Historically, a major breakthrough for the development of microrheology techniques occurred in 1995, when Mason and Weitz showed that the response of a fluid to equilibrium thermal fluctuations, measured using small particle probes, has a well defined relation to the material's bulk response to deformation [24]. They obtained $G^*(\omega)$ from thermal fluctuations and found a good agreement with the $G^*(\omega)$ measured by mechanical methods, expanding with their work the possibilities to explore a wider range of materials at microscales. In addition, microrheology techniques development was facilitated by the technological advances in microscopy, high speed resolution cameras, laser optics, etc., which improved the ability of manipulation and detection of micron-sized probes at very short times.

The main advantages of microrheology techniques are: the use of small samples and volumes (1-10μL), short acquisition times (ms-μs), a broad range of frequency analysis (kHz-MHz), good sensitivity and, the ability to map also the local behavior of the material [14]. This advantages have placed microrheology as one of the principal techniques of choice to study the complex structure and dynamics of biological materials. There are two approaches: *passive*, when the deformation of the material is due only to the thermal fluctuations; and *active*, when the material responds to an applied external force.

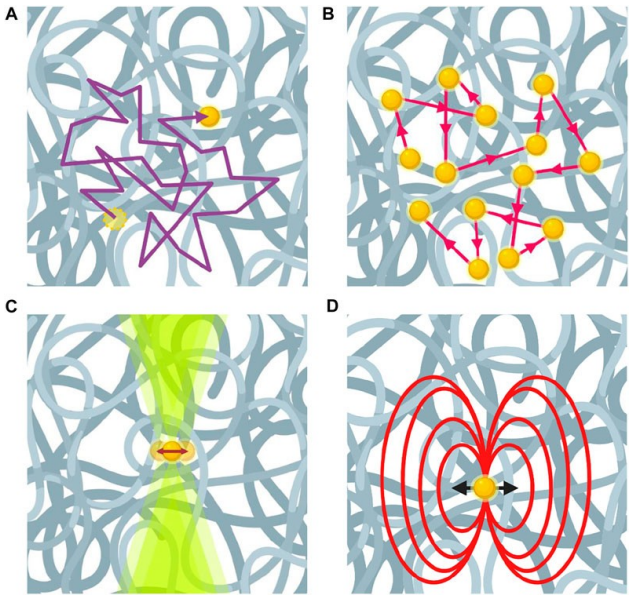

Figure 1.5: Microrheology using different techniques for passive and active measurements. (a) Representation of a single probe tracked over time as done during video particle tracking measurements. (b) Incident light in the sample is scattered multiple times by the embedded probes in a diffusive wave spectroscopy measurement, providing information about their motion. (c) A external force is applied on a probe using an optical trap. (d) A magnetic field drives the movement of a magnetic probe to test the material. (Figure reproduced from [23] licensed under the Creative Commons Attribution CC BY 4.0, Copyright ©2022.)

1.2.1 Passive microrheology

Passive microrheology relies on small particle probes embedded in the material and driven only by thermal fluctuations. This condition limits this method to the study of materials soft enough to detect the probes movement due to those fluctuations. Typically, to obtain the information of the material, the mean square displacement (MSD) is computed [13]. This quantity represents the statistical displacement of the particles over time by calculating the ensemble average displacement of a group of particles over different lag times τ according to the equation 1.23:

$$\langle \Delta r^2 (\tau) \rangle = \langle [\boldsymbol{r} (\tau + t) - \boldsymbol{r} (t)]^2 \rangle \tag{1.23}$$

Where $\boldsymbol{r}$ represents the vector with the position coordinates of the particle at a specific time. If we consider a pure viscous fluid, the particles will follow a simple diffusion process

hence presenting Brownian motion, which relates the MSD with the diffusion coefficient D as [14]:

$$\left\langle \Delta r^2 \left(\tau\right) \right\rangle = 2\mathbb{N}D\tau \tag{1.24}$$

Where $\mathbb{N}$ is the dimensionality of the problem, and D can be related to the Stokes dragging force of a sphere in a viscous fluid by the Stokes-Einstein equation:

$$D = \frac{k_B T}{6\pi\eta a} \tag{1.25}$$

With η the viscosity of the fluid, a the radius of the particle, k_B the Boltzmann constant, and T the absolute temperature (units of Kelvin, K).

In the case of more complex materials, the MSD behavior will reflect their elastic and viscous components. In these cases, the relation with τ is not necessarily linear anymore In particular, a power law relation is a common approximation for viscoelastic materials [25],

$$\left\langle \Delta r^2 \left(\tau\right) \right\rangle \sim \tau^{\alpha} \tag{1.26}$$

Where α is called the diffusion exponent. For a freely difussive particle $\alpha = 1$, for a subdifussive process $0 < \alpha < 1$ and $\alpha = 0$ represents a trapped particle.

In their work, Mason and Weitz generalized the relation between the MSD and the shear complex modulus in the Laplace space, the so called Generalized Einstein-Stokes Relation (GESR) [24]. Assuming a system at thermal equilibrium and negligible inertia, the relation is expressed as

$$\tilde{G}\left(s\right) = \frac{\mathbb{N}k_b T}{3\pi a s \langle \Delta\hat{r}^2\left(s\right)\rangle} \tag{1.27}$$

with $s = i\omega$ and $\langle \Delta\hat{r}^2\left(s\right)\rangle$ the Laplace transform of the MSD, and T the absolute temperature. In the Fourier space, the GESR can be written as follows:

$$G^*(\omega) = \frac{\mathbb{N}k_bT}{3\pi a i\omega\langle\Delta\tilde{r}^2(\omega)\rangle} \tag{1.28}$$

Where $\langle\Delta\tilde{r}^2(\omega)\rangle$ represents the unilateral Fourier transform of the MSD, and we recovered the shear complex modulus introduced in equation 1.6 [25].

To avoid the mathematical complexity that arises from the transforms in the denominators of expressions 1.27 and 1.28, the relation presented in equation 1.10 is commonly used. In this manner, the Fourier transform of the creep compliance will be given by:

$$\tilde{J}(\omega) = \frac{1}{i\omega G^*(\omega)} \tag{1.29}$$

and using equation 1.28 follows:

$$\tilde{J}(\omega) = \frac{3\pi a}{\mathbb{N}k_bT}\langle\Delta\tilde{r}^2(\omega)\rangle \tag{1.30}$$

This expression can be directly transformed to the time domain, where the measured MSD can be related to the creep compliance as:

$$J(\tau) = \frac{3\pi a}{\mathbb{N}k_bT}\langle\Delta r^2(\tau)\rangle \tag{1.31}$$

Although equation 1.31 facilitates the relation to the measured MSD, in practice, the MSD is still a discrete set of data that has to be numerically transformed to the Fourier or Laplace space, which leads to significant errors at frequency extremes [25]. Different published methods to recover G* from the MSD reducing the noise effects can be found. They involve the approximation to the Laplace transform [26], the numerical computation of the transform of creep compliance [27] or the normalized auto correlation function [28], plus additional fitting routines. Nevertheless all of them rely on the validity Generalized Stokes-Einstein Relation 1.28.

In addition, probe surface chemistry plays an important role in passive microrheology. If

the probe interaction with the surrounding material is strong enough to modify its structure, the measurements obtained will reflect its local microenvironment and not its bulk behavior. To avoid undesired interactions, the probe particles can be functionalized or coated with polymers that decrease protein absorption, for example polyethyleneglycol (PEG)[14].

An important reminder when using passive microrheology is that the validity of the GSER relation requires the system to be at thermal equilibrium and inertia should be negligible, which can be violated at higher frequencies. This also means that the response obtained by this method will be linear. When there are other forces that can drive the system out of equilibrium, complementary methods to obtain the rheological properties must be used.

Next we will present some of the most common techniques used to obtain the MSD from a set of probe particles in passive microrheology measurements.

1.2.1.1 Video particle tracking

Video particle tracking (Fig. 1.5a) is a well-known and accessible passive rheology technique. In this method a brightfield or epifluorescence microscope is set to visualize spherical particles inside the material under study. A high-speed camera is used to record the trajectories of the beads during a time relevant for the experiment conditions, where the temporal resolution will be determined by the frequency at which the positions are recorded. Use of fluorescent beads is preferred because it provides a high signal-to-noise ratio as well as high contrast when tracking the particles. The particles size should be chosen small enough to respond to the thermal fluctuations of the surrounding medium but big enough compared to the mesh size of the material to truly represent the properties of the bulk state [14]. Later, a computational analysis of the video is done with the aid of available tracking algorithms to obtain the trajectories of the particles inside the sample. Once the trajectories of many beads are obtained, the mean squared displacement (MSD) is computed using equation 1.23, to then process the data to obtain G* using the GSER formalism.

1.2.1.2 Light scattering techniques

There are two popular methods to perform passive rheology based on the light scattered from small particles inside the sample of interest. The first, dynamic light scattering (DLS), is a method where a laser beam hits a transparent sample with probe particles and the scattered light is collected by a sensor with an angle θ with respect to the incoming beam. This method assumes each photon is deflected once and measures the intensity of the scattered light over time $I(t)$, which fluctuates as the particles diffuse in the sample [25]. The normalized intensity correlation function $g_2(\tau)$ is computed as:

$$g_2(\tau) = \frac{\langle I(t)I(t+\tau)\rangle}{\langle I(t)\rangle^2} \tag{1.32}$$

where $\langle\ \rangle$ represents the time average. This function is related to the electric field correlation function g_1 by the Siegert relation [25]:

$$g_2(\tau) = 1 + \beta|g_1|^2 \tag{1.33}$$

Where β is determined by the coherence of the detection setup. If the particles move only in response to thermal fluctuation, then $g_1(\tau)$ will be related to the MSD in an exponential decay manner:

$$g_1(\tau) = \exp\left[\frac{-q^2\left\langle \Delta r^2\left(\tau\right)\right\rangle}{6}\right] \tag{1.34}$$

with the scattering wave vector $q = \frac{4\pi n}{\lambda} sin(\frac{\theta}{2})$, where n is the refractive index of the medium and λ the laser wavelength. Then, the three dimensional MSD is extracted numerically by means of equation 1.34. This method offers a high frequency resolution ($> 10^3$ Hz), however, it requires the sample to be transparent enough to allow at least 90% of the light to be transmitted to achieve the proper detection of the scattered light [23].

The second method is diffusing wave spectroscopy (DWS) (Fig. 1.5b), in which a laser

beam hits a highly-turbid sample in a similar manner that DLS, but assumes the light will be scattered multiple times before being measured, loosing the angle dependence and allowing a wider range of frequencies to be measured (up to 10^3-10^6 Hz) [14, 25]. Under this frame, photons can be thought of as taking random walks through the sample [14], which mathematically translates in the light propagation being modeled applying the diffusion equation for photons. Thus, the field correlation function $g_1(\tau)$ is related to the MSD as:

$$g_1(\tau) \propto \int_0^\infty P(s) \exp\left[\frac{k_0^2 s \left\langle \Delta r^2 \left(\tau\right)\right\rangle}{3l^*}\right] ds \tag{1.35}$$

where $P(s)$ describes the probability of the light to travel a path s, $k_0 = \frac{2\pi n}{\lambda}$ with n the refractive index of the solution, λ the laser wavelength and l^* the light transport mean free path [25]. The MSD can then be obtain numerically from equation 1.35.

Overall, DWS can be used in opaque solutions as it requires a higher scattering of the particles. It is also more sensitive to smaller length scales and faster timescales compared with DLS [25].

1.2.2 Active microrheology

As mentioned earlier, passive microrheology is limited to soft materials. To measure materials with a higher degree of elasticity, a different approach must be used. Active microrheology involves small probes that are actively manipulated to exert forces on the material. These forces are commonly applied by using optical or magnetic forces [13]. The type of measurements available using these techniques are analogous to the ones mentioned in section 1.1, like the creep test or the oscillatory stress application, where the response of the material will be measured through the forces that the probe feels from its surroundings. The active approach allows the application of larger stresses, useful for stiffer materials, and the study of non-equilibrium behavior of samples if forces large enough are applied to be outside the linear regime [14]. Next, some of the most used active techniques will be

reviewed.

1.2.2.1 Optical manipulation

In the nineteenth century Maxwell's electromagnetic theory showed that light propagation on a medium produces a pressure perpendicular to the direction of propagation, the so called, radiation pressure [29]. However, the pressure effect was measured to produce a force of 7nN for a light source with 1W of power [29], a very small force to have any applicability at that time. Nonetheless, the invention of the laser in 1960 opened the possibility to study in more depth the light matter interaction. Then in 1970, Arthur Ashkin calculated what size a particle should be to feel the effects of light pressure and, using micron-sized latex particles, he found out that when focusing a laser beam with a power of mW, the spheres placed around the beam edges were attracted to its center and at the same time pushed in the direction of light propagation [30]. Consequently in 1986, Ashkin and colleagues presented a three dimensional optical system using a strongly focused laser beam able to trap particles of sizes from 25nm to 10μm in its center [31]; the optical tweezers, were born. Known also as optical traps, soon it became clear its potential use in the study of biological systems given its spatial and temporal range of application along with its low invasive effects. In 2018 half the Nobel Prize in Physics was awarded to Ashkin "for the optical tweezers and their application to biological systems" [32].

Recently, optical tweezers have become a fundamental tool in the study of micro scale systems, specially biological ones. As a device to exert and measure small forces in a controlled manner it emerged as an important tool for microrheology techniques as well (Fig. 1.5c). In addition, modern optics allow a high control of a laser's position in a way that a probe particle can be trapped and moved in a constant, or oscillatory manner, along with the focused laser. This probe then can be use to stress the sample under study and measure its response to deformation.

When a laser beam interacts with a small particle, the light will exert two forces on

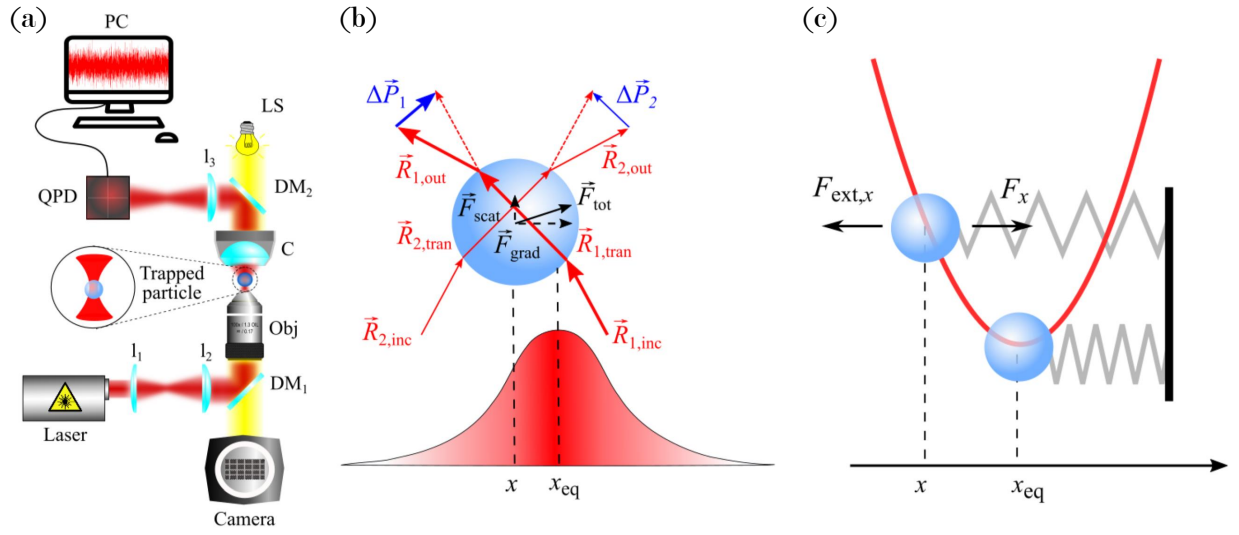

Figure 1.6: Optical tweezers setup and principles. (a) Optical tweezers setup. The dielectric mirrors DM_n constitute the steering beam system and can be substituted for other devices like spatial light modulators (SLM) or optoacoustic deflectors (AOD). (b) Scattering and gradient forces acting on a trapped bead away from the trap focus. Additionally, a description of the light momentum contribution of rays $\vec{R}$ of different intensity is depicted. The resulting momentum $\vec{P}$ attracts the bead to the trap center. (c) The force applied on the probe can be modeled as the recoil force of a spring as it moves away the equilibrium position.(Figure reproduced from [34] licensed under the Creative Commons Attribution CC BY 4.0, Copyright ©2023.)

it: the gradient force, which will attract the particle towards the more intense part of the laser beam; and the scattering force, which will push the particle in the direction of the light propagation (Fig. 1.6b) [25]. In an optical tweezers system, an objective lens with a high numerical aperture tightly focuses the laser producing a high intensity light spot at the center of the trap, allowing the gradient force to overcome the scattering force, and a particle to be attracted and stably trapped at it [33].

Typical optical tweezers systems are built using a conventional microscope with a high numerical aperture objective to focus the laser beam at the sample chamber. A beam steering system placed before reaching the objective, controls the trap position. Then a condenser lens receives the transmitted light which is directed to a position-sensitive detector, commonly a quadrant photodiode (QPD), to detect the light position changes. A camera is used to

visualize the sample and additional features like fluorescence microscopy can be added to they system. Near infrared laser wavelengths are commonly chosen to avoid biological samples damage [35]. Figure 1.6a shows a standard OT system example.

As any other device, a correct calibration of the system is fundamental for the accuracy of force measurements. An extensive number of calibration methods have been established since the OT introduction [33]. Next, some of the less complex calibration examples will be introduced.

When a trapped bead moves outside the trap center, the laser beam will deflect. This deflection in the transmitted light is detected at the objective's back focal plane by the position-sensitive detector. The voltages given by the detector can be related to the position of the bead relative to the trap's center by a sensitivity constant β_{pd}, given in units of distance per volt. The first trap calibration step is to obtain β_{pd}. The simplest method is to fix a bead on the coverslip and move it around the center of the focused laser at different distances with the aid of the microscope stage. This method will provide a relation between distance from the trap center, and voltage measured by the detector. At distances close to the trap focus, this relation is linear, so the slope of the plotted distance vs voltage will provide the sensitivity value β_{pd} [36].

Once the detection position sensitivity is calibrated, the optical trap can be used as a force transducer due to its behavior as a harmonic potential close to its center position, x_0. The trapping force can be modelled as a Hookean spring with a proportionality constant κ, called the *trap stiffness* (Fig. 1.6c). The corresponding restoring force along the x direction can be expressed as:

$$F = -\kappa(x - x_0) \tag{1.36}$$

Knowing the trap stiffness, the displacement of the bead from the trap center $(x - x_0)$ is used to calculate the trapping force. Perhaps the more straightforward method to obtain it, is using the equipartition principle. Considering a trapped bead, the energy associated to a

one dimensional harmonic potential is $U = \kappa\langle(x - x_0)^2\rangle/2$, with $\langle\ \rangle$ denoting the average. Then, the equipartition principle establishes that in thermodynamic equilibrium the energy of the system should be [33]:

$$\frac{k_B T}{2} = \frac{1}{2}\kappa\ \langle(x - x_0)^2\rangle \tag{1.37}$$

By sampling the fluctuations of the trapped bead positions over a period of time, κ can be found as:

$$\kappa = \frac{k_B T}{\sigma_x^2} \tag{1.38}$$

with $\sigma_x^2 = \langle(x - x_0)^2\rangle$ the variance of the bead displacement from x_0. This method is independent of the viscoelastic properties of the material and allows for a reliable computation of κ. Once the trap is calibrated, the beam steering system can be used to move the probe particle to inflict a deformation in the surrounded material.

In general, if we apply an oscillatory movement to a bead optically trapped within a viscoelastic material, in the linear regime the corresponding frequency dependent displacement response will be $u(t) = u(\omega)e^{-i\omega t}$. Ignoring inertial effects, the equation of motion of the trapped bead plus an oscillatory force can be modeled by the generalized Langevin equation[37],

$$\int_{-\infty}^{t} \zeta\,(t - \tau)\,\vec{u}\,(t)\,d\tau = -\kappa\vec{u}\,(t) + \kappa F_0 e^{-i\omega t} + \vec{F}_r\,(t) \tag{1.39}$$

Where the integral term introduces a time dependent memory function $\zeta\,(t)$, that represents the effect of the viscoelasticity of the material, F_0 is the amplitude of the oscillatory force, $\vec{u}(t)$ the velocity, κ the trap stiffness, and $F_r\,(t)$ the thermal force. $u(t)$ depends on the material's viscoelasticity but we know that is an oscillation as well, thus the first two terms of equation 1.39 can be interpreted as one apparent sinusoidal force $F_a(t)$. Now, taking the Fourier transform of Eq.1.39 averaged over time ($\langle F_r\,(t)\rangle = 0$), it

allows to write the frequency-dependent response of the probe $u(\omega)$ in terms of an apparent complex response function $\chi(\omega)$ [37]:

$$u\left(\omega\right) = \chi\left(\omega\right) F_a\left(\omega\right) \tag{1.40}$$

$\chi(\omega)$ includes the response of the probe owed to the trap effects and the material itself, and can be measured experimentally. The actual response function due only to the viscoelasticity of the material is given by [37],

$$\alpha\left(\omega\right) = \frac{\chi\left(\omega\right)}{1 - \kappa\chi\left(\omega\right)} \tag{1.41}$$

This response function can be then used to obtain the shear complex modulus as they are related by the equation:

$$\alpha\left(\omega\right) = \frac{1}{6\pi a G^*\left(\omega\right)} \tag{1.42}$$

From where we can obtain the real and imaginary part of $G^*(\omega)$ to know the elastic and viscous contributions of the material under study.

1.2.2.2 Magnetic manipulation

Magnetic manipulation (Fig. 1.5d) of small embedded probes is one of the oldest microrheology techniques, in particular, its application to study biological samples, can be tracked to the early twentieth century [14], and is still widely used. Magnetic fields can drive either translational or rotational movement of a probe particle. The probe's motion is measured over time and the viscoelastic properties of the material are calculated using the applied force and the bead motion information. Current magnetic systems, sometimes called *Magnetic tweezers*, usually include electromagnets that can be tuned to exert forces from femtonewtons to nanonewtons [14]. They also have a tracking system to measure the probes displacement, which is commonly video microscopy based.

The force the probe experiments will depend on their magnetic properties. The most common magnetic probes are paramagnetic (also called superparamagnetic), which means they do not have a magnetic moment but can be magnetized in the presence of a magnetic field and align with its direction. Ferromagnetic probes on the other hand, can have a magnetization without the need of an external magnetic field [14].

The experimental configurations will depend on the type of measurements to be achieved. In a simple design, two electromagnetic coils induce a magnetic field $B(t)$ in the focal plane of the imaging system. The paramagnetic probes embedded in the sample of interest will experiment a force proportional to the square of the current $I(t)$ in the coil [13] which will produce a translational motion of the probe.

$$\mathbf{F}(t) \propto I^2(t) \tag{1.43}$$

The proportionality constant can be found through the balance of a constant magnetic force and the viscous drag of a known viscosity newtonian fluid using the Stokes's equation:

$$\mathbf{F_d}(t) = 6\pi\eta a\mathbf{v}(t) \tag{1.44}$$

Measuring the velocity from the probe's displacement over time, a calibration curve can be obtained.

To perform a creep test,a force pulse $F_m(t)$ is applied and the particle deflection is tracked over time.The creep compliance can be determined as:

$$J(t) = \frac{6\pi a x(t)}{F_m(t)} \tag{1.45}$$

A measured of the relaxation behavior can be done as once the field is turned off.

In the case of an oscillatory force, similar as the analysis presented in section 1.1, a magnetic driven oscillatory force $F_m = F_0 e^{(i\omega t)}$ will produce a bead displacement given by

$x(t) = x_0 e^{i(\omega t - \delta)}$ where δ is the phase shift between the force and displacement. The loss and storage modulus of the material are then given by [13]:

$$G'(\omega) = \frac{F_0}{6\pi\eta a x_0(\omega)} \cos(\delta(\omega)) \tag{1.46}$$

$$G''(\omega) = \frac{F_0}{6\pi\eta a x_0(\omega)} \sin(\delta(\omega)) \tag{1.47}$$

A more complex method known as *twisting magnetometry*, applies a short strong magnetic field to magnetic particles. While the field is on, the magnetic moment of the particles aligns with the field. When it is turned off, the alignment of the particles themselves produces a remnant field whose decay can be measured as the moments become randomized again. If rotational diffusion is important for the randomization, the decay can be related to the viscosity of the sample. Another approach of this method involves adding a weaker external field, oriented perpendicular to the first stronger field. Under this scenario, this field will exert a maximal torque to the remnant field of the particles after the first field is turned off. The particles will then rotate towards the second field's direction and the rate at which the particles align to the perpendicular field, along with the recoil once the field is removed, can be used to give a measure of the viscoelasticity of the material [25].

A variant of this technique widely used in cell's surface force measurements is *magnetic twisting cytometry*. Briefly, ferromagnetic particles are ligand coated to be attached to the cell's surface. The magnetic particles are first oriented in one direction with a magnetic field. Then they are twisted in a perpendicular direction producing a controlled shear stress on the cell's surface. Once the field is turned off, the remnant field is measured with a magnetometer and it is related to the cell's mechanical response to the rotational motion, the angular strain. The viscoelastic frequency dependent response could be obtained if the twisting varies sinusoidally with time, however, to compute the complex moduli the surface contact area between cell and particle should be known [25].

1.2.2.3 Alternative active techniques

Although several microrheology approaches use small probes inside a sample to measure its rheological properties, there are alternative contact techniques that can probe deformation and forces at microscale without an embedded probe being required. As they can provide rheological properties of micron-sized materials they can be considered microrheology techniques as well. Here we briefly mention two of them.

Atomic Force Microscopy The atomic force microscope (AFM) has been extensively used to study the mechanical properties of soft materials and biological samples at nanoscale [25], particularly important for cell mechanics characterization [38]. It consists of a flexible cantilever with a nanometer-sized tip that is brought in contact with the sample to induce a deformation. Thus, the cantilever deflection is detected with high precision using a laser, and as the cantilever stiffness is previously calibrated, the force can be obtained [38]. Specially useful to study stiff materials, its contact mode can map a material stiffness at different surface points [39], whereas its dynamic mode, where the cantilever is excited harmonically, can provide a measure of the frequency-dependent storage and loss modulus [40].

Surface Force Apparatus Surface force apparatus (SFA) have been widely used to study adhesive and cohesive forces [41]. It uses multiple beam interference fringes to measure separation and deformation of a material between two surfaces while measuring normal forces as low of 10nN, with a spacial resolution of Angstroms ($\mathring{A}$). Typically, the sample is confined between two mica surfaces of cylindric shape that are brought together to apply a compressive load force ($\sim$1-10MPa). Then, the surfaces are separated and separation forces are measured, from which interactions such as Van der Waals forces, electrostatic forces and hydrogen bonds can be measured [41].

1.2.3 Selecting a microrheology technique

To select the adequate microrheology technique for an experiment one must consider the sample length-scale, the timescale during which the process of interest occur and the environmental conditions. For instance, to measure the rheological properties of a cell *in vivo*, a technique that allows to apply precise forces locally at microscale are needed. Then, an active approach must be consider over a passive technique, because the sample is not at thermal equilibrium. Further, if the experiment objective is to understand intracellular processes, a technique using optical tweezers will potentially offer more relevant information, as the probe will be embedded inside the cell, in contrast with atomic force microscopy, which typically probes only the cellular surface, or magnetic tweezers where the beads are commonly attached to the cell surface through ligands.

In this thesis, we will study two biological samples of different nature. The first, condensate droplets constituted by a polymeric molecule produced by the mussels. These condensates are known as biomolecular condensates, as they are made of biomacromolecules. In general, biomolecular condensates show a rich viscoelastic behavior, thus, we are interested in measure the dynamic viscoelasticity of our sample. Although the condensates can fuse and form a big condensed phase, we sought to understand the mechanical response of micron-sized droplets and the nature of the interactions that affect their behavior. As we are performing our experiments *in vitro*, we assume thermal equilibrium so we choose passive video particle tracking and active optical tweezers microrheology to obtain the viscoelastic modulus of the biomolecular condensates from probes embedded inside them, which can provide important insights about the internal rearrangement at different timescales. Other microrheology techniques like dynamic light scattering and surface force apparatus could provide information such as condensates size or adhesive forces respectively, however these are bulk properties that do not suit our experiment objective.

The second sample will be cells. We are interested in understanding the changes in the cytoplasm dynamics under conditions affecting one of their protein filaments, the microtubules. Thus, as mentioned above, an optical tweezers approach will be our choice to study the cell response and internal rearrangement at different rates by inducing deformation through an embedded probe.

Chapter 2

Microrheology of Mussel foot protein coacervates

2.1 Mussels: an inspiring model for new materials

A major challenge in designing adhesive materials, particularly in biomedical applications, is incompatibility with wet surfaces. While synthesizing moisture-resistant adhesives is possible, it requires elaborate and costly clean-room procedures [42]. In nature, however, marine mussels have evolved natural mechanisms to strongly attach themselves to rough surfaces under water. They do so by producing protein-based fibers, known as byssal threads, which tightly anchor to rocky seashores, overcoming the force of crushing waves. Byssal threads have been extensively studied and can be divided into different regions based on their function: the plaque, the core, and the cuticle. The strong adhesive interface occurs at the plaque. The core, a tough fiber composed of collagen-like proteins, exhibits self-healing properties and functions to dampen the effects of wave impacts [43]. The cuticle is a natural coating that protects the thread, characterized to present high extensibility, stiffness and hardness [44]; characteristics challenging to achieve synthetically as increasing hardness inherently reduces material extensibility [44]. Due to its remarkable properties, in recent decades there has been considerable interest in understanding and studying the composition and biofabrication process of the mussel byssus as it represents an important model for bio-inspired materials like underwater adhesives, self-healing

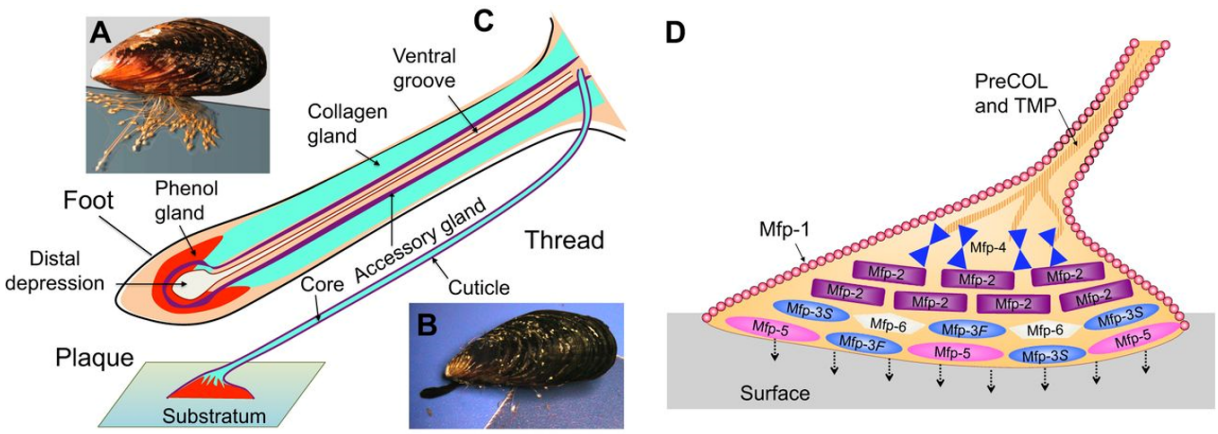

Figure 2.1: Overview of mussel adhesion to a surface. (a) The mussel byssus is a bundle of hundreds of threads attached to the mussel's body that attach to the surface. (b) The foot emerges from the mussel shell to sense the surface and place its tip where the new thread will be form. (c) Resembling an injection molding process, different precursor proteins are secreted within the ventral groove and distal depression of the foot for the assembly on a new thread. The three secretory glands: collagen, phenol and accessory gland are shown. When named by the portion of the thread they produce, they are referred as core, plaque and cuticle glands respectively. (d) Distribution of the different known byssal proteins (Figure adapted with permission from [10], Copyright ©2017, The Company of Biologists Ltd; permission conveyed through Copyright Clearance Center, Inc.)

materials and surface coating technologies.

2.1.1 Byssus formation

The byssus is a collection of threads (Fig.2.1a), each one divided in three parts with different mechanical properties: the plaque, where the strong adhesive interface with the surface occurs; the distal end, exhibiting high stiffness; and the proximal, with higher extensibility and attached to the mussel's body [10]. Byssal threads are produced one at a time by a retractile tongue-like shaped organ known as the foot. Emerging from the mussel's shell, the foot explores surfaces until finding a suitable one, where it plants its tip and becomes rigid to initiate thread production (Fig.2.1b) [45]. The foot features a groove in its ventral surface that extends from its base to the tip, ending in the so-called distal depression [45]. Resembling an injection molding process, thread formation occurs in the ventral groove

where several proteins are secreted by three major glands along the foot during the thread's formation (Fig.2.1c). In this manner, the foot functions as a controlled factory that releases specific amounts of their contents at specific order to achieve the defining characteristics of the threads at different sections. Before the thread leaves the groove, it is coated by the cuticle for protection, upon which is released in full contact with the seawater.

2.1.2 Byssus proteins

The byssus comprises over 20 proteins stored in secretory vesicles within the glands along the foot (Fig.2.1c). Although the glands are known by different names, I will adopt the nomenclature based on the part of the byssus they produce: the core, cuticle and plaque glands [46]. The plaque gland surrounds the cup-like shape distal depression of the foot, secreting the, at least 7, proteins involved in the adhesive interface and plaque formation, the Mussel foot proteins (Mfp), numbered based on their discovery (Mfp-2,Mfp-3, etc.)[43]. The core gland is localized along the length of the foot groove and it secretes the different prepolymerized collagens (preCols) and thread matrix proteins (TMP) that form the thread fibers. The cuticle gland secretes the Mfp-1, the primary protein for coating formation (Fig.2.1d)[10]. A distinctive hallmark of Mfps is their cationic nature and enrichement with the post-translational modification of Tyrosine 3,4-dihydroxyphenylalanine (DOPA). Several studies recognize the presence of DOPA as essential for the adhesive and mechanical properties of the plaque through interactions such as H-bonding, π-π interactions, π-cation interactions, cross-linking, and metal coordination [44, 47, 48].

2.1.3 Role of Liquid-liquid phase separation in byssus formation

An extensive characterization of the byssus thread attributes their material properties to its complex hierarchical structure at multiple length scales (Fig.2.2) [43]. Although the mussel fabrication process to achieve such organization is not fully understood yet, recent studies

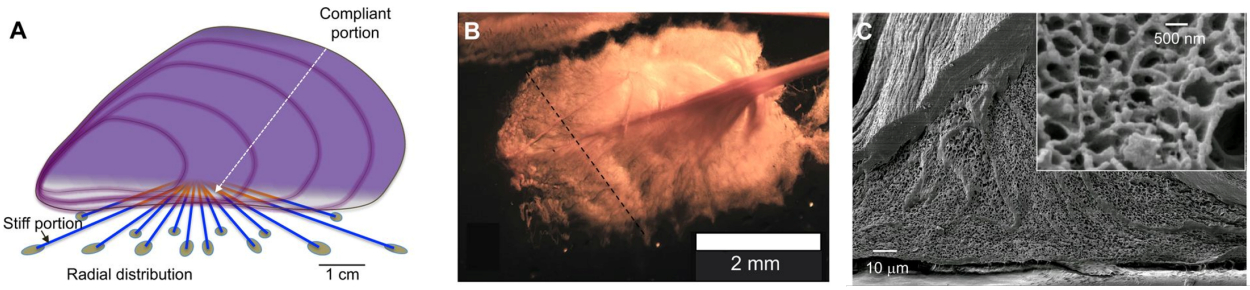

Figure 2.2: Hierarchical structure of the mussel's plaque: (a) Mussel threads with a radial distribution signaling the different mechanical properties of the dystal (stiff-blue) and proximal (compliant-orange) ends. (b) The spatulate geometry of a byssal thread and plaque [dashed line shows orientation of section for scanning electron microscopy (SEM) shown in (c)]. (c) Porous structure of a plaque in SEM section. (Figure adapted with permission from [10], Copyright ©2017, The Company of Biologists Ltd; permission conveyed through Copyright Clearance Center, Inc.)

suggest that they use fluid protein condensates as precursors for the assembly of the protein fibers outside their body (Fig. 2.3a) [49, 50].

Protein condensation involves a phase transition called liquid-liquid phase separation (LLPS). This phenomenon occurs when an homogeneous aqueous solution divides into two liquid phases, each with different concentrations of the components in the initial mixture (Fig. 2.3b). In general, LLPS is a thermodynamically driven process that occurs when the physical interactions of the components in the demixed state of the solution consume less energy than that required to mix them [51]. These interactions are mainly electrostatic (Fig. 2.3c), thus can be tuned by changing the solution conditions like temperature, ionic strength , concentration or pH. It is a well studied phenomenon in polymer science [52], and colloidal chemistry [53] where it is known as coacervation. Under this terminology, the more concentrated component, is called the coacervate, while the remaining phase, which is more diluted, is referred as the equilibrium solution [53].

In the past decades, liquid- liquid phase separation has become a major research focus subject in biological systems, as several membrane-less organelles and compartments inside the cell are now identified to be liquid phases of different biomolecules, named biomolecular

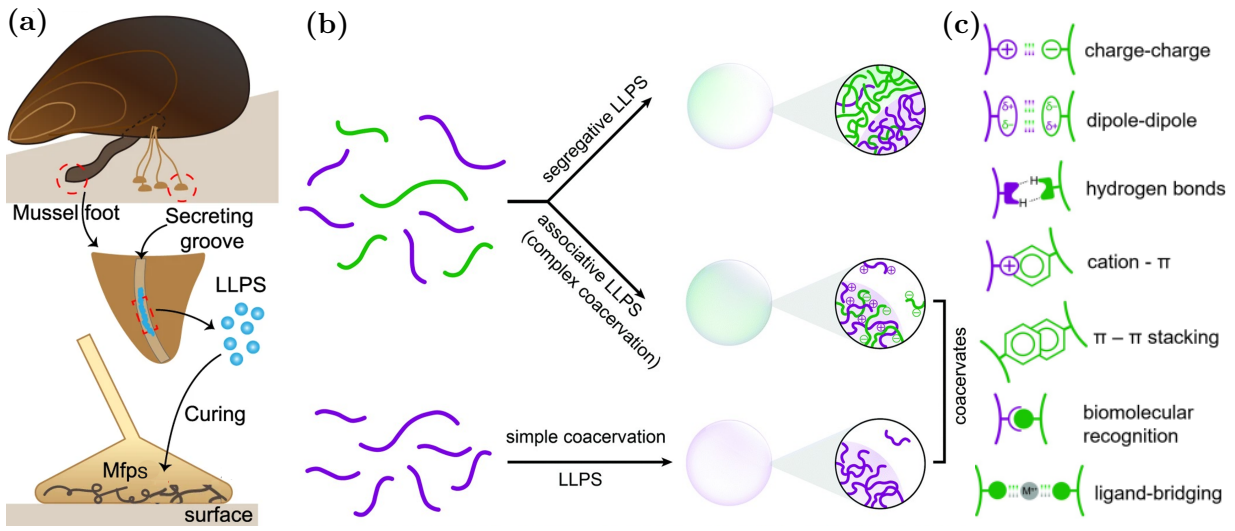

Figure 2.3: Liquid-liquid phase separation in mussels. (a) Schematic of the secretion and transport of proteins inside the foot groove via LLPS. (b) Types of liquid–liquid phase separation: segregative, occurs when two molecules do not mix due to repulsive interactions between them, producing two phases enriched with one of the solutes; associative, occurs when there are attractive interactions between two molecules so they form a phase rich enriched in both solutes; simple coacervation, where a single molecule presents attractive forces that trigger a condensed face under specific conditions of temperature, pH and salt concentration [56]. (c) Recognized interactions involved in the formation of coacervates (Figure (a) is an excerpt adapted of the original figure from [48] licensed under the Creative Commons Attribution CC BY 4.0, Copyright ©2022; figures (b) and (c) adapted from [56] with permission from the Royal Society of Chemistry, Copyright ©2019;permission conveyed through Copyright Clearance Center, Inc.)

condensates[3]. Among the biological processes where LLPS has being recognized to be a fundamental regulator are: surface adhesion, cellular compartmentalization, self-assembly and vesicle formation [54]. Moreover, in light of this renewed interest in LLPS, video particle tracking and optical tweezers-based microrheology have emerged as valuable techniques to asses the material properties of biomolecular condensates, as they offer an easier way to probe their inner contents [55].

Furthermore, the extensive new research on LLPS has shown that these liquid-like phases exhibit viscoelastic properties that in some cases can mature into solid-like structures over time or under specific triggers [55], a catastrophic trade that can lead to disease if present in cellular processes, but a relevant characteristic in the context of liquid phase precursor

proteins that tend to harden to assemble into complex structured materials. Additionally, condensation and coalescence of precursor proteins once they are secreted inside the foot groove are believed to offer several advantages to the adhesion process. First, the condensed phase could function as a mechanism to prevent the rapid diffusion of secreted proteins in aqueous environments; second, it facilitates distribution of high protein concentrations along the groove; and third, due to the coacervate low interfacial tension, it aids the mixture to spread over the desired surface target [54].

2.1.4 Motivation and objective

In recent years, much effort has been made to understand the fundamental physical and chemical principles underlying the coacervation of different mussel foot proteins (Mfps). For instance, surface force apparatus (SFA) has been used to measure the adhesive forces of Mfps coacervates and uncover the important role of DOPA in modifying their mechanical properties [41]. Nonetheless, these measurements are conducted at the ensemble level as they require the full condensed coacervate settled onto a mica surface.

Currently, it is hypothesized that precursor proteins within the vesicles are stored as fluid condensates under acidic and reducing conditions [10, 50, 57]. In particular, a recent *in vitro* study [50] found that upon rupture of plaque vesicles, their contents underwent multiphase liquid-liquid phase separation (LLPS). This multiphase entity showed the formation of nanodroplets that coalesced and gradually solidify forming a porous microstructure. Changing the buffer conditions revealed that solidification of the phase separated proteins always occurred above pH 6 within 2 s. Below that threshold, the condensates dissipated into the solvent in seconds. Interestingly, the addition of sulfate anions stabilized the condensate phase at acidic pH preventing its dissipation, and above pH 6 the solid structure showed more numerous and smaller pores. On the other hand, the addition of chloride anions did not form nanodroplets, producing a more homogeneous

condensate, and it was unable to avoid diffusion at pH below 6. These observations highlight that pH variation and the presence of specific anions, such as sulfate, are critical factors influencing multiphase separation and its transition to solid. Furthermore, these findings portray the necessity of studying Mfps condensed phases at microscale to elucidate their dynamic transition from the storage phase into complex structured materials.

As a result, the project presented here emerged as part of a broader interdisciplinary effort to investigate further, and in a controlled manner, the critical role of pH and sulfate ions in the coacervation of cationic byssus proteins, and their subsequent solidification into functional materials. Due to the challenges that represent obtaining enough native MFPs for experimentation, a recombinant approach to produce the protein was used. The complete study aims to characterize the composition, structure, and dynamic mechanical properties of condensates of a recombinant truncated form of Mfp-1, the most well-studied cuticle protein. Mfp-1, from the *Mytilus edulis* species, consists of about 80 repeats of the decapeptide consensus motif $[\text{AKPSYPPTYK}]_n$ where the lysine(K) residues provide an hydrophilic character and the tyrosine (Y) residues present a rich DOPA conversion. Additionally, a less hydrophilic non-repetitive domain is present at its N-terminus. [58]. In comparison, the recombinant truncated Mfp-1 (rMfp-1) contains only 12 tandem repeats, lacking DOPA and the non-repetitive domain. In the cuticle, DOPA is believed to have a cohesive role for Mfp-1 though dopa-metal cross-links [59], thus we can expect the rMfp-1 to show less cohesion than the native protein. Nonetheless, this rMfp-1 has already been shown to undergo LLPS *in vitro* in the presence of NaCl at seawater concentrations, via pi-cation interactions [60], which means the absence of DOPA does not prevent LLPS, our main object of study. In addition, DOPA oxidation entails experimental challenges as it associates with protein aggregation and limits the pH conditions of the experiments [61]. Thus, using rMfp-1 offers a more controlled experimental environment.

Particularly, the measurements pertained to this thesis correspond to the mechanical characterization of the rMfp-1 coacervates. Given the necessity of studying the condensates

dynamics at microscale, we proposed to apply video particle tracking microrheology, and adapted a previously developed multiharmonic OT-based microrheology technique [8], to measure the viscoelastic moduli of micron-sized recombinant Mfp-1 condensates. Because identifying the particular chemical stimuli that drive phase separation and solidification is difficult given the interaction of numerous proteins and molecules within the mussel foot, we will focus in analyzing independently the interplay of the two aforementioned stimuli: pH and salt type (or anion type). We measured the viscoelastic moduli of rMfp-1 condensates induced by the addition of: 1)Na_2SO_4 (a divalent anion); or 2)$NaCl$ (a monovalent anion); while varying the pH from $\sim$2 to $\sim$ 8. Hence, we were able to track the combined stimuli effects in the condensate's rheological properties under conditions that simulate the protein storage, and seawater environments respectively.

Unlike surface force apparatus, the multiharmonic OT-based method we present here allow us to probe the condensates viscoelasticity across a wider range of different timescales simultaneously, thus providing important new information about the network dynamics such as the characteristic timescales for internal molecular motion or identification of liquid-to-solid transitions [62]. Uncovering this knowledge is necessary for a deeper mechanistic understanding of the pH and salt effects in modulating the Mfps self-assembly process. By dissecting this information, and combining it with the condensates structure and composition characterization, new insights about the triggers and conditions that lead to hierarchical structure formation of the mussel byssus would be obtained. This information will be specially valuable for the bio-inspired design and engineering of sustainable polymeric materials with multi-scale structure, which have a wide range of applications from tissue adhesives, drug delivery encapsulation systems, to coatings for flexible electronics [43, 63, 64].

2.2 Methodology

To asses the rheological properties of rMfp-1 condensates, we used optical trapping-based microrheology. To validate the active method, we performed video particle tracking (VPT) passive microrheology on glycerol-water solutions at different volume concentrations and compared them to active optical trapping measurements. Glycerol behaves as a pure viscous solutions, and the viscosities for solutions of different glycerol concentrations can be found in the literature to compare with the viscosities estimate by the active microrheology. Also, as a complementary assessment to the active measurements of rMfp-1 , VPT was performed when there were multiple beads inside of the condensate to enable a reliable estimate of the average displacement.

2.2.1 Protein

Experiments were performed following a previously developed protocol reported in [65], using a recombinantly expressed truncated form of the mussel foot protein 1 (Mfp-1) comprised of 12 tandem repeats of the decapeptide AKPSYPPTYK, referred from here on as rMfp-1. The plasmid to produce rMfp-1, a gift from Dr. Dong Soo Hwang (Pohang University of Science and Technology), was transformed into *Escherichia coli* [BL21 (DE3)], which was cultured in 100mL of Terrific Broth (TB) medium with 50 μg/mL kanamycin sulfate at 37°C and 160 rpm until the optical density at 600 nm (OD600) reached a value of 0.6. The resulting stock was used to innoculate 10L of TB that was incubated also at 37°C and 160 rpm until the OD600 reached a value of 0.6. Then, the rMfp-1 expression was induced by adding 1 mM of isopropyl-β-D-1-thiogalactopyranoside (IPTG) and the *E.coli* was left to express for 5 hours in the same conditions. Expression was monitored every 2 hours via SDS-PAGE and after the 5 hours cells were collected by centrifugation at 5000g at 4°C for 10 minutes. The pellet was weighted and stored in a plastic bag at -80°C.

rMfp-1 is expressed in *E.coli* as dense, insoluble aggregates called inclusion bodies. To purify it, the frozen pellet was mechanically broken by hitting it with a hammer several times to obtain smaller pieces that were subsequently added to a beaker. 4mL of TNE per gram *E.coli* were added and then the mix was stirred to defrost and resuspended at 37°C. Once resuspended, 80 μL of lyzosome solution (egg lysozome prepared in TNE at 10mg/mL) per gram *E.coli* was added, followed by a 30 minutes incubation. Once the solution became more viscous, the beaker was stored at -20°C until freezing of the solution. The process was repeated two more times from the lyzosome addition step. Disruption of unlysed cells was done using a probe sonicator while the solution was kept on ice (Sonic Dismembrator Model 500, Fisher Scientific) operating at 75% amplitude, at a cycle of 6 seconds on:4 seconds off, during 5 minutes. The solution was centrifuged at 12000 rpm for 20 minutes and the pellet was resuspended in a TNE refrigerated solution with 2% Triton. Then, the solution was homogenized with a Teflon pestle and mortar, followed by another round of sonication with the same parameters. The wash process by centrifugation, resuspension and homogenization of the resulting solution was repeated several times until the supernatant showed no visible color (originally yellow). Once this point was reached, the resuspension solution was change to TNE with 2M urea and the wash repeated once. Next wash was resuspended in TNE alone, and final wash was done using Milli-Q water, yielding a pellet of pure inclusion bodies.

Next, the pellet was resuspended in Mili-Q water and homogenized with teflon pestle and mortar, followed by sonication, and then transferred to a beaker. Solubilization was achieved by adding glacial acetic acid over a 30 minutes span under constant stirring until reaching a final concentration of 20% acetic acid. The solubilization was run for 24 hours, and the solution was then centrifuged at 12000 rpm for 20 minutes. The supernatant containing the rMfp-1 was collected and centrifuged in batches using an Amicon Ultra filter (15 mL, 10 kDa MWCO, Sigma). The retained rMfp-1 was purified using prep-scale HPLC (Discovery BIO Wide Pore C8 column, 10 μm particle size, 250 mm $\times$ 21.2 mm, Supelco) with the gradient elution of water and acetonitrile. Pooled fractions were flash frozen in liquid nitrogen and

lyophilized for 24 hours, producing pure rMfp-1 as a granulated powder. Finally, rMfp-1 powder was stored in an airtight container at -20 °C. Purity was confirmed by SDS-PAGE and mass spectrometry.

2.2.2 Preparation of PEG-coated beads

Adapting the protocol from reference [66], amine-terminated methoxypoly(ethylene glycol), mPEG-NH2(Sigma-Aldrich), was covalently coupled to 500nm yellow-green (505/515) carboxylate-modified polystyrene beads (FluoSpheres^{TM} F8813, Invitrogen) using carbodiimide chemistry. 285μL of beads were washed with deionized(DI) water 3 times by centrifugation at 20000 rcf. Washed beads were resuspended in 3mL of DI water and sonicated for 10 minutes. Then, they were loaded into a previously hydrated dialysis cassette (Slide A-Lyzer^{TM} 3.500 MWCO, 66330, Thermo Scientific). First the cassette was submerged in 400mL of MES buffer(100 mM 2-(N-morpholino)ethanesulfonic acid, Bio Basic) with pH 6 for 2 hours. After that time, the casssette was transfered into fresh 400 mL MES containing 60μM of mPEG-NH2 for 45 minutes. EDC (Bio Basic) to a final concentration of 1.2mM and NHS(Bio Basic) to a concentration of 2.4 mM were added to the PEG-MES in which the bag was, and left for 30 minutes. Then the solution was rinsed by submerging the cassete into fresh 400mL MES buffer for 10 minutes. Subsequently the bag was submerged in 400 mL of borate buffer(50mM boric acid plus 36mM sodium tetraborate, ph 8.5) with 60μM mPEG-NH2 added. After 30 minutes NHS was added to the PEG-borate solution to a concentration of 2.4 mM and was left for 16 hours under continuous mixing. The solution was then washed by submerging the cassette in 400 mL of fresh borate buffer for 2 hours. Finally, the beads were recovered from the cassette and washed with DI water 2 times by centrifigation at 20000 rcf; to be finally resuspended in 1mL PBS 1X(Wisent Inc.) and stored at 4°C. During all the steps of the reaction, the buffer's container was covered with aluminum foil to prevent photobleaching of the beads

and the solution was under constant agitation to prevent bead aggregation.

2.2.3 Sample preparation

Glycerol solutions were prepared by mixing glycerol (Fisher Scientific) and purified water to achieve 50%, 60%, 70%, and 80% (v/v) concentrations. 500nm yellow-green (505/515) carboxylate-modified polystyrene beads (FluoSpheres^{TM} F8813, Invitrogen) were added as probes to a low concentration ($\sim 10^5$ particles/mL). For the protein samples, LLPS of rMfp-1 was induced by adding 0.6M $NaCl$ or 0.4M Na_2SO_4 to a solution of purified rMfp-1 in 0.1 M sodium acetate buffer at different pH (2-8). Final protein concentration was 100 mg/mL. Microrheology tests were done using PEG-coated beads (see protocol in section 2.2.2), to prevent surface interactions with the protein. Beads were added at low concentrations to the buffer after adding the protein and were vortexed around 10 seconds. Then, the salt was added and everything was mixed by vortexing another 5 seconds. To accelerate the condensation process, the sample was centrifuged for 2 minutes at 12 000 rcf and the dilute and dense phase were mixed using a pipette.

To visualize the samples in the microscope, a chamber was made by gluing two double-sided tape pieces to a glass slide (dimensions: 25×75mm, thickness: 1 mm, Globe Scientific, 1331) at the same distance to create a channel. Then a line of vacuum grease (Dow Corning High Vacuum Grease) was added to the channel edges, and a microscope coverglass (dimensions: 22×30mm, thickness: #1.5 (0.16 to 0.19 mm), Fisher Scientific, 12-544A) was put on top and pressed to close the chamber. Next, around 20μL of the sample was flowed inside the chamber and the open sides were sealed using vacuum grease to prevent sample evaporation. Condensates samples were left to equilibrate until no more droplet fusion was seen under the microscope (∼15 minutes).

2.2.4 Video particle tracking passive microrheology

Video particle tracking was done using an inverted microscope (Nikon Eclipse Ti-E) customized for Total Internal Reflection Fluorescence (TIRF) with a 1.49 numerical aperture oil-immersion 100x objective. Fluorescent beads were excited using a 488nm diode laser at 1 mW (Coherent OBIS Laser box). The bead's trajectories were imaged with a EMCCD camera (iXon U897, Andor Technology) and videos were recorded using NIS-Elements acquisition software (Nikon) with a pixel size of 0.16μm. An exposure time of 20ms was used for glycerol solutions and 100ms for rMfp-1 condensates. Tracking of the tracers was done using FIJI's plugin TrackMate [67, 68, 69].

2.2.5 Data Analysis for passive measurements

First, the trajectories were analyzed using custom-built MATLAB[70] scripts to obtain the mean square displacement at different delay times according to equation 1.23. For different condensates in the same sample, the MSD associated to each condition was computed as an average of the MSD from the tracks measured across all the condensates. The MSD behavior of the samples in the frequency range analyzed was linear, so the free diffusion equation 1.24 was fitted to the two-dimensional MSD curve, for both the glycerol dilutions and the rMfp-1 condensates. The steady-state viscosity was obtained from the diffusion coefficient using equation 1.25. Next, the viscoelastic moduli of the samples were computed implementing the algorithm proposed by Evans [27, 71]. This algorithm takes advantage of the linear relation between the creep compliance and the MSD in the time domain and computes its Fourier transform numerically.

2.2.6 Optical tweezers based active microrheology

Active microrheology was performed on a custom-built optical tweezers system mounted to the same inverted microscope used in section 2.2.4. A near-IR laser (1064 nm, 10 W, IPG Photonics) was collimated and expanded to over-fill the back aperture of the objective. The bead position relative to the trap center was measured using a lateral effect photodiode (Thorlabs) positioned conjugate to the back focal plane of the condenser objective.The trap position was controlled using an optoacoustic deflector (AOD) (AA Optoelectronics, DTSXY-400-1064, direct digital synthesizer driver) controlled through a field-programmable gate array and custom LabVIEW programs (National Instruments).The measurements on the protein samples were initiated once all the droplets were settled on the coverslip surface and there was no fusion present. Then, a bead embedded into a condensate was selected and trapped. We observed the formation of bubbles at high laser power, so used low laser powers corresponding to trap stiffness of ∼0.002-0.025 pN/nm. Beads were chosen to be away from the condensate's edges to avoid the effects of the condensate interface. Next a multicomponent (∼19 frequencies) excitation input wave was applied with a frequency range covering from ∼0.02 Hz to 1000 Hz with corresponding amplitudes ranging from ∼50 nm to ∼1 nm. The frequencies of oscillation were chosen at prime numbers to avoid subharmonics generation. The amplitudes were empirically selected to be small enough to remain in the linear response regime of the system and at the same time to provide a coherent signal. Measurements of the bead position signal and the laser input were recorded for 180 seconds at a sampling rate of 20 kHz.

2.2.7 Data Analysis for active measurements

Using custom-built MATLAB scripts, the frequency response function (FRF) of the bead displacement related to the AOD signal was computed using the *tfestimate* function based

on the Welch's method. To avoid leakage, at each frequency a specific window length is chosen to be an integer multiple of the period of the input. In addition, the power spectrum of the thermal response is computed using the data opposite to the direction of the oscillatory movement and filtering out the excitation frequencies, where the window length is chosen to obtain the best trade-off between frequency resolution and averaging. Next, the trap calibration is done following a previously developed method [8, 72, 73] where κ and β_{pd} are obtained for each individual measurement by fitting a simplified viscoelastic model simultaneously to the FRF and the power spectrum of the thermal response. Once κ and β_{pd} are known, by means of the relations 1.41 and 1.42, the response function due only to the material properties was obtained following [8]. Then the complex shear modulus is directly computed for each bead measured.

The statistical analysis of the measured complex modulus was done by drawing 1000 bootstrap samples from the dataset and fitting each bootstrap sample to the modified Jeffrey's model using the *lsqcurvefit* function. In this way, a distribution for each parameter of the model was obtained for each condition and the statistics was computed directly from the distributions of both, the parameters and the viscoelastic moduli.

2.2.8 Simplified viscoelastic model for calibration

In our system, the equation of motion describing a trapped bead due to the trap potential and relative to the trap position is given by the equation:

$$m(\ddot{x}_{trap})+\gamma_{mat}(\dot{x}_{trap})+k_{mat}(x_{trap}) = -m(\Delta\ddot{x})-\gamma_{mat}(\Delta\dot{x})-\kappa(\Delta x)-k_{mat}(\Delta x)+f_{thermal} \quad (2.1)$$

where $\Delta x(t) = x_{bead}(t) - x_{trap}(t)$, m is the bead mass, γ_{mat} is the friction coefficient of the medium (proportional to the viscous part of the medium), k_{mat} represent the spring constant of the material (proportional to the elastic contribution), κ is the trap stiffness, and $f_{thermal}$ represents the forces due to thermal fluctuations, with ($\langle f_{thermal}(t)\rangle = 0$) and

($\langle f_{thermal}(t) f_{thermal}(t')\rangle = 2k_B T\gamma_{mat}\delta(t-t')$).

Ignoring inertial effects, $m(\ddot{x}_{trap}) = 0$, for the passive calibration we consider the scenario where the trap is static $x_{trap} = 0$. By getting the Fourier transform of equation 2.1, the apparent complex response due to the force f_a, that comprises the thermal fluctuations and the trap stationary potential, is obtained (see Eq. 1.40):

$$\frac{\Delta X(\omega)}{F_a} = \frac{1}{\kappa + \gamma_{mat} j\omega + k_{mat}} = \chi(\omega) \tag{2.2}$$

In equilibrium, the fluctuation dissipation theorem relates the imaginary part of $\chi(\omega) = \chi'(\omega) + i\chi''(\omega)$ to the power spectral density by the relation:

$$P(\omega) = \frac{2k_B T}{\omega}\chi''(\omega) = \frac{2k_B T\gamma_{mat}}{|\kappa + \gamma_{mat} j\omega + k_{mat}|^2} \tag{2.3}$$

In general, for a viscoelastic material the terms γ_{mat} and k_{mat} depend of the frequency as $\gamma_{mat}(\omega)$ and $k_{mat}(\omega)$. Next, as the measurements read from the photodiode are in volts, the correspondent factor to convert to nanometers should be added to the power spectrum equation using the relation $P(\omega) = \langle X(\omega)^2\rangle = \beta_{pd}^2 \langle V_{pd}(\omega)^2\rangle$. Then, the power spectrum function to be fitted to the experimental data is:

$$\left\langle V_{pd}(\omega)^2 \right\rangle = \frac{1}{\beta_{pd}^2} \times \frac{2k_B T\gamma_{mat}}{|\kappa + \gamma_{mat} j\omega + k_{mat}|^2} \tag{2.4}$$

For the active calibration part, $x_{trap} \neq 0$. Neglecting inertial forces ($m(\ddot{x}_{trap}) = 0$) and considering average over thermal noise ($\langle F_{thermal}\rangle = 0$), the Laplace transform at steady state ($s = j\omega$) was applied to both sides of equation 2.1 to obtain the transfer function $H(\omega)$ between the output and input signals:

$$H(\omega) = \frac{\Delta X(\omega)}{X_{trap}(\omega)} = \frac{\gamma_{mat} j\omega + k_{mat}}{\kappa + \gamma_{mat} j\omega + k_{mat}} \tag{2.5}$$

Adding the correspondent conversion factor to nanometers using the relation $V_{pd}(\omega)\beta_{pd} =$

$\Delta X(\omega)$, the transfer function to be fitted to the experimental data is:

$$H(\omega) = \frac{V_{pd}(\omega)}{X_{trap}(\omega)} = \frac{1}{\beta_{pd}} \times \frac{\gamma_{mat} j\omega + k_{mat}}{\kappa + \gamma_{mat} j\omega + k_{mat}} \tag{2.6}$$

From the transfer function fit to equation 2.6 and the power spectrum fit to 2.4 the calibration factors β_{pd} and κ are obtained. Following [8], the experimental transfer function $H(\omega)$ can be related to the apparent response function $\chi(\omega)$ as :

$$\chi(\omega) = \frac{1}{\kappa}[\beta_{pd} H(\omega) + 1] \tag{2.7}$$

from where the response function due to the material only,$\alpha\,(\omega)$, can be obtained now using 1.41, $\alpha\,(\omega) = \chi\,(\omega)\,/1 - \kappa\chi\,(\omega)$, and finally, the $G^*(\omega)$ from the material is computed using 1.42:

$$G^*(\omega) = \frac{1}{6\pi R \alpha(\omega)} \tag{2.8}$$

Applying 2.8 to the apparent response function $\chi(\omega)$ instead, we can obtain the apparent complex moduli $G^*_a(\omega)$ due to the material properties plus the trap effect which can be written as:

$$G^*_a(\omega) = \frac{1}{6\pi R}[\kappa + \gamma_{mat}(\omega) j\omega + k_{mat}(\omega)] = \frac{1}{6\pi R}[\kappa + G^*(\omega)] \tag{2.9}$$

We used expression 2.9 to simulate the behavior of the experimental transfer function and power spectrum for a simple viscoelastic model, with $\gamma_{mat}(\omega)$ and $k_{mat}(\omega)$ constants, and for a Maxwell and Jeffrey model using their corresponding expressions of $G^*(\omega)$ and the experimental conditions for β_{pd} and κ. The simulation showed that the behavior of the power spectrum corresponding to the simple viscoelastic model only differs significantly at high frequencies to the Jeffrey's model 2.4b. In consequence, just frequencies below $\sim$30Hz were considered for the calibration as showed in figure 2.7e.

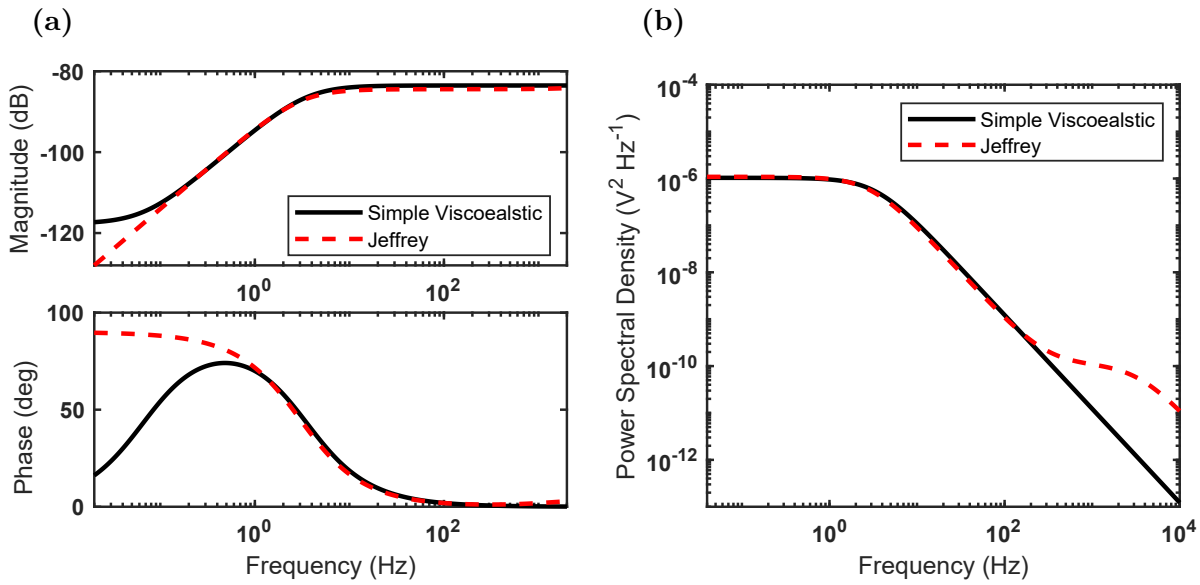

Figure 2.4: Simulated transfer response function and power spectrum: (a) Transfer function magnitude and phase, and (b) power spectral density comparison from the simple viscoelastic model and the Jeffrey model. The correspondence between the pole in the magnitude plot and the corner frequency in the power spectrum is preserved in both models, which is exploited in the calibration procedure by fitting the simple model in the frequency ranges that the models behave similarly. Parameter values used $\kappa = 0.01$ pN/nm, $\beta = 15000$ nm/V, $\eta = 0.1$ Pa·s, $\omega_c = 2\pi f$ with $f = 30$Hz, $\tau_c = 1/\omega_c = 0.0053$ s and $E = \eta/\tau_c = 18.85$ Pa.

2.3 Results

2.3.1 Active and passive calibration using a viscous fluid

Dilutions of glycerol were used as viscous Newtonian fluids to compare active and passive microrheology methods. We conducted VPT passive microrheology on glycerol dilutions of 50%, 60%, 70% and 80% (volume/volume) concentrations. As the glycerol concentration increased, the displacement of embedded particles shortened due to higher viscosity, as expected. This trend is illustrated in Figure 2.5a, where longer displacements are observed for the less viscous condition of 50% glycerol. Additionally, a higher number of shorter tracks in the 50% solution indicates faster mobility, as beads move out of camera focus more frequently. The decrease in displacement is quantified in the MSD plots. Figure 2.5b shows a linear relationship with the time delay τ at a timescale of seconds, consistent with

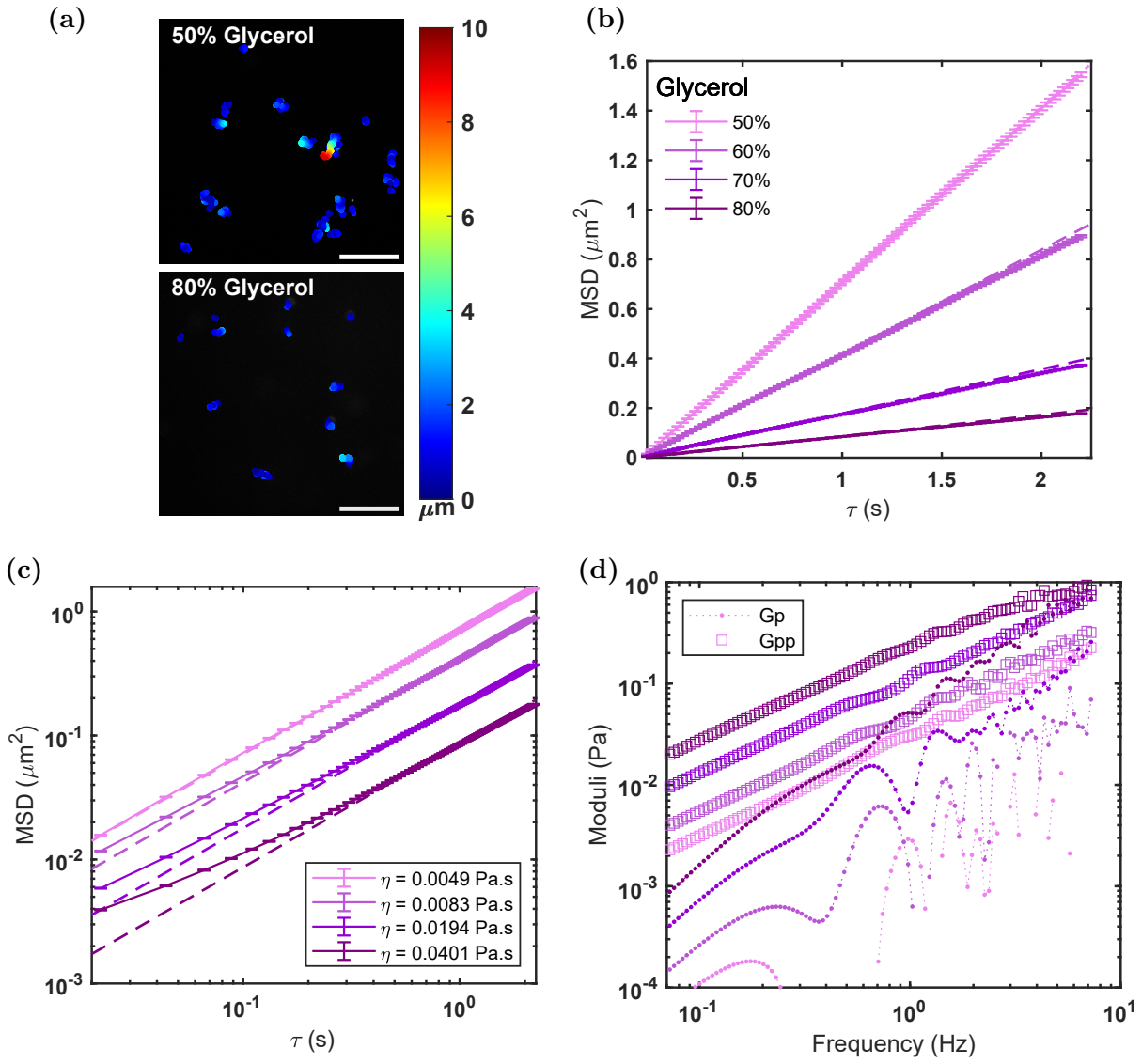

Figure 2.5: Video particle tracking microrheology of glycerol solutions. (a) Passive track examples for 50% and 80% glycerol concentrations; colorbar represents the total displacement in μm, scale bar = 20μm. (b) MSD of glycerol solutions at different volume concentrations; the dashed line represents their fit to the equation $\langle \Delta r^2(\tau) \rangle = 4D\tau$; (c) logarithmic representation of MSD data where the tracking error effects can be observed at short delay values; (d) Corresponding viscoealastic moduli using the GESR relation 1.28. The error contrubution from the short delay times can be observed at high frequencies were the moduli behaves noisier and starts to deviate from the pure viscous model expected behavior.

the Newtonian model (Eq. 1.24). However, the logarithmic representation in Figure 2.5c reveals the limitations of the method at shorter timescales, where increasing viscosity leads to tracking errors that deviate the MSD from the expected Newtonian model. Nonetheless, viscosity values obtained from the MSD fit and Stokes' relation (Eq. 1.25) closely match literature values for glycerol solutions at 25°C (Table 7 in [74]).

By applying the GSER (Eq. 1.28), we computed the viscoelastic moduli (Figure 2.5d). For a viscous Newtonian fluid, the storage modulus should theoretically be zero. In practice, the passive results show an increasing storage modulus that correlates with the tracking error present. However, its magnitude is lower than the viscous contribution. At low frequencies, the loss modulus G" aligns with the linear relation between frequency and viscosity predicted by the Newtonian model. At higher frequencies, errors from MSD measurements cause an apparent curvature in G".

To extend measurements across a wider frequency range, we optically trapped a single bead in the solution and applied multifrequency excitation to the trap position. We used the passive and active response of the bead to the trap movement, to compute the viscoelastic moduli. Then, we compare it to the results obtained with the passive method (Figure 2.6 and Table 2.1). The storage modulus exhibits a behavior consistent with a constant elastic modulus at 50%, 60% and 70% glycerol solutions. For the most viscous solution, a plateau is maintained at frequencies below 10 Hz, followed by a linear increase. The loss modulus shows some variability at low frequencies (<0.1 Hz) but follows a linear relation at higher frequencies.

Two important observations can be made from the different methods. First, both describe the loss modulus linearly, consistent with the Newtonian model, but the active method consistently shows lower magnitudes compared to passive data, likely due to laser-induced heating of the trap. Second, the storage modulus dominance in active measurements at lower frequencies (<1Hz) contrasts with the expected liquid behavior dominating across all frequencies, which is better described by the passive measurements. This difference may

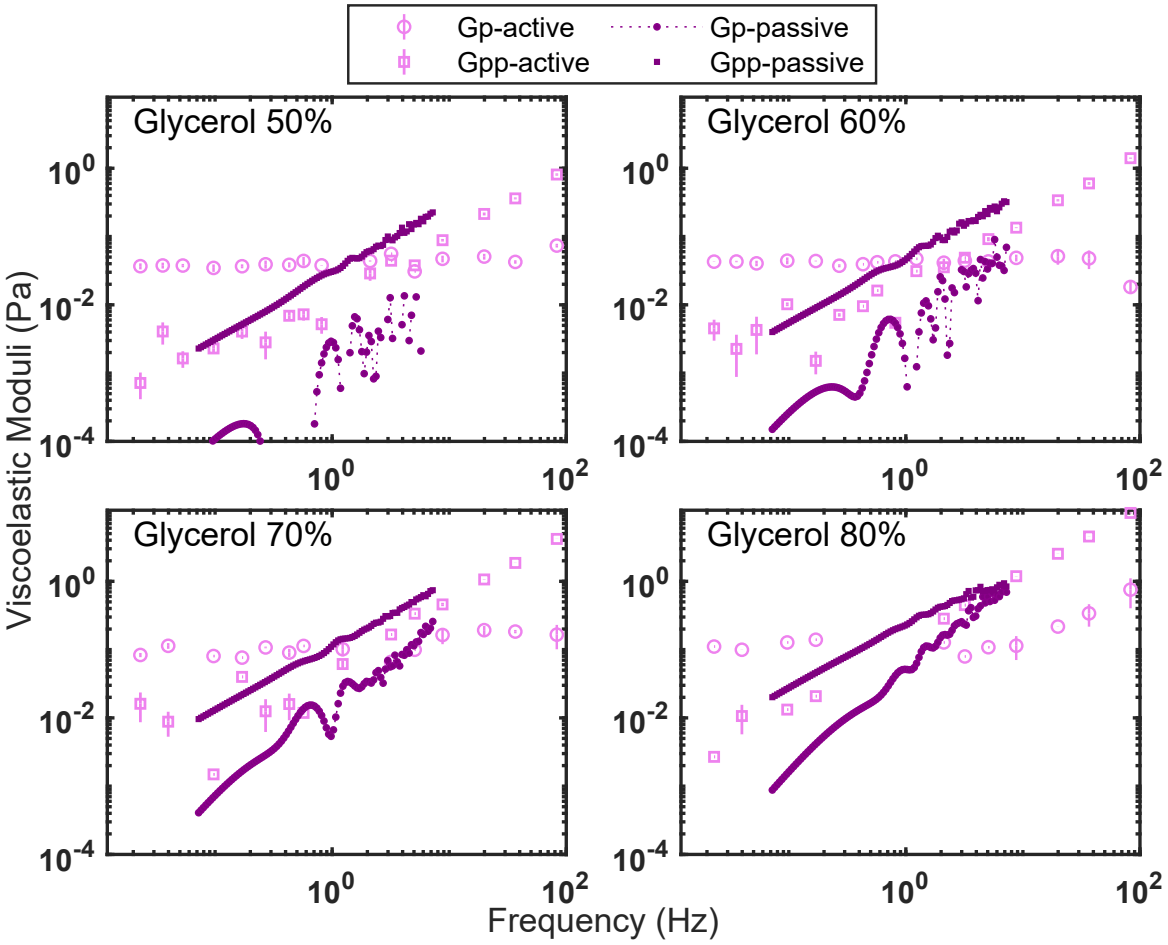

Figure 2.6: Active vs passive microrheology of glycerol solutions. Comparison of viscoelastic moduli of glycerol solutions at different volume/volume dilutions in water, obtained by VPT passive microrheology, and OT active microrheology. The behavior of the loss modulus G" is consistent in both cases although the magnitude of the active measurements show a lower value compared with the passive method. The elastic modulus G" shows a constant plateau only in the active measurements while the passive shows a constant decrease as frequency decreases.

arise from various factors. For instance, the transfer function plot for a pure viscous liquid decreases linearly at low frequencies, but the measured transfer function reaches a plateau that could be determined by the sensitivity of the system itself. In consequence, this plateau might translate to an apparent elasticity of the material. Another possibility is the presence of surface tension effects or an incomplete separation of the trap stiffness contributions before obtaining the material viscoelasticity.

[Glycerol] (v/v)	Literature η(mPa·s)	Passive (VPT) η(mPa·s)	Active (OT) η(mPa·s)
50%	5.0	4.9	1.4
60%	8.8	8.3	2.1
70%	18.0	19.4	4.9
80%	45.8	40.1	19.4

Table 2.1: Glycerol viscosity results. Viscosity of glycerol solutions obtained using VPT and OT-based microrheology compared to literature values at 25° (Table 7 in [74]).

In summary, these measurements highlight the strengths and limitations of both microrheology techniques. VPT passive microrheology provides a straightforward approach to estimate viscosity in fluid-like samples with a good approximation to physical values, simultaneously exploring diffusion changes and their viscoelastic response at low frequencies. Yet, we should be careful to interpret the results as tracking errors may lead to inaccurate behaviors at higher frequencies. The optical tweezers-based active microrheology provides reliable information at higher frequency ranges that complements the loss modulus trend, with the disadvantage of consistently lower magnitudes than expected. The presence of an elastic modulus plateau at low frequencies, inconsistent with a viscous solution behavior, and not observed in passive measurements, suggests non-material origins. These insights will serve as a base to interpret further measurements in our samples of interest.

2.3.2 Optical trap-based active microrheology reveals rMfp-1 coacervates behave as a Jeffrey's fluid

Current models of byssus production suggest that the condensation of various adhesive proteins is an essential mechanism for fabricating and assembling the adhesive material outside the mussel's body. Previous studies indicate that Chloride (Cl^-) and Sulfate (SO_4^{2-}) anions play crucial roles in the LLPS (Liquid-Liquid Phase Separation) of different mussel foot proteins [50, 60]. To better understand their impact on the mechanical properties of coacervates, we employed an optical trap-based active microrheology

approach to investigate the mechanical changes in recombinant mussel foot protein 1 (rMfp-1) condensation triggered by two different salts: sodium chloride ($NaCl$) and sodium sulfate (Na_2SO_4). We also varied the pH from $\sim$ 2 to 8 to simulate the conditions inside (storage) and outside (seawater) the mussel environment.

We triggered rMfp-1 coacervation by adding 0.6M $NaCl$, or 0.4M Na_2SO_4, to a solution of 100 mg/mL rMfp-1 in acetate buffer containing 500nm PEGylated beads at pH values ranging from $\sim$ 2 to 8. Dense and dilute phases formed spontaneously (Fig. 2.7a). The solution was then mixed with a pipette to produce smaller condensates. We optically trapped a bead embedded in a condensate settled on a slide surface, as depicted in Figure 2.7b, and applied multiharmonic excitation to the trap position. A schematic of the simple viscoelastic model used for trap calibration is shown in Figure 2.7c, where elastic contributions are represented by a spring and viscous contributions by a dashpot. The active response of the bead to the trap movement is used to obtain the magnitude and phase of the transfer function at each excitation frequency, as illustrated in Figure 2.7d. The power spectrum (Fig. 2.7e) at low frequencies reflects passive response due to thermal fluctuations in the condensate, and is simultaneously fitted with the transfer function to the simple viscoelastic model to find the trap stiffness k_{trap} (pN/nm) and photodiode constant β_{pd} (nm/V).Upon completing the trap calibration, viscoelastic moduli of the condensate were computed by subtracting trap contributions from the transfer function. Additionally, the loss tangent is plot for better visualization of liquid-to-solid transitions across the studied frequency range (elastic $\tan\delta < 1$, viscous $\tan\delta > 1$).

In general, we observed a consistent trend in the viscoelastic moduli across all conditions studied. As shown in Figure 2.7f, the elastic modulus exhibited a plateau at lower frequencies, increased through an intermediate frequency range, and then maintained a constant magnitude at higher frequencies. The loss modulus linearly increased with frequency until reaching a crossover point with the storage modulus, after which it decreased to form a concave curve that rose again at the highest frequencies measured.

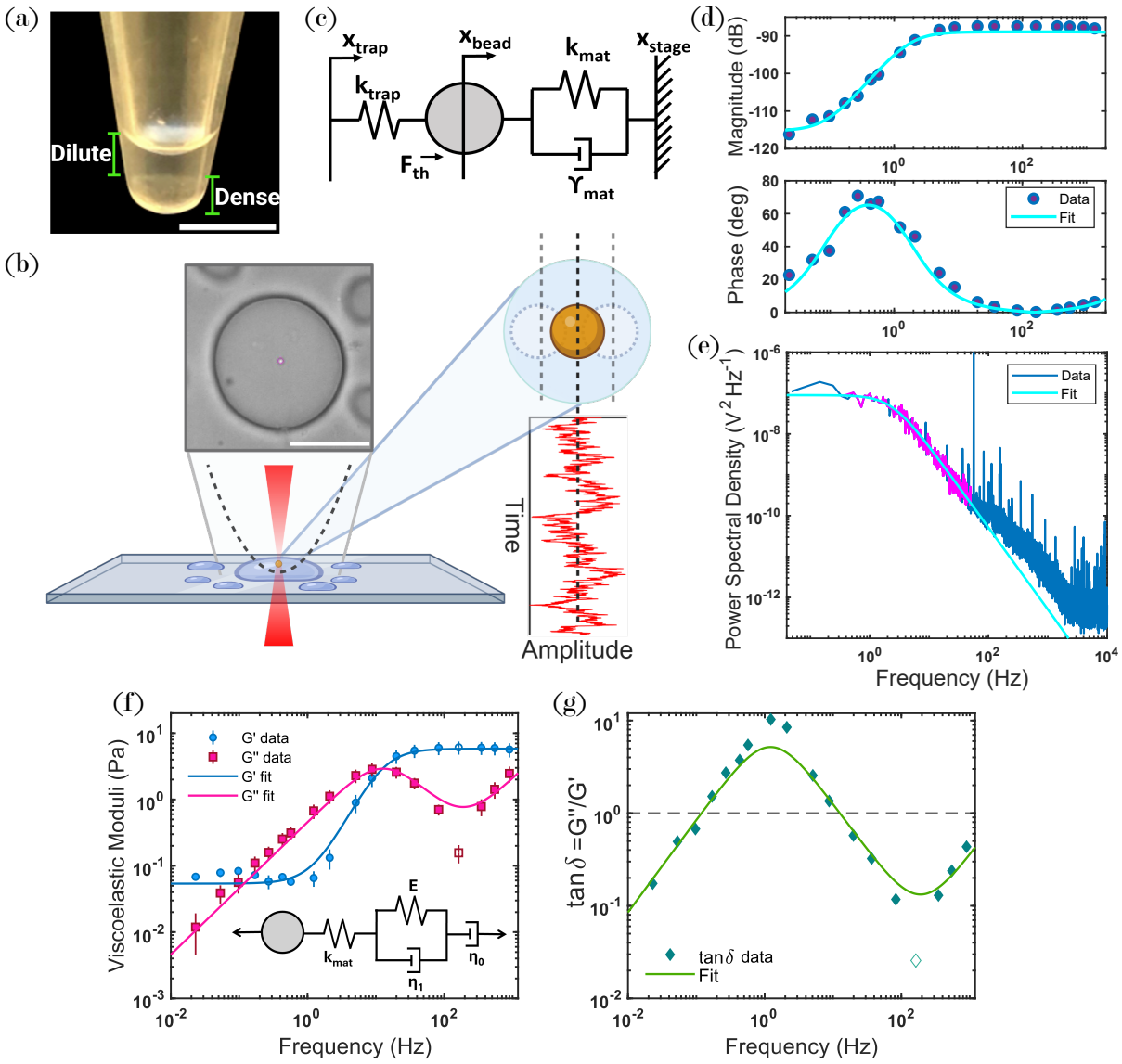

Figure 2.7: Active microrheology process in rMfp-1. (a) Phase separation of rMfp-1 in dense (bottom), and dilute fase (supernatant), scale bar = 5mm. (b) Optical tweezers based active microrheology setup: A bead is trapped by the optical harmonic potential in the middle of the droplet and a multiharmonic wave is applied in the X direction; a top view of the sample is shown with a scale bar of 10μm. (c) A diagram of the simple viscoelastic model used for the trap calibration, where k_{mat} and γ_{mat} were set constant.(d) Magnitude and phase of the transfer response function fitted to a simple viscoelastic model to obtain the trap stiffness k_{trap} (pN/nm) and the photodiode constant β_{pd}(nm/V). (e) The power spectrum of the fluctuations of the bead (blue). The low frequencies representing the thermal fluctuations (purple) are simultaneously fit to the passive part of the model. (f) Viscoelastic moduli obtained after subtracting the trap contribution and fitted to a modified version of the Jeffrey fluid model (inset);open symbols represent data omitted in the fit due to high noise. (g) Loss tangent showing the frequency range where the material is dominated by the viscous ($\tan\delta > 0$) or elastic ($\tan\delta < 0$) behavior. (Figure 2.7b created with BioRender.com)

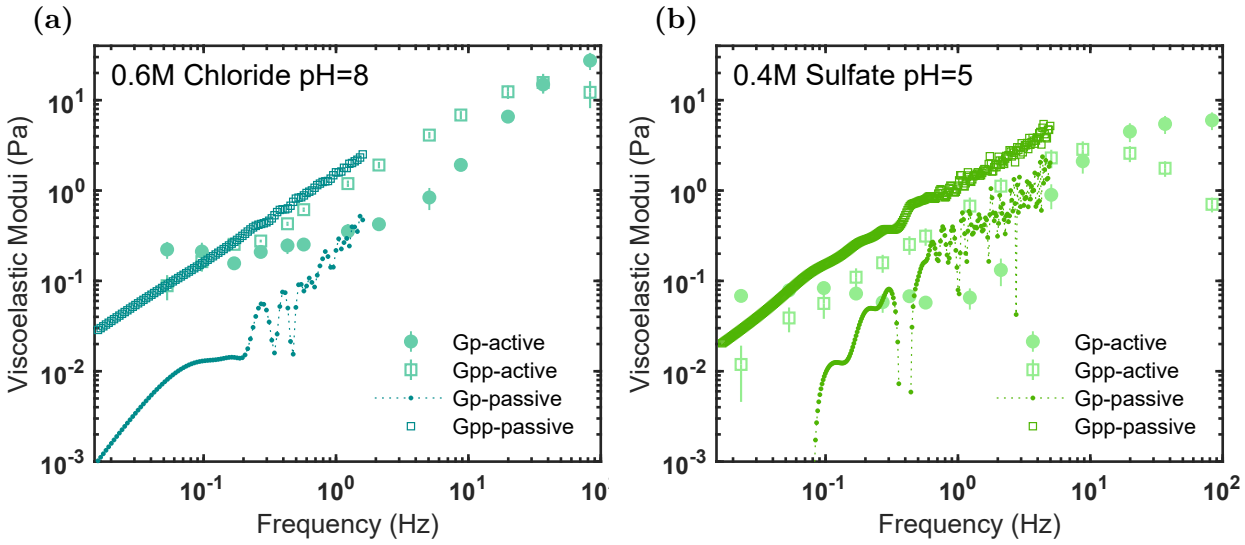

Figure 2.8: Active vs passive microrheology for rMfp-1 condensates. Frequency dependent moduli obtained by passive and active method: (a) 0.6M Chloride sample with ph=8 and $\eta = 252$ mPa·s from MSD fit. (b) 0.4M Sulfate sample with ph=5 and $\eta = 214$ mPa·s. In both cases the trend of loss modulus in the passive measurement is consistent with the active data but with a higher magnitude. The elastic modulus shows a plateau at lower frequencies for the active approach while in the passive seems to decrease.

Aside from the low-frequency elastic plateau, this behavior is consistent with the Jeffrey's fluid model (Eq. 1.22), which has been identified as suitable for describing several protein condensates [16, 75]. The observed low-frequency elastic plateau, consistent with the behavior previously observed in glycerol (section 2.3.1), may be attributed to methodological limitations or surface tension effects from the droplets. Thus we considered it in our fit model by adding an additional term k_{mat} to the Jeffrey's fluid affecting only the storage modulus at low frequencies:

$$G^*(\omega) = k_{mat} + i\omega\eta_0 + \frac{i\omega\eta_1}{1 + i\omega\tau_c} \tag{2.10}$$

The inset in Figure 2.7f illustrates a diagram of this mechanical model. The loss tangent plot further illustrates that condensates are fluid-like ($\tan\delta > 1$) at intermediate frequencies ($\sim$0.1-10Hz) and predominantly elastic ($\tan\delta < 1$) at higher frequencies.

To cross-validate our active microrheology results, we independently measured the viscoelastic moduli using VPT passive microrheology in samples with multiple beads inside the condensates (Fig. 2.8). Our results show an agreement in the loss modulus behavior across the analyzed frequency range, albeit with higher magnitudes. Unlike active measurements, passive measurements did not show a plateau in the storage modulus at low frequencies, suggesting a fluid-like behavior of the condensates across all frequencies below the crossover point. Increasing the acquisition frame rate extended the experimentally accessible frequency range, as shown in Figure 2.8b, but data was insufficient to validate the high-frequency condensate behavior observed using active microrheology.

Overall, active and passive microrheology measurements of rMfp-1 condensates reveal that coacervates triggered by the addition of chloride or sulfate exhibit a Jeffrey's fluid rheology across all tested conditions.

2.3.3 pH and salt tunes viscoelasticity of rMfp-1 coacervates

To assess the impact of pH variation on the viscoelasticity of rMfp-1 condensates, we plotted the loss and storage moduli for each condition. As a control, we first present the viscoelastic moduli for a protein solution of 100 mg/mL without any added salt, which does not show coacervation (Fig. 2.9a). The observed behavior of the aqueous solution resembles that of a pure viscous fluid measured with the same method (Fig. 2.6). Consequently, we fitted the data to the simple viscoelastic model previously used (Fig. 2.7c). There is no significant variation in the magnitude of the loss modulus across different pH conditions. However, in the case of the storage modulus, there appears to be a slight increase with increasing pH. The loss tangent plot indicates predominant liquid-like behavior of the solution at frequencies above approximately 1Hz.

Next, we compared the chloride condition (Fig. 2.9b). Here, the data reveals a notable increase in the magnitude of the viscoelastic moduli at the highest pH, whereas there is only

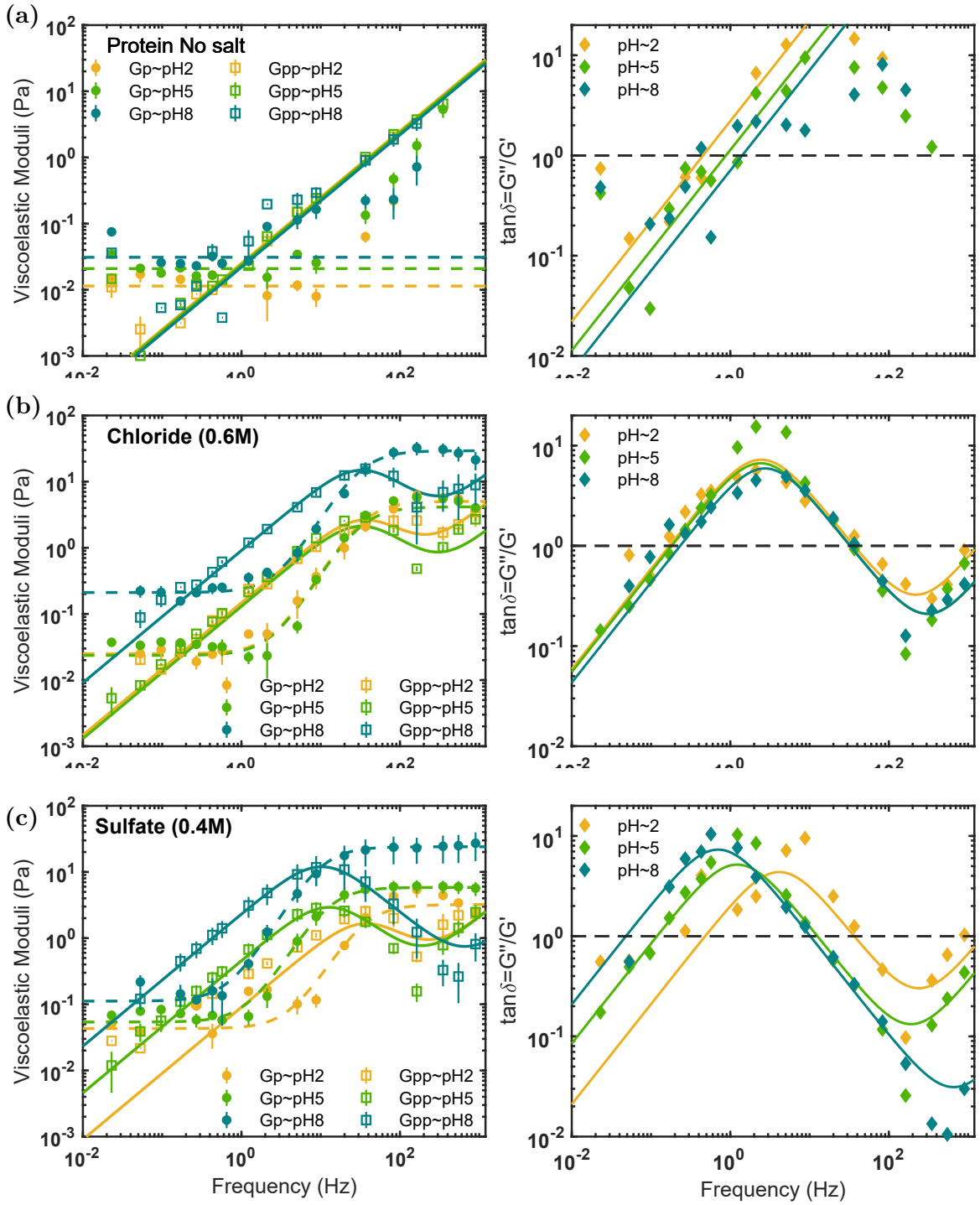

Figure 2.9: Viscoelastic moduli results for chloride and sulfate induced condensates. Moduli and loss tangent results at different pH values for (a) rMfp-1 solution with no salt added, fitted to the simple viscoelastic model (Fig.2.7c). (b) 0.6M chloride and (c) 0.4M sulfate conditions fitted to the modified Jeffrey's fluid model (mean and SEM from 1,000 bootstrap samples of n data sets at each condition. No salt: n=6 for pH∼2, n=4 for pH∼5, n= 5 for pH∼8; Chloride: n=4 for pH∼2, n=6 for pH∼5, n= 3 for pH∼8; Sulfate: n=5 for pH∼2, n=4 for pH∼5, n=3 for pH∼8)

a slight variation between the low and intermediate pH conditions. The loss tangent plot shows that while the magnitude of the moduli changes, the range of frequencies where the behavior shifts from liquid to solid remains highly similar.

Finally, in the sulfate condition (Fig. 2.9c), we observed an increase in the magnitude of both the loss and storage moduli with increasing pH. Unlike the chloride situation, the addition of sulfate also affects the frequency range of transition where viscous contribution dominates over the elastic, suggesting an impact on the timescales at which the coacervation process occurs.

As the coacervates exhibit a Jeffrey's fluid behavior, we derived the characteristic parameters by fitting the modified model (Eq. 2.10; Fig. 2.10a), which includes the elastic plateau at low frequencies, thereby minimizing fit errors. Table 2.2 presents the parameter values plotted in Figure 2.10b for each salt and pH condition. For chloride, the relaxation time τ_c shows no significant change from pH 2 to 5 but slightly increases at pH 8. In contrast, for sulfate, there is a substantial increase with pH. The corresponding corner frequency $f_c = 1/2\pi\tau_c$ exhibits an opposite trend, decreasing slightly for chloride at pH 8 and decreasing further as pH rises in the presence of sulfate. These data indicate a shift in the transition time (and frequency) from fluid-like to solid-like behavior. Specifically, sulfate induces elastic behavior over a wider time range ($t < \tau_c$) as pH increases, whereas chloride affects elastic behavior mostly at pH 8 and at shorter times compared to sulfate. Conversely, it suggests that fluid-like behavior ($t > \tau_c$) starts at larger times with sulfate and shorter times with chloride. An interesting observation is that the storage pH condition shows no significant difference between the two anions, suggesting that their effect in the fluid to solid like transition takes effect once the proteins are secreted.

The parameter η_1 can be interpreted as the long-term viscosity of the fluid-like state. We also included the viscosity term obtained for the protein without salt for comparison. In the absence of salt and hence coacervation, viscosity does not vary with pH and remains very low ($\sim$0.003 Pa).For the chloride case, there is a slight decrease in viscosity from pH 2

pH	Salt	τ_c (ms)	f_c (Hz)	η_1 (mPa·s)	η_0 (mPa·s)	E (Pa)	k_{mat} (Pa)
2	No salt	-	-	3.9 ± 0.3	-	-	0.009 ± 0.003
	Cl^-	4.9 ± 1.8	37 ± 14	23.5 ± 4.3	0.6 ± 0.2	5.1 ± 1.1	0.022 ± 0.006
	SO_4^{-2}	4.4 ± 0.5	37.1 ± 4.6	12.9 ± 1.3	0.3 ± 0.1	3.0 ± 0.2	0.038 ± 0.012
5	No salt	-	-	3.9 ± 0.2	-	-	0.019 ± 0.003
	Cl^-	4.4 ± 0.5	36.5 ± 4.2	17.7 ± 2.8	0.20 ± 0.03	4.0 ± 0.5	0.020 ± 0.009
	SO_4^{-2}	11.6 ± 2.2	14.3 ± 3.5	64.4 ± 23.9	0.3 ± 0.1	5.4 ± 1.4	0.052 ± 0.007
8	No salt	-	-	2.8 ± 1.1	-	-	0.034 ± 0.007
	Cl^-	6.5 ± 6.4	29.4 ± 5.9	140.7 ± 21.8	1.6 ± 1.1	26.4 ± 7.6	0.209 ± 0.036
	SO_4^{-2}	17.0 ± 5.6	9.9 ± 1.9	360.4 ± 127.6	0.09 ± 0.04	23.4 ± 10.8	0.091 ± 0.057

Table 2.2: Parameters from the modified Jeffrey's model for rMfp-1 condensates. Parameters (with Std Dev) fitted to the loss and storage modulus of rMfp-1 at different conditions of pH and salt.

to pH 5, followed by a significant increase (∼8-fold) at pH 8. Sulfate induces a consistent increase in viscosity with increasing pH, reaching significantly higher magnitudes compared to chloride under the same pH conditions (∼0.5-3 fold). These data suggest that sulfate combined with pH increase has a stronger effect on the electrostatic attraction in coacervate formation compared to chloride, where the effect is stronger only under seawater conditions and viscosity is lower than sulfate under the same pH condition.

The term η_0 describes a short-term viscosity that becomes relevant only at very high frequencies, where viscous contribution predominates again over elastic behavior. Fit values from the experimental frequency range analyzed show very low values for η_0 approximately 1-fold lower than the viscosity of the protein solution in the absence of coacervation. Additionally, there is no significant trend or difference between the two salt conditions with increasing pH.

The quantity E refers to the magnitude of the storage modulus where elastic behavior dominates over G" after the crossover frequency f_c. The variation between pH 2 and 5 slightly decreases for chloride and increases for sulfate. Moreover, at seawater pH, there is a significant increase (∼5-fold) for both chloride and sulfate, reaching similar magnitudes, suggesting that seawater conditions have a major effect in inducing higher stiffness under

rapid motion.

Finally, the term k_{mat} is plotted alongside values obtained for the protein without coacervation. The magnitude of this term is similar for chloride at pH 2 and 5; however, it increases 6-fold at pH 8. In the case of sulfate, the behavior follows a similar trend to that of protein alone, with a magnitude at least twice as large. As mentioned earlier, this parameter may arise as a limitation from our measurements in accurately determining the elastic modulus at low frequencies. The similarity in magnitude and trend between absence of salt and coacervate state under more acidic conditions (2 and 5) could hint that this parameter presence is method-related. Nonetheless, the significant change at the highest pH value may indicate an effect of the coacervate state on stiffness at low frequencies, potentially related to a surface tension contribution.

To summarize, our data reveals the strong influence of pH and salt content in the mechanical response of rMfp-1 coacervates, especially at seawater condition.

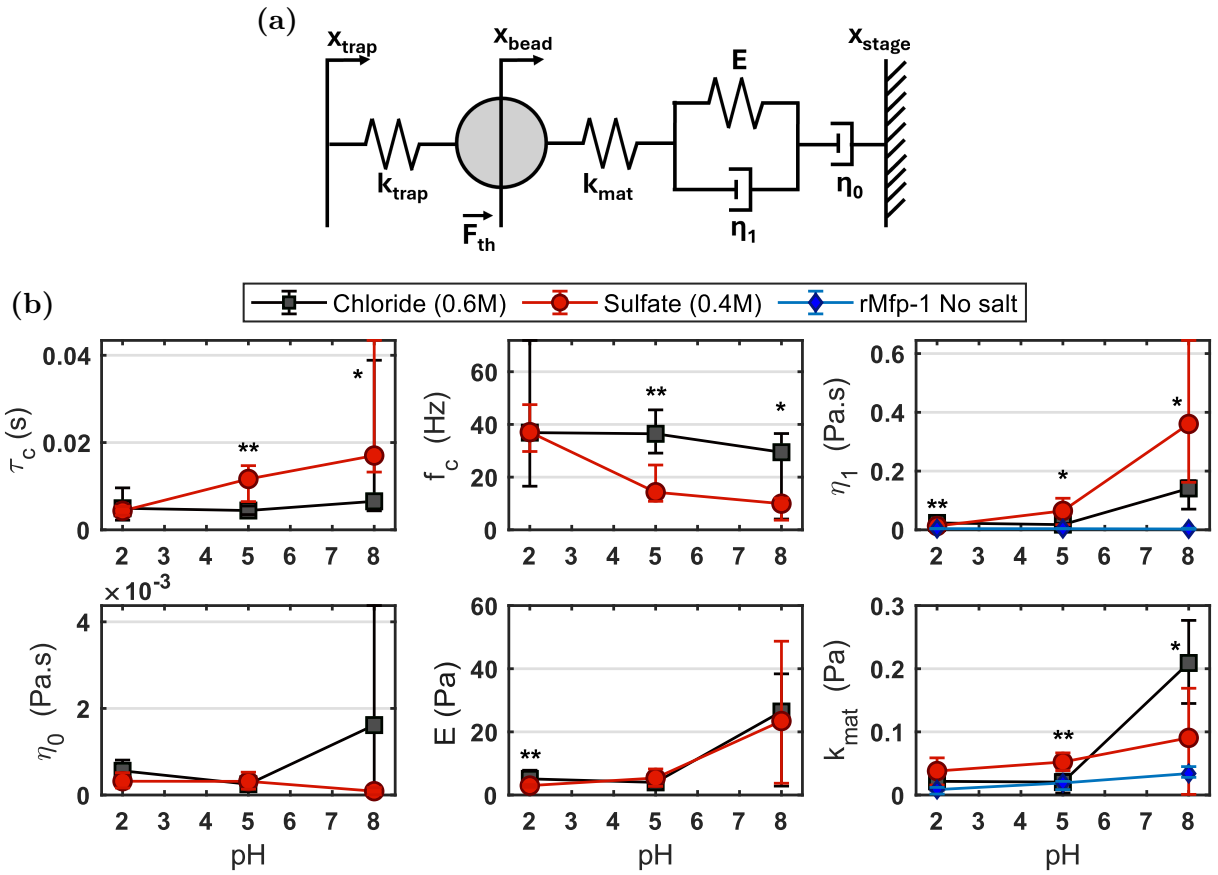

Figure 2.10: Parameters from the modified Jeffrey's model across different salt conditions for rMfp-1 condensates. (a) Schematic of the experimental diagram for an optically trapped bead (left bead's side) embedded within a material described by the modified Jeffrey's model (right side). The later was fit to the chloride and sulfate conditions to obtain the parameters shown. (b) Fit parameters in the presence of chloride, sulfate, and without salt. In the absence of salt there is no coacervation hence only a simple viscoelastic model with two parameters is fit (Fig.2.7c) (** indicates a p-value of $p < 0.01$ and * corresponds to $p < 0.05$ between the coacervate conditions at same pH).

Chapter 3

Microrheology of the cell cytoplasm

3.1 Cell mechanics

As the fundamental unit of life, cells are constantly exposed to mechanical forces such as shear, compressive, and extensional forces [76]. Hence, proper cellular function relies on their ability to control their response to mechanical stimuli. Moreover, cells are complex heterogeneous systems that behave in different forms depending on their environment, function, or life stage. To regulate their physiological activity, they sense mechanical cues and convert them into biochemical responses to provide adequate conditions for different processes to take place, such as cellular division, proliferation, migration, and adhesion [2].

The interior of a single cell is fluid-like, packed with organelles, macromolecules, and polymeric structures that define the cell's internal organization and shape [77]. However, the cytoskeleton, a complex network of polymeric filaments, determines the cell's mechanical behavior[2]. The cytoskeleton is a network consisting of three types of dynamic filaments: microtubules (MTs), actin, and intermediate filaments. These filaments change their organization in response to mechanical and biochemical signals, modifying the cell elasticity and viscosity according to their environmental needs [78]. Abnormalities in these mechanisms associate with the development of diseases. For example, studies have shown that malaria disrupts the cytoskeletal reorganization of red blood cells modifying their adhesive properties and making them stiffer, compromising their function and enabling the disease to evolve [79]. In cancerous cells, alteration of the cytoskeleton results in a change

of cell stiffness, which is believed to have an essential contribution to metastasis as it provides the cell with the ability to squeeze and disseminate to other tissues [80]. Understanding the individual mechanics and dynamics of these mechanisms offers not only a starting point towards a general model of mechanical cell regulation, but also opens the possibility to potentially use them as a tool in therapeutics again disorders triggered by cytoskeletal misregulation.

3.1.1 Microtubules

The first studies to uncover how the cytoskeleton regulates cell mechanics focused on actin filaments because of their roles in cell movement, shape and architecture [81]. However, in the last decade, increasing research has highlighted microtubules importance as cell mechanical regulators. For instance, it has been shown that microtubules play a key role in the mechanics of the cardiac muscle [82], and in the mechano-transduction process necessary to perform migration or adhesion [83].

Microtubules are the largest and stiffest cytoskeletal constituents, formed by α-tubulin and β-tubulin heterodimers that assemble into hollow tubes of around 25nm in diameter [84]. Microtubules are highly dynamic, as they can switch from growing to shrinking, a process called *dynamic instability*. Microtubule dynamics allow rapid cytoskeletal reorganization and force generation, particularly important during cell division [85]. In addition, the different properties and functions that microtubules display, such as their dynamics and mechanics, are tuned by a combination of their post-translational modifications (PTMs) and the tubulin isoforms they are build from [86]. Among the most studied PTMs are tyrosination, glutamylation, polyglutamylation, and acetylation.

3.1.2 Motivation and objectives

Despite their dynamic nature, some microtubules can remain stable and persist for several hours in the cell cytoplasm, a necessary characteristic to maintain tracks for intracellular transport [87]. In recent years, research has found that acetylation directly protects stable microtubules from mechanical breakage and confers them with a higher flexibility, thus explaining microtubule stability [87, 88]. Therefore, we hypothesize that microtubule acetylation could be an important regulator in the context of cell mechanics.

Tubulin acetylation modifies the lysine 40 (K40) site of α-tubulin, located on the inner side of the microtubules (the lumen); in mammals, acetylation is majorly mediated by an enzyme named α-tubulin acetyltransferase, while it is removed by the histone deacetylase 6 (HDAC6), and in special conditions by Sirtuin 2 (SIRT2) [89].

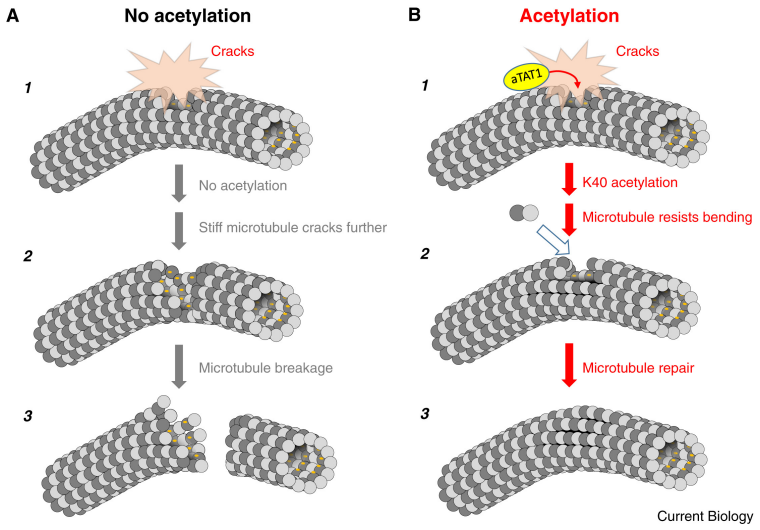

Figure 3.1: Tubulin acetylation increases microtubules resistance to stress. Upon bending forces, microtubules experiment a mechanical stress that can damage their lattice and produce cracks. (a) Damage can spread and lead to the microtubule breakage and complete depolymerization. (b) However, it is proposed that α-tat1 uses these cracks to access the microtubule lumen and acetylate the K40 site in the α-tubulin. This modification increases the microtubule flexibility protecting it from further breakage and providing it more time to self repair, thus keeping it stable. (Reprinted from [90], Copyright ©2017, with permission from Elsevier; permission conveyed through Copyright Clearance Center, Inc.)

Because microtubules interact with the actin filaments by different mechanisms, such as crosslinking or anchoring by actin networks[91], we expect that changes in the microtubules mechanical properties will affect the entire cytoskeletal network, thus leading to changes in the cell's mechanical response.

Currently, there is a consensus regarding that cytoskeleton mechanical properties are described using a theory based on the semiflexible polymer network model [9]. In consequence, optical tweezers microrheology is particularly useful because it access to a wide range of different timescales, providing information about the intracellular network dynamics, such as characteristic timescales, in contrast to techniques like atomic force microscopy (AFM) and magnetic twisting cytometry, that apply deformation only at the cell surface and across a narrow frequency range [25]. Hence, to investigate the role of microtubule acetylation as a possible mechanical regulator of the cell mechanical properties, we will apply a previously developed optical tweezers-based active microrheology technique to measure the viscoelastic moduli of the cell cytoplasm. This method analyzes only the response to specific frequencies, hence is insensitive to non-equilibrium active cellular processes like motor protein-based transport and cytoskeletal dynamics [8, 72]. In addition, it accounts for cell heterogeneity by performing the trap calibration *in situ*, thus providing more accurate measurements [8]. In this manner, we sought to identify the intracellular mechanical changes produced in the cytoeskeletal network due to microtubule acetylation by comparing the complex modulus of wildtype cells against hyper-acetylate induced cells.

Finally, previous studies have shown microtubule acetylation alterations to be associated with neurological disorders and some cancer types [92], therefore knowledge of how acetylation affects the cell mechanical structure will provide a deeper insight into those diseases and potentially propose new treatment strategies to target them. Besides, elucidating the role of microtubules in cell mechanics will provide one more step towards establishing a more complete model to describe the general mechanisms that cells use to

regulate their mechanical properties.

3.2 Methodology

3.2.1 Plasmid

We used an α-tat core plasmid construct tagged with YPet yellow fluorescent protein, a gift from Kristen Verhey (University of Michigan). The plasmid contains the catalytic core of alpha tubulin acetyl transferase (also known as MEC17) to induce hyper-acetylation in mammalian cells. We obtained the plasmid from a glycerol stock with DH5alpha bacteria resistant to ampicillin using a maxi-prep procedure(Qiagen, Hilden, Germany) according to manufacturer's instructions.

3.2.2 Cell culture

U-2 OS cells (American Type Culture Collection, Manassas, VA) were cultured in T-25 cell culture flasks (Sarstedt) for maintenance. Cells were grown in culture media containing DMEM basal media (Gibco) supplemented with 1% (v/v) glutamax (Gibco) and 10% (v/v) fetal bovine serum (Gibco). Cells were passaged at 80% confluency using 0.25% trypsin-EDTA (Gibco) and PBS (Wisent, St-Jean Baptiste, QC, Canada), and they were terminated by P20. Previous to cell passaging, glass coverslips (22×22mm, Fisher Scientific) were sterilized with 70% ethanol and placed at the bottom of 6-well plate (Sarstedt) slots. Then, cells were seeded onto the coverslips and incubated at 37°C with 5% CO_2 for 24-36 hours to yield an appropriate cell density prior to transient transfection. When cells were ∼80% confluent, they were transiently transfected with $\sim 0.3\mu g$ of α-tat plasmid prepared in OPTIMEM Reduced Serum (Gibco), using Lipofectamine LTX with Plus-Reagent (Invitrogen, Thermo Fisher Scientific), according to the manufacturer's instructions. Cells were incubated with transfection solution for four hours before

replacement with fresh DMEM media. Afterwards the cells were left overnight(∼12h) in the incubator at 37degC before experiments.

3.2.3 Sample preparation

We used 500nm red[580/605] FluoSpheres^{TM} Carboxylate-Modified Microspheres (F8813, Invitrogen), previously PEG-coated following protocol from section 2.2.2, to avoid spectral crosstalk with the α-tat-YPet. Prior to the experiment, the beads were washed and resuspended in hypertonic media ($\sim 10^7$ beads/mL in 10% PEG 35000, 0.25 M sucrose in supplemented DMEM media). Culture media was removed from the 6-well plates and $\sim 50\mu L$ hypertonic media was added to the coverslips. The cells were incubated in the hypertonic media for 1h to allow bead uptake via phagocytosis, after which they were washed and hypotonic media (2:3 water:complete media) was added followed by an incubation of no more than 3 minutes, to burst the phagosome membranes around the beads. Then, regular complete media was added to the cells and they were left in the incubator for one hour to recover from the shock. A chamber was made by gluing two double-sided tape pieces to a glass slide (dimensions: 25×75mm, thickness: 1 mm, Globe Scientific, 1331) at the same distance to create a channel. Then a line of vacuum grease (Dow Corning High Vacuum Grease) was added to the channel edges, and a the coverslip with the cells was carefully put on top and pressed to close the chamber. Next, imaging media (Leibovitz) was flowed through the chamber and the open sides were sealed using vacuum grease to prevent sample evaporation. A custom-built environmental chamber with a heating system (World Precision Instruments) allowed to kept the cells at 37 °C during the optical trapping experiments.

3.2.4 Optical tweezers-based active microrheology in cells

Active microrheology was performed on the same custom-built optical tweezers system previously described in section 2.2.6. Heater was turned on 30 minutes prior to measurements ensuring the environment temperature being 37° and the objective correction collar was adjusted accordingly. Cells were visualized using the brightfield camera of the microscope and presence of the plasmid was verified by assessing cells fluorescence illuminated with a 488nm diode laser at 5 mW (Coherent OBIS Laser box), using the TIRF system of the microscope. As there are several of small vesicles inside the cell that could be confused with a bead, we verified the bead presence by fluorescence under the 571nm laser at 1 mW. Once a single diffusive bead was localized inside the bead's cytoplasm, at a middle distance from the cell's edge and its nucleus, the optical trap is turned on and the bead is trapped. Next a multicomponent (∼22 frequencies) excitation input wave was applied with a frequency range covering from ∼0.02 Hz to 1000 Hz with corresponding amplitudes ranging from ∼50 nm to ∼1 nm. The frequencies of oscillation were chosen at prime numbers to avoid subharmonics generation. The amplitudes were adjusted empirically to be small enough to remain in the linear response regime of the system and at the same time to provide a coherent signal. Measurements of the bead position signal and the laser input were recorded for 275 seconds at a sampling rate of 20 kHz. Where possible, a step excitation at 1Hz was measured after the multiharmonic wave to be used in the estimation the QPD sensitivity.

3.2.5 Optical trap calibration for cells active microrheology

The optical trap was calibrated following the previously developed method [8, 72, 73]. The calibration is analogous to the methodology provided in section 2.2.7, but using a different viscoelastic model to account for the cell environment. The cell simplified calibration model, propose to account for the frequency dependent stiffness of the cytoplasm by introducing

a time dependency in the elastic part of the model [8, 72]. Hence, the stiffness parameter of the system is written as the sum of a constant stiffness plus a time dependent term: $k_{cyt}(t) = k_{cyt0} + k_{cyt1}t^{-(\alpha-1)}$; which adds two parameters α and k_{cyt1} for fitting. The equation of motion to describe the trap system in the cell using this model is,

$$m(\ddot{x}_{trap}) + \gamma_{mat}(\dot{x}_{trap}) + (k_{cyt0} + k_{cyt1}t^{-(\alpha-1)})(x_{trap}) = \\ - m(\Delta\ddot{x}) - \gamma_{mat}(\Delta\dot{x}) - \kappa(\Delta x) - (k_{cyt0} + k_{cyt1}t^{-(\alpha-1)})(\Delta x) + f_{thermal} \quad (3.1)$$

where as before $\Delta x(t) = x_{bead}(t) - x_{trap}(t)$, m is the bead mass, γ_{mat} is the friction coefficient of the medium (proportional to the viscous part of the medium), $k_{cyt}(t) = k_{cyt0} + k_{cyt1}t^{-(\alpha-1)}$ represent the frequency dependent stiffness of the cytoplasm (proportional to the elastic contribution), κ is the trap stiffness, and $f_{thermal}$ represents the forces due to thermal fluctuations, with $(\langle f_{thermal}(t)\rangle = 0)$ and $(\langle f_{thermal}(t) f_{thermal}(t')\rangle = 2k_B T\gamma_{mat}\delta(t-t'))$.

After taking the Laplace transform of Eq 3.1, ignoring inertial contributions, the final calibration equations to fit the experimental transfer function and power spectrum are:

$$H(\omega) = \frac{V_{pd}(\omega)}{X_{trap}(\omega)} = \frac{1}{\beta_{pd}} \times \frac{\gamma_{cyt} j\omega + k_{cyt0} + \frac{k_{cyt1} j\omega^{\alpha}}{\Gamma(\alpha)}}{\kappa + \gamma_{cyt} j\omega + k_{cyt0} + \frac{k_{cyt1} j\omega^{\alpha}}{\Gamma(\alpha)}} \quad (3.2)$$

$$\left\langle V_{pd}(\omega)^2 \right\rangle = \frac{1}{\beta_{pd}^2} \times \frac{2k_B T(\gamma_{cyt} j\omega + \frac{k_{cyt1} j\omega^{\alpha}}{\Gamma(\alpha)})}{\omega|\kappa + \gamma_{cyt} j\omega + k_{cyt0} + \frac{k_{cyt1} j\omega^{\alpha}}{\Gamma(\alpha)}|^2} \quad (3.3)$$

Additionally, the material and optical properties of cells are not homogeneous, the photodiode constant β_{pd} and the trap stiffness k_{trap} are expected to vary from cell to cell. Due to the highly viscoelastic environment, the bead does not instantaneously respond to the trap motion, and the instantaneous increase in voltage recorded by the QPD under a step excitation can be related to the bead displacement to estimate the β_{pd} value as described in [73]. Where the square measurement was available, β_{pd} was estimated using this method to enter as an initial guess in the fitting calibration algorithm.

Once calibration is done, the viscoelastic moduli is obtain in the same manner described in section 2.2.8, using equations 2.7, 1.41 and 2.8.

The mean of the storage and loss modulus for the two conditions was computed from 1000 bootstrap samples drawn from each data set with their corresponding 95% confidence intervals. Fittings to the mechanical model where done using the *lsqcurvefit* Matlab function.

3.3 Results

3.3.1 In situ optical trap calibration and α-tat1 expression

To better understand the impact of microtubule acetylation in the overall mechanical response of the cell cytoplasm, we characterized the viscoelasticity of cells under hyperacetylated conditions by applying an optical tweezers microrheology approach, where 500nm PEGylated beads were internalized by the cell to be used as probes, and a multiharmonic excitation input was applied to the trap position (Fig. 3.2a,3.2b). To study the acetylation effect, we transiently transfected U2-OS cells with a plasmid containing the catalytic core of α-tat1, with the objective of hyperacetylating the microtubules. Because the construct was tagged with YPet yellow fluorescent protein, we assessed the expression of α-tat1 by fluorescence microscopy as shown in Fig.3.2c. The α-tat1 was uniformly distributed across the cell cytoplasm. Finding a transfected cell with a diffusive bead in it was challenging, as we performed a chemical lipid-based transient transfection method that considerably reduced the amount of viable cells in our sample; then followed by an osmotic shock to induce bead internalization, which further depleted the available cells to measure. In practice, for an appropriate control of the experiment, the construct expression level is normalized to the background of each cell to select cells with similar conditions; however, due to the limited amount of transfected cells with beads per sample, we considered all the cells showing a visible intensity in contrast to the background, regardless of their intensity

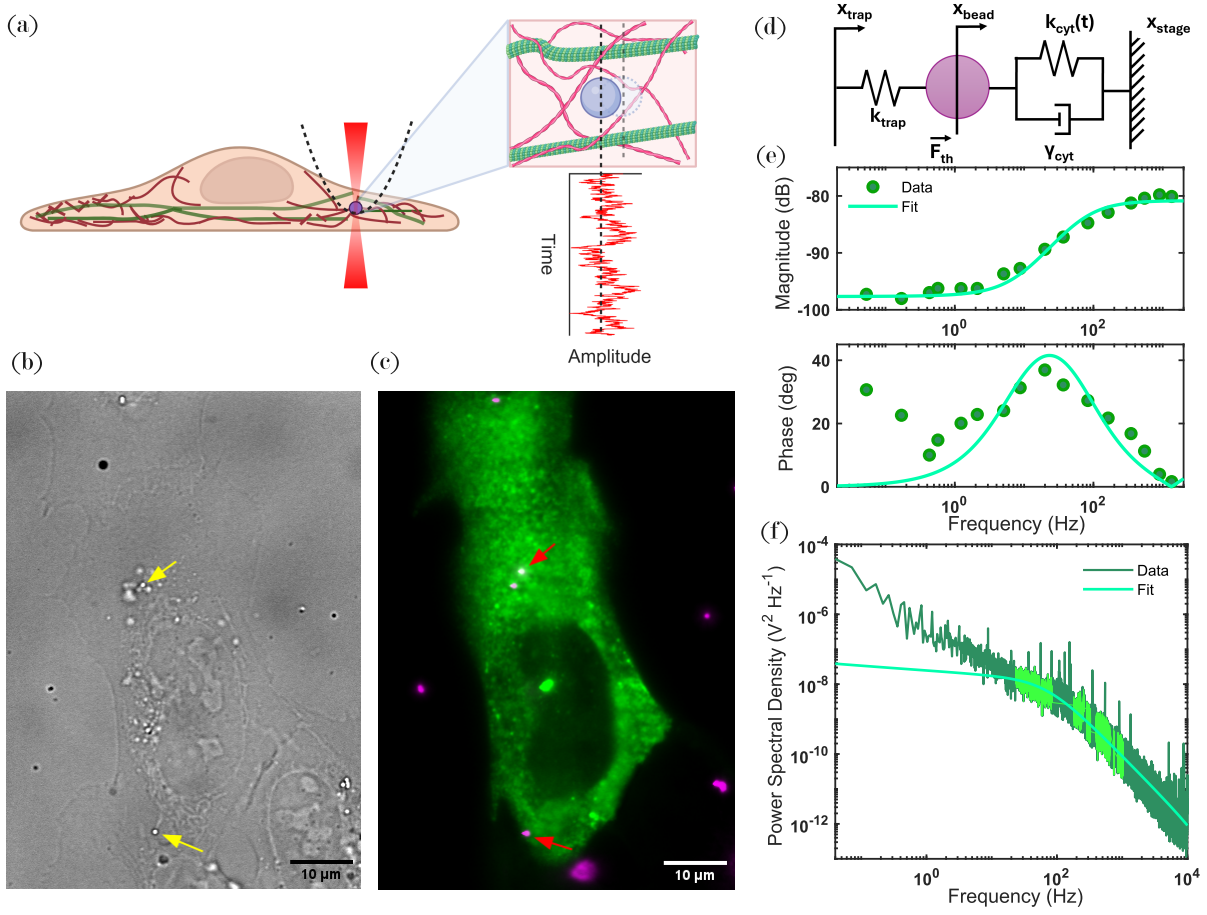

Figure 3.2: Active microrheology in cells. (a) A bead is internalized in a cell and optically trapped to apply a multi component oscillatory deformation. (b) Brightfield image of a U2-OS cell with internalized beads shown by arrows. (c) Fluorescent image of the same cell showing expression of α-tat1 in green and fluorescent beads in magenta. (d) Simple viscoelastic model fitted for calibration; the term $k_{cyt}(t) = k_{cyt0} + k_{cyt1}t^{-(\alpha-1)}$ accounts for the frequency dependent stiffness of the cytoplasm. (e) Magnitude and phase of the transfer response function fitted to the simple viscoelastic model to obtain the trap stiffness k_{trap} (pN/nm) and the photodiode constant β_{pd}(nm/V). (f) Power spectrum of the fluctuations of the bead (dark green). Only high frequencies representing the thermal fluctuations (light green) are simultaneously fit to the passive part of the model as they are not affected by the active process occurring in the cell. (Figure 3.2a created with BioRender.com)

level. Hence, the results here presented are still considered preliminary because it was necessary to average few measurements from each of various samples with different transfection levels, which can lead to a significant variability in the final results. For the cells meeting all the conditions, a freely diffusing bead in the cytoplasm was optically

trapped and its response to a multiharmonic excitation was measured. This measurements were used to calibrate the optical trap by simultaneously fitting the viscoelastic model shown in Fig.3.2d to the transfer response magnitude (Fig.3.2e) and the high frequencies of the power spectrum (Fig.3.2f) leading to average calibration values of $\beta_{pd} = 14533$ nm/V and $k_{trap} = 0.01$ pN/nm. Additionally, to be used as a control, measurements were done in cells without performing the transient transfection step, and in cells from transfected samples not showing fluorescence of the plasmid.

3.3.2 Intracellular viscoelasticity under hyperacetylation

We successfully obtained the viscoelastic moduli for three different conditions: wildtype U2-OS cells, cells from transfected samples not showing expression of α-tat1, and cells showing expression of α-tat1 (Fig. 3.3). Overall, the storage modulus dominates across all the frequencies measured, however, at frequencies below 1Hz, the loss modulus reaches a maximum and minimum accompanied by a decrease in elasticity, an indication of the presence of transient crosslinks [93]. In agreement with previous work [8], the viscoelastic moduli was described well by fitting a model representing the presence of a dominant crosslinker in a semiflexible polymer network, where the frequency of the loss modulus local maximum is determined by the crosslinker characteristic timescale as $f_r = k_{off}/2\pi$ [93]. The corresponding equations for the storage and loss modulus of that model are,

$$G'(f) = G_0 - a \cdot \frac{N k_{off}}{\left(\frac{k_{off}}{2\pi}\right)^2 + f^2} + b \cdot \left(\frac{f}{f_0}\right)^{\beta} \tag{3.4}$$

$$G''(f) = c \cdot \frac{N f}{\left(\frac{k_{off}}{2\pi}\right)^2 + f^2} + d \cdot \left(\frac{f}{f_0}\right)^{\beta} \tag{3.5}$$

where the term G_0 in the storage modulus represents the value of the elastic plateau at lower frequencies, which decreases due to crosslink unbiding, with N the density of intact crosslinks. The last term including the factor f_0 represents the fluctuations of single filaments in the

semiflexible network. The terms a and c are related to the energy dissipated by crosslink unbinding, whereas b and d scale with the density of filaments in the network [93].

We first compared the viscoelastic moduli of cells no transfected against cells showing expression of α-tat1 (Fig. 3.3a). We observed that the shape of the moduli is similar in both cases, with a slight decrease in the magnitude for the hyperacetylated case. The best fit to the averaged moduli yield an estimate of $k_{offWT} = 0.26s^{-1}$ for wildtype (WT) cells, compared with a value of $k_{offHA+} = 0.46s^{-1}$ for the hyperacetylated (HA+) case, corresponding to relaxation frequencies of $f_{rWT} = 0.04Hz$ and $f_{rHA+} = 0.07Hz$ respectively. The exponent of last term in Eq. 3.5 was $\beta_{WT} = 0.40$ for the wildtype cells versus $\beta_{HA+} = 0.41$ for the hyperacetylated cells. Given the high variability across the samples, the difference in these parameters could not be asserted as significant.

Further, to reduce the variability of experimental conditions, we analyzed viscoelastic measurements from cells not showing any α-tat1 expression (HA-) in the same sample of cells that were transfected. Interestingly, the viscoelastic response of the cells not expressing the plasmid versus cells showing fluorescence is almost the same (Fig. 3.3b). The estimated parameters from the fitting are $k_{offHA-} = 0.36s^{-1}$ and $f_{rHA-} = 0.06Hz$ for cells showing no expression against $k_{offHA+} = 0.46s^{-1}$ and $f_{rHA+} = 0.07Hz$ of the hyperacetylated case. The exponent β_{HA-} matched the value $\beta_{HA+} = 0.41$.

Finally, the loss tangent plots for both cases (Figs. 3.3c and 3.3d) show better the dominant elastic behavior of the cell across the frequency range studied, as well as the tendency of the cell cytoplasm to increase its fluid-like behavior at frequencies below 1Hz.

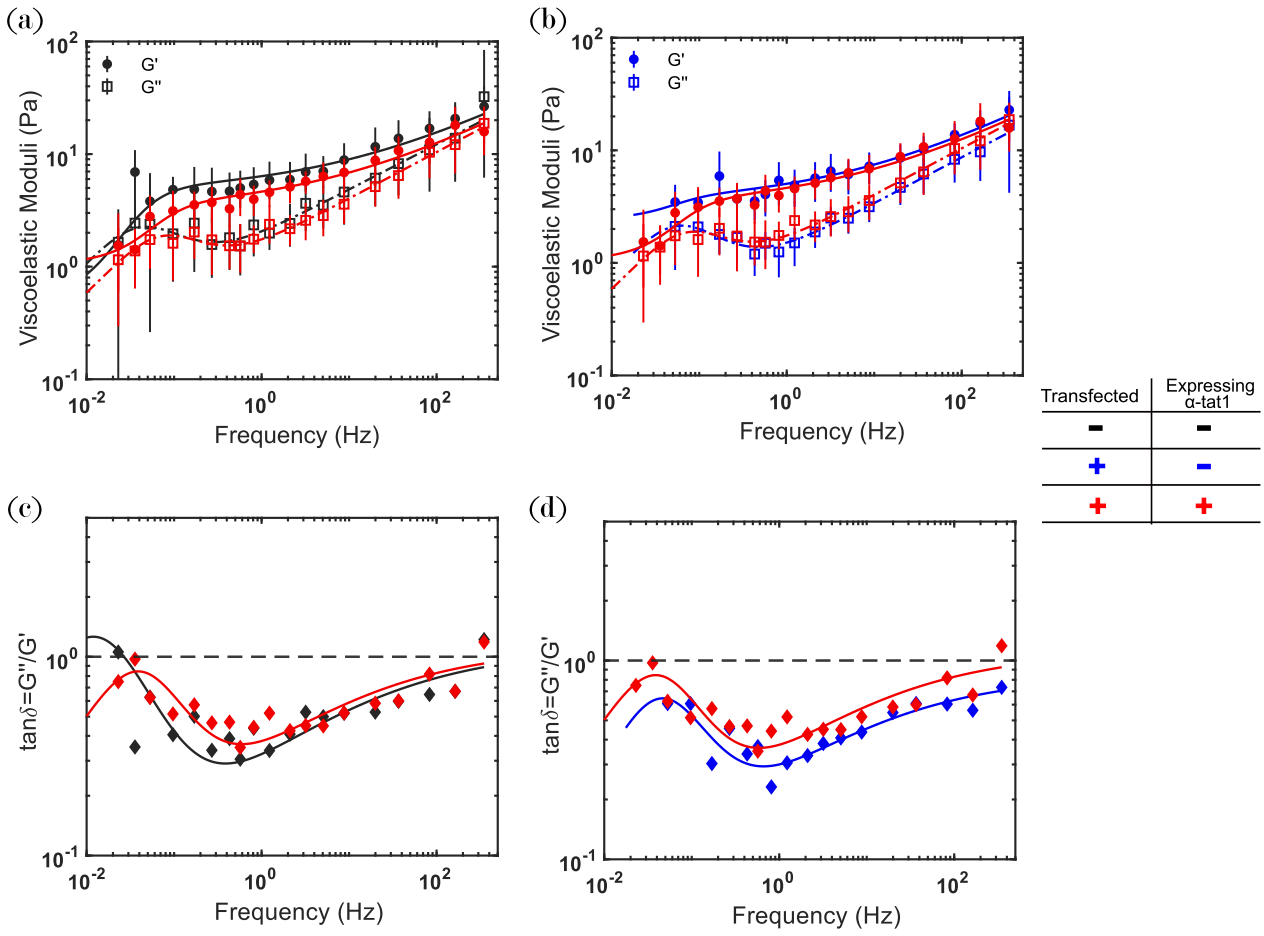

Figure 3.3: Viscoelastic moduli of cells. (a) Frequency dependent moduli and (c) losstangent of no transfected cells vs cells showing expression of α-tat1. (b) Viscoelastic moduli and (d) losstangent of cell sample treated with transfection comparing cells not showing expression vs cells showing expression of α-tat1 (mean and 95 confidence intervals from 1,000 bootstrap samples of n data sets at each condition. No transfected: n=13; Transfected sample showing no expression: n=11; Cells showing expression of α-tat1: n=24)

Chapter 4

Discussion

Optical tweezers-based microrheology is uniquely suited to characterizing the viscoelastic properties of intracellular structures like the cytoskeleton or membraneless organelles formed by liquid-liquid phase separation, being an important tool in their rheological characterization. In both cases they are composed by a biopolymeric network with transient crosslinks between their constituents, protein molecules in the case of LLPS, and semiflexible polymer filaments in the case of the cytoskeleton. The rate at which those crosslinks bind and unbind determine the mechanical response of the material when a deformation is applied, producing a rich viscoelastic behavior. The microrheology technique used here allows us to measure viscoelasticity across a wide range of different timescales simultaneously using an embedded probe inside the sample, thus providing information about the dynamics of the protein networks. This technique was originally developed to study the cell cytoplasm, thus we choose U2OS cells as one of the samples of study to illustrate the methodology when working with a sample *in vivo*. On the other hand, we adapted the technique to study the mechanical response of a type of biomolecular condensates formed extracellularly, as its use has focused mostly to study intracellular proteins. The sample of choice was a mussel foot protein, a protein of great interest in the design of biomaterials, and the experiments were performed *in vitro*. Additionally, I applied video particle tracking passive microrheology to compare the information obtained by active microrheology in the experiment *in vitro*. Furthermore, in each sample, we sought to investigate relevant mechanisms believed to affect their mechanical response and internal

network rearrangement.

In the sample *in vitro*, we investigated the combined role of pH with sulfate and chloride ions, as an important chemical stimuli to drive phase separation, and potentially the assembly of polymers, of recombinant mussel foot protein-1 (rMfp-1) condensates. In addition of measuring the viscoelastic moduli using the active microrheology optical tweezers approach, we obtained correlated data at low frequencies using video particle tracking microrheology. We found that overall, the rMfp-1 condensates triggered by the addition of chloride or sulfate exhibited a behavior well described by a Jeffrey's fluid model. Apart from this, we observed an increase in viscosity with rising pH for both anions, where sulfate induced condensates showed a higher viscosity, and a slower liquid to solid transition than condensates formed with sodium chloride.

In the sample *in vivo*, we aimed to address the role of microtubule acetylation in the cell's mechanical response by measuring and comparing the viscoelastic moduli in wild-type cells against cells transfected with a plasmid to induce microtubule hyperacetylation. However, as several procedures on the cells were required in preparation for the measurements, obtaining enough viable cells meeting the optimal experimental conditions was challenging. This resulted in a limited set of measurements with different expression levels of the enzyme driving acetylation, making it difficult to draw strong conclusions. Nevertheless, we analyzed the measurements at both conditions, finding a slight decrease in the magnitude of the viscoleastic moduli when samples were transfected, accompanied by a small shift in the relaxation frequency in the dynamic response towards a more fluid-like state. Additionally, cells not overexpressing the α-tat1 enzyme show even a smaller change in relaxation while presenting a stronger elastic behavior compared to cells expressing the enzyme. Hence, although our data set was too small to obtain a reliable statistical assessment of the observed differences, our measurements indicate that flexibility induced by microtubule acetylation is reflected in the overall cell mechanics.

In the following sections, I will discuss the implications and future work for each study.

4.1 Microrheology of rMfp-1 condensates

4.1.1 Discussion

We measured the viscoelastic moduli of rMfp-1 condensates triggered by the addition of sodium chloride or sodium sulfate at different pH conditions. We found that rMfp-1 condensates behaved like a Jeffrey's fluid across the experimental frequency range studied. Further, we compared optical tweezers measurements for low frequencies with video particle tracking microrheology and observe differences in the apparent elastic response dominating the low frequency range in measurements acquired using the active technique. Additionally, we found that chloride induced condensates exhibited a prominent increase of viscosity at pH 8 with no significant impact in the relaxation characteristic time by pH variation. In contrast, sulfate induces a consistent rising of viscosity by augmenting the pH, reaching higher values than chloride condensates. Moreover, the presence of sulfate results in increasing relaxation times τ_c when combined with an increase in pH.

In this study, we used an optical tweezers microrheology technique to characterize the rheological properties of a mussel foot protein condensate system for the first time, to our knowledge. Thus, we will first compare our measurements with previous characterizations available in the literature to assess the consistency of the data obtained using optical tweezers-based microrheology. As mentioned earlier, several Mfps have been mechanically characterized using Surface Force Apparatus (SFA). For instance, a previous work of the mechanical properties of rMfp-1 coacervates triggered by NaCl at acidic conditions (pH $\sim$ 3) revealed very low interfacial tension with shear-thinning viscous behavior [60]. Shear thinning has been suggested to facilitate flow through the narrow ducts during secretion [10]. It consist of a decrease in the viscosity under a load as shear rate increases, which is expected for materials that feature terminal viscous behaviors [94], such as the Jeffrey's fluid. Moreover, showing rMfp-1 condensates behaving fluid-like at low and intermediate

frequencies combined with the known low interfacial tension, concur to explain how the Mfp-1 spreads over the core to form the cuticle coating. Hence, our results describing the behavior of rMfp-1 condensates as a Jeffrey's fluid agree with the SFA measurements.

In addition, during a thiol characterization study [95], the viscosity of rMfp-1 condensates at 0.7M NaCl and pH 5.5 was measured to be 50 mPa·s. From our results, the long-term viscosity can be compared to the dominant viscous parameter from the Jeffrey's model η_1, that at pH ~ 2 was 23 mPa·s and 18 mPa·s for pH 5. Considering that the active method consistently gave lower magnitudes during calibration with glycerol solutions, apart from the experimental variability, our results are comparable at similar conditions, which confirms the viability of our optical tweezers-based microrheology technique to obtain physically meaningful information about the rMfp-1 condensates.

Among the advantages of using this active microrheology approach is its capability to expand the current knowledge about the effect of pH in NaCl-triggered rMfp-1 condensates by studying their dynamic viscoelasticity across a frequency range compatible with the network characteristic relaxation time τ_c. The transient network models for associative polymers suggest that τ_c relates with the kinetics of macromolecular transient association and dissociation[18, 75]. Given that the NaCl triggered condensates had very similar values for this parameter, we propose that chloride has no significant effect in the network reconfiguration times, maintaining a dominating fluid-like behavior throughout the same timescales independently of pH condition. On the other hand, the viscous term η_1 can be explain by two scenarios: an increase in the degree of structural order (or compactness)[96]; or an increase in the strength of macromolecular interactions[75]. As the network configuration time does not change significantly, this suggests that the strength of interactions does not increase; if it were the case, the strengthened network would take larger times to break the stronger bonds. Then, the notable increase in the viscosity of condensates from acidic (pH 2 and 5) to seawater conditions (pH 8) could be consequence of an increase in macromolecular packing as pH increases. This scenario is supported by

previous findings showing a cohesion enhancement with increasing NaCl content, as well as the reduction of volume fraction of the coacervate phase upon pH increase from ~ 2 to ~ 8 [60]. Together, our results regarding NaCl induced rMfp-1 condensates suggest that the exposure to seawater compacts the macromolecular structure of the full network without affecting its reconfiguration time significantly.

Following to discuss the sulfate triggered rMfp-1 condensates, we found that, although previous works have shown coacervation of some plaque proteins triggered by sulfate [97, 98, 99], there is not literature regarding sulfate inducing Mfp-1 coacervates. In this regard, our study demonstrates that rMfp-1 coacervation can also be triggered by the addition of sulfate anions, which is not surprising given that cuticle vesicles contain sulfur [58]. By characterizing the rheological properties of sulfate triggered rMfp-1 coacervates under different pH conditions, we showed that condensates are viscoelastic, with the fluid like behavior dominating at low frequencies and intermediate frequencies. However, unlike the chloride induced condensates, we observed a shift to the left in the crossover frequency as pH rises (Fig. 2.9c). This could mean that as pH increases, the interactions of the sulfate anions with rMfp-1 molecules induce a change in the network reconfiguration times, probably by the formation of strong electrostatic interactions. At pH 2, the value of τ_c is 4.9ms, continuing to 11.6ms at pH 5 and reaching 17ms for seawater pH 8. This suggests the formation of a strengthened network at seawater conditions, which is seconded by the increase of η_1, from 12.9 mPa·s at pH 2, to 64.4 mPa·s for pH 5, rising up to 360.4 mPa·s at pH 8. These results reflect that, compared to chloride, presence of sulfate anions provide a more controlled mechanism to tune the rheological properties of rMfp-1 coacervates towards a more viscous solution, possibly facilitating the transition to solid in its native state once they are exposed to seawater.

Indeed, the presence of sulfate inside plaque vesicles has been proposed to stabilize the internal condensed phase at acidic pH by enabling phase separation and creating a reducing environment against oxidation [50]. Our results highlight the ability of sulfate to trigger

rMfp-1 condensation at low pH, and showing a more fluid behavior compared to that seen at pH 8, support this scenario. Nevertheless, the structure of the cuticle vesicles differs from the plaque vesicles in that the former shows a two-layer structure composed of immiscible condensed phases. The external layer named the proto-matrix, coalesce with other vesicles and shows sulfur-rich components along with cysteine rich-proteins (Mfp-16, Mfp-19); the inner layer, called proto-granule, is enriched with Mfp-1 and DOPA with a minor presence of sulfate [58]. Although more detailed studies of the phases in both layers is required, our results suggest that the colocalization of Mfp-1 and sulfate in the proto-granule can contribute to the condensed phase observed.

Altogether, our results combined suggest that the presence of sulfate offers a higher degree of control in the rMfp-1 coacervates viscoelasticity, from the storage state towards solidification, by strengthening electrostatic interactions in synergy with pH changes. In contrast the presence of chloride enhances the coacervate cohesion mostly when exposed to seawater pH condition. These observations indicate that different salts could play different roles during the byssus assembly at different stages. For instance, sulfate could participate in stabilizing the precursor proteins at the storage and secretion phase, to then stimulate the solidification process in cooperation with chloride once the coacervate is exposed to seawater. Additionally, the elastic predominant behavior in both condensate conditions at higher frequencies, which is $\sim$ 5-fold greater at pH 8 (Table 2.2), may serve as a material reinforcement to resist rapid wave impacts.

4.1.2 Future work

We have demonstrated that two specific salt types, sodium chloride and sodium sulfate, in synergy with pH variation, greatly affect the rheological properties of Mfp-1 coacervates. Although is hard to predict which salt participates in the formation of condensates at each different assembly stages, the uniform presence of nitrogen in the cuticle vesicles [58] and a

previous report [98] indicating $NaNO_3$ induced coacervate formation of other Mfp (rfp-3F), suggests that nitrate could also interact with Mfp-1 to some degree, which, nevertheless, should be further confirmed.

Also it is of relevance to consider that our experiments were done using a recombinant form of the rMfp-1, which lacks DOPA and a non-repetitive domain present at the protein N-terminus [58]. Consequently, the behavior observed does not reflect completely that of the native protein. Particularly, some passive VPT microrheology measurements in native Mfp-1 coacervates triggered by NaCl, showed a viscosity of $6-12$ Pa·s at ph 5.5 compared to the 0.05 Pa·s for the recombinant Mfp-1 [95] under the same conditions. This represents an approximate 100-fold increase of viscosity in the measurements done on the native protein. Therefore, it would be important to compare the rheology of recombinant and native Mfp-1 samples to understand better the combined interaction upon the addition of chloride and sulfate anions in response to pH variations.

Additionally, while performing our OT experiments, we observed the formation of bubbles upon turning on the laser at high power, a reason why we decided to lower it during our measurements. We conjecture that this behavior is a response to laser-induced heating. Temperature is known to affect coacervation, and given that sea temperature is colder than our experimental conditions, it could be worth exploring the effects of temperature in Mfps coacervation as well. In fact, some Mfps have been shown to undergo coacervation as a result of a temperature change showing an upper critical temperature solution behavior (UCST), where phase separation occurs at temperatures below a particular critical temperature [97, 98]. Currently, some optical trap systems offer temperature control as they are used to work with cellular samples that require higher temperatures to be viable, a technical feature that can be expanded to study the temperature effect on Mfps coacervation while measuring their rheological properties.

Further, although we successfully introduced the use of optical tweezers based active microrheology to obtain relevant information of rMfp-1 condensates at microscale,

improvements in the method are still necessary to account for the magnitude scale differences when data is compared with video particle tracking microrheology. For instance, a detailed calibration using a well characterized viscoelastic material, such as a PEG hydrogel, instead of using a pure viscous solution would provide more information regarding the differences from the active and passive methods. Also, a deeper characterization of the detected signal at lower frequencies compared to the system noise floor could be useful to track the source of the apparent elastic plateau at lower frequencies in the magnitude response function, thus being able to subtract it from the final results afterwards.

Finally, the rediscovery of liquid-liquid phase separation in the context of intracellular interactions, has brought novel techniques using optical tweezers microrheology to study biomolecular condensates. By introducing OT-based microrheology to the study of extracellular Mfp condensates we can adapt those techniques to acquire more information about the byssus nature at microscale. For instance, besides the multiharmonic approach we showed here, there are techniques that make use of dual traps to measure surface tension of droplets in addition to the viscoelastic modulus, by squeezing a droplet using two beads and measuring the response to the forces involved [6], an approach that may be applied as well in the mechanical characterization of Mfps coacervate droplets. Being able to adapt these techniques to study the contents of the purified secretory vesicles remains a challenge due to their size ($\sim 2\mu m$), which hinders probe insertion. However, pursuing its achievement can lead to invaluable insights about the material properties of the precursor phases during storage, thus providing a better understanding of the physical and chemical forces that led to the byssus assembly.

4.2 The effect of microtubule acetylation on cell mechanics

4.2.1 Discussion

By applying a multiharmonic deformation to the cell's cytoplasm using optical tweezers, we measured the viscoelastic moduli of wild-type cells and compared it with cell overexpressing α-tat1, an acetylase that targets microtubules. We found our data to be well described by a dynamic crosslinking model [93], and to show a slight decrease in the magnitude of both, the storage and loss modulus, when cells expressed α-tat1. From the fits of our data to a dynamic crosslinking model, we detected a small shift in the crosslinking relaxation time from $k_{offWT} = 0.26s^{-1}$ to $k_{off+} = 0.46s^{-1}$ between the wildtype cells and the transfected sample, which can indicate a more fluid-like behavior in the acetylated state. However, our data set was small to be able to assert this difference as statistically significant. Interestingly, when comparing cells coming from a transfected sample, the dynamics was almost the same for cells not showing plasmid expression against those that show it, with the loss tangent depicting a slight shift across all the frequencies towards the fluid-like state for cells showing expression by fluorescence, indicating that these cells may be expressing low levels of alpha-tat1 not detected by fluorescence.

Following previous work [8, 93], our results concur with a mechanical model proposing that cell dynamics are governed by the transient binding of a dominant crosslink in the actin network. Furthermore, our estimated crosslinking relaxation time of $k_{offWT} = 0.26s^{-1}$ is in close agreement with previously measured rate of $k_{off} = 0.24s^{-1}$ for WT fibroblasts[8] suggesting that the crosslinking mechanism in both cells may be similar to one another. However, due to the large amount of cytoskeletal crosslinkers identified[100, 101], distinguishing the particular crosslink involved remains a challenge.

The elastic modulus in the fitted model scales with the density of crosslinks present in the sample [93]. Thus, if confirmed as significant, the slight decrease on the magnitude of the viscoelastic moduli in the hyperacetylated condition compared to the moduli of wildtype cells could suggest a decrease in the crosslinks density, maybe as a result of a higher microtubule flexibility.

Finally, we observed similar mechanics for all cells treated for transfection, regardless of whether expression of α-tat1 was observed by fluorescence. There are several possible explanations. First, a reduction of the experimental conditions variability that can potentially affect crosslinks binding, mainly the stress induced by the transfection procedure itself, could suggest that the previously observed shift in dynamics was a consequence of the experimental procedure rather than the hyperacetylation state. Secondly, it is possible that even though no fluorescence indicated the presence of the α-tat1 in cells, those cells analyzed had had a minimum α-tat1 expression which was enough to render the same dynamic response, thus suggesting that the threshold level for α-tat1 to affect the crosslink dynamics is very low. And thirdly, those results may indicate that indeed, hyperacetylation of microtubules does not significantly affect the dynamics of the cytoskeletal network measured using our microrheology technique. Future experiments will focus on analyzing the level of microtubule acetylation in these cells using antibodies specific for acetylated microtubules [102]. Because our optical tweezers microrheology approach probes the mechanical response locally, our measurements are more sensitive to local changes; however, as microtubules are long semiflexible filaments their increased flexibility due to acetylation could potentially affect more the bulk response of the cell to resist damage against loading forces, rather than being present as a local effect, unaffecting the binding dynamics, explaining why we do not observe significant differences in the dynamic behavior. Despite the similarity in dynamics, the loss tangent still suggest a softening of hyperacetylated cells across all the frequencies measured, which is compatible with the observation that acetylation reduces microtubule rigidity [87].

4.2.2 Future work

As the effects observed in our measurements are comparable with the variability of the samples, further improvements in the experiment protocol should be made to increase the efficiency in cell viability in order to assess the true significance of our results. Moreover, our lab has access to a variant of the α-tat1 plasmid, developed by our collaborator Klaus Hahn (UNC), which is linked to a light-sensitive LOV2 domain, such that the α-tat1 enzyme is inactive in the dark, but undergoes a conformational change to switch to an active state when is exposed to blue light [103]. Thus, use of this switchable protein could further reduce the experimental variability of the experiments by performing viscoelastic measurements using the same trapped-particle before, and after the activation of the α-tat1 enzyme. Nevertheless, a parallel method to induce acetylation should be considered as well to exclude the transfection process as the possible cause of the differences observed. For instance, we propose to use *tubacin*, a drug that increases α-tubulin acetylation by inhibition of the tubulin deacetylase (HDAC6) [104]. We expect that implementation of this considerations would provide more compelling results to elucidate the role of microtubule acetylation as a mechanism to regulate cell mechanics.

Chapter 5

Conclusions and summary

Understanding the dynamic mechanical response of biological samples to different stimuli could provide insights about their structure and functions, which can be harnessed to target potential malfunctions or to reproduce similar mechanisms synthetically for biomedical applications. Microrheology techniques offer a broad range of options to study biological materials as they provide measurements at their relevant spatial and temporal scales. In particular, for samples constituted of transiently crosslinked biopolymeric networks, the application of microrheology can provide information about their binding rates, which relate to the network rearrangement and their mechanical response to deformation. In this project, we demonstrate the applicability of video particle tracking and optical tweezers-based active microrheology to better understand mechanisms of mussel adhesion and cell mechanics regulation, where the crosslinks binding rates in the mussel protein molecules, and in the cell cytoskeleton biopolymers, can be tuned by certain stimuli to modulate the sample's mechanical behavior.

Marine mussels produce high performance polymeric fibers from fluid protein condensed phases to tightly anchor to underwater surfaces. Byssal fibers serve as an inspiring model in the design of underwater adhesives, self-healing materials and surface coating technologies. Despite being a broadly studied system, the fundamental mechanisms underlying the assembly from a fluid phase to a hierarchically structured material still remain elusive. In this work, we successfully introduced the use of optical tweezers-based microrheology as a new exploitable approach to study the physicochemical factors that

control the transition of these dense fluid phases into solid fibers. We highlighted the advantages of our method to investigate the dynamics of condensates across a wider frequency range, compared to previously used techniques to characterize mussel foot proteins. We also identified inconsistent elastic behaviors measured at low frequencies with the active technique that were addressed by using video particle tracking, thus illustrating the complementary nature of both approaches. By measuring the viscoelastic moduli of rMfp-1 condensates, we identified a synergy between sulfate anions and pH in controlling the viscoelasticity of rMfp-1 condensates, inducing higher viscosities with increasing pH, suggesting sulfate is a strong stimuli in the solidification process. Additionally, we found that chloride anions increased the condensate's viscosity mostly at seawater pH. In general, identification of these and other chemical triggers, and characterization of their effects in mussel foot proteins condensed phases, is specially valuable in the design and formulation of sustainable biomaterials. Thus, our study has relevance in both, understanding mussel byssus formation, and in broadening considerations of material design of mussel-inspired materials. Furthermore, we believe that optical tweezers based microrheology has also great potential to become a relevant tool in pursuing the mechanical characterization of condensate phases contained within secretory vesicles, which is currently lacking.

Moving froward, opposite to the measurements performed *in vitro*, we encountered many challenges to successfully asses the effect of microtubule acetylation in cell mechanics using optical tweezers-based microrheology, mainly arising from the cell treatments required in preparation for the experiments. Nevertheless, we successfully obtain viscoelastic moduli traces showing the dynamic crosslinking nature of the cell's cytoplasm in agreement with previous work [8], thus illustrating the consistency of the microrheology method itself. Although limited, our measurements hinted that microtubule acetylation possibly makes the cells slightly softer and increases its fluid-like behavior, which agrees with studies showing that acetylated microtubules are more flexible [87]. However, due to our high sample variability, our data is not sufficient to offer a final conclusion in

elucidating the role of microtubule acetylation as a cell mechanical regulator. Therefore, we propose further improvements in the experiment protocol, such as using an alternative methods to induce acetylation, to obtain more reliable information in this regard. Although experimentally challenging, pursuing a better understanding of cell mechanics and their mechanism of regulation is necessary, as understanding them better could help in the developing of treatments to target a broad range of diseases affecting the cell mechanical properties.

Overall, our project demonstrated the advantages and limitations arising when using passive and active microrheology to study two samples of distinct nature. We identified the different considerations to be taken ranging from the calibration models, to sample preparation, and were able to correlate our data measured *in vitro* to the biological relevant process of phase transition observed in mussel protein condensates. We proposed improvements in both studies performed that hopefully will contribute to gain new insights about these and more biological materials in the future.

Bibliography

[1] Malkin, A.Y. and Isayev, A.I. *Rheology: Concepts, Methods, and Applications*. 4th ed. Scarborough, Ontario: ChemTec Publishing, 2022.

[2] Gardel, Margaret L et al. "Mechanical response of cytoskeletal networks". *Methods in cell biology* 89 (2008), pp. 487–519.

[3] Hyman, Anthony A, Weber, Christoph A, and Jülicher, Frank. "Liquid-liquid phase separation in biology". *Annual review of cell and developmental biology* 30.1 (2014), pp. 39–58.

[4] Choi, Jeong-Mo, Holehouse, Alex S., and Pappu, Rohit V. "Physical Principles Underlying the Complex Biology of Intracellular Phase Transitions". *Annual Review of Biophysics* 49.Volume 49, 2020 (2020), pp. 107–133.

[5] Alshareedah, Ibraheem et al. "Programmable viscoelasticity in protein-RNA condensates with disordered sticker-spacer polypeptides". *Nature communications* 12.1 (2021), p. 6620.

[6] Jawerth, Louise M. et al. "Salt-Dependent Rheology and Surface Tension of Protein Condensates Using Optical Traps". *Phys. Rev. Lett.* 121 (25 Dec. 2018), p. 258101.

[7] Jawerth, Louise et al. "Protein condensates as aging Maxwell fluids". *Science* 370.6522 (2020), pp. 1317–1323.

[8] Chaubet, Loic et al. "Dynamic crosslinking of the actin cytoskeleton governs cell mechanics". *Biophysical Journal* 118.3 (2020), 280a–281a.

[9] Broedersz, Chase P. and MacKintosh, Fred C. "Modeling semiflexible polymer networks". *Rev. Mod. Phys.* 86 (3 July 2014), pp. 995–1036.

[10] Waite, J. Herbert. "Mussel adhesion – essential footwork". *Journal of Experimental Biology* 220.4 (Feb. 2017), pp. 517–530. URL: https://doi.org/10.1242/jeb.134056.

[11] Conti, Monica, Danese, Valeria, and Pata, Vittorino. "Aging of Viscoelastic Materials: A Mathematical Model". *Mathematical Modeling in Cultural Heritage*. Ed. by Bonetti, Elena et al. Cham: Springer International Publishing, 2021, pp. 135–146. URL: https://doi.org/10.1007/978-3-030-58077-3_9.

[12] Barnes, Howard A, Hutton, John Fletcher, and Walters, Kenneth. *An introduction to rheology*. Vol. 3. Elsevier, 1989.

[13] Tassieri, Manlio. *Microrheology with Optical Tweezers: Principles and Applications*. Singapore: Pan Stanford Publishing, 2016.

[14] Furst, Eric M. and Squires, Todd M. *Microrheology*. Oxford University Press, Oct. 2017. URL: https://doi.org/10.1093/oso/9780199655205.001.0001.

[15] Mezger, Thomas. *The Rheology Handbook. For users of rotational and oscillatory rheometers*. Hannover, Germany: Vincentz Network, 2020.

[16] Zhou, Huan-Xiang. "Viscoelasticity of biomolecular condensates conforms to the Jeffreys model". *The Journal of Chemical Physics* 154.4 (2021).

[17] Alberts, Bruce et al. *Molecular biology of the cell*. 6th ed. Garland Science, Taylor and Francis Group, 2015.

[18] Tanaka, F and Edwards, SF. "Viscoelastic properties of physically crosslinked networks. 1. Transient network theory". *Macromolecules* 25.5 (1992), pp. 1516–1523.

[19] Katashima, Takuya. "Molecular understanding of viscoelasticity in transient polymer networks based on multiple methods". *Nihon Reoroji Gakkaishi* 50.1 (2022), pp. 51–56.

[20] Green, Melville S and Tobolsky, Arthur V. "A new approach to the theory of relaxing polymeric media". *The Journal of chemical physics* 14.2 (1946), pp. 80–92.

[21] Tanaka, F. and Edwards, S.F. "Viscoelastic properties of physically crosslinked networks: Part 1. Non-linear stationary viscoelasticity". *Journal of Non-Newtonian Fluid Mechanics* 43.2 (1992), pp. 247–271.

[22] Tanaka, F and Edwards, SF. "Viscoelastic properties of physically crosslinked networks: Part 2. Dynamic mechanical moduli". *Journal of non-newtonian fluid mechanics* 43.2-3 (1992), pp. 273–288.

[23] Mao, Yating, Nielsen, Paige, and Ali, Jamel. "Passive and Active Microrheology for Biomedical Systems". *Frontiers in Bioengineering and Biotechnology* 10 (2022). URL: https://www.frontiersin.org/articles/10.3389/fbioe.2022.916354.

[24] Mason, T. G. and Weitz, D. A. "Optical Measurements of Frequency-Dependent Linear Viscoelastic Moduli of Complex Fluids". *Phys. Rev. Lett.* 74 (7 Feb. 1995), pp. 1250–1253.

[25] Gardel, M.L., Valentine, M.T., and Weitz, D.A. "Microrheology". *Microscale Diagnostic Techniques*. Ed. by Breuer, Kenneth S. Berlin, Heidelberg: Springer Berlin Heidelberg, 2005, pp. 1–49.

[26] Mason, Thomas G. "Estimating the viscoelastic moduli of complex fluids using the generalized Stokes–Einstein equation". *Rheologica acta* 39 (2000), pp. 371–378.

[27] Evans, RML et al. "Direct conversion of rheological compliance measurements into storage and loss moduli". *Physical Review E* 80.1 (2009), p. 012501.

[28] Tassieri, Manlio et al. "Microrheology with optical tweezers: data analysis". *New Journal of Physics* 14.11 (2012), p. 115032.

[29] Nichols, E. F. and Hull, G. F. "The Pressure Due to Radiation". *Proceedings of the American Academy of Arts and Sciences* 38.20 (1903), pp. 559–599. URL: `http://www.jstor.org/stable/20021808` (visited on 07/31/2024).

[30] Ashkin, A. "Acceleration and Trapping of Particles by Radiation Pressure". *Phys. Rev. Lett.* 24 (4 Jan. 1970), pp. 156–159.

[31] Ashkin, A. et al. "Observation of a single-beam gradient force optical trap for dielectric particles". *Opt. Lett.* 11.5 (May 1986), pp. 288–290.

[32] NobelPrize.org. *The Nobel prize in physics 2018. Tools made of light*. URL: `https://www.nobelprize.org/nobel-prizes-2018/` (visited on 01/25/2024).

[33] Gieseler, Jan et al. "Optical tweezers — from calibration to applications: a tutorial". *Adv. Opt. Photon.* 13.1 (Mar. 2021), pp. 74–241.

[34] Magazzù, Alessandro and Marcuello, Carlos. "Investigation of Soft Matter Nanomechanics by Atomic Force Microscopy and Optical Tweezers: A Comprehensive Review". *Nanomaterials* 13.6 (2023). URL: `https://www.mdpi.com/2079-4991/13/6/963`.

[35] Bustamante, Carlos J. et al. "Optical tweezers in single-molecule biophysics". *Nature Reviews Methods Primers* 1 (2021).

[36] Koch, Matthias D. and Shaevitz, Joshua W. "Introduction to Optical Tweezers". *Optical Tweezers: Methods and Protocols*. Ed. by Gennerich, Arne. New York, NY: Springer New York, 2017, pp. 3–24.

[37] Mizuno, Daisuke et al. "Active and passive microrheology in equilibrium and nonequilibrium systems". *Macromolecules* 41.19 (2008), pp. 7194–7202.

[38] Matellan, Carlos and Río Hernández, Armando E. del. "Where No Hand Has Gone Before: Probing Mechanobiology at the Cellular Level". *ACS Biomaterials Science & Engineering* 5.8 (2019), pp. 3703–3719.

[39] MacKintosh, F.C. and Schmidt, C.F. "Microrheology". *Current Opinion in Colloid & Interface Science* 4.4 (1999), pp. 300–307.

[40] Mahaffy, R. E. et al. "Scanning Probe-Based Frequency-Dependent Microrheology of Polymer Gels and Biological Cells". *Phys. Rev. Lett.* 85 (4 July 2000), pp. 880–883.

[41] Li, Yiran and Cao, Yi. "The molecular mechanisms underlying mussel adhesion". *Nanoscale Adv.* 1 (11 2019), pp. 4246–4257.

[42] Lee, Bruce P et al. "Mussel-inspired adhesives and coatings". *Annual review of materials research* 41.1 (2011), pp. 99–132.

[43] Amstad, Esther and Harrington, Matthew J. "From vesicles to materials: bioinspired strategies for fabricating hierarchically structured soft matter". *Philosophical Transactions of the Royal Society A* 379.2206 (2021), p. 20200338.

[44] Holten-Andersen, Niels et al. "Metals and the integrity of a biological coating: the cuticle of mussel byssus". *Langmuir* 25.6 (2009), pp. 3323–3326.

[45] Waite, J Herbert. "Adhesion in byssally attached bivalves". *Biological Reviews* 58.2 (1983), pp. 209–231.

[46] Harrington, Matthew J, Jehle, Franziska, and Priemel, Tobias. "Mussel byssus structure-function and fabrication as inspiration for biotechnological production of advanced materials". *Biotechnology journal* 13.12 (2018), p. 1800133.

[47] Yu, Jing et al. "Mussel protein adhesion depends on interprotein thiol-mediated redox modulation". *Nature chemical biology* 7.9 (2011), pp. 588–590.

[48] Guo, Qi et al. "Hydrogen-bonds mediate liquid-liquid phase separation of mussel derived adhesive peptides". *Nature Communications* 13.1 (2022), p. 5771. URL: https://doi.org/10.1038/s41467-022-33545-w.

[49] Harrington, Matthew J, Mezzenga, Raffaele, and Miserez, Ali. "Fluid protein condensates for bio-inspired applications". *Nature Reviews Bioengineering* 2.3 (2024), pp. 260–278.

[50] Renner-Rao, Max et al. "Mussels fabricate porous glues via multiphase liquid–liquid phase separation of multiprotein condensates". *ACS nano* 16.12 (2022), pp. 20877–20890.

[51] Gomes, Edward and Shorter, James. “The molecular language of membraneless organelles”. *Journal of Biological Chemistry* 294.18 (2019), pp. 7115–7127.

[52] Flory, Paul J. “Thermodynamics of high polymer solutions”. *The Journal of chemical physics* 10.1 (1942), pp. 51–61.

[53] Menger, Fredric M. and Sykes, Bridget M. “Anatomy of a Coacervate”. *Langmuir* 14.15 (1998), pp. 4131–4137.

[54] Astoricchio, Emanuele et al. “The wide world of coacervates: from the sea to neurodegeneration”. *Trends in biochemical sciences* 45.8 (2020), pp. 706–717.

[55] Michieletto, Davide and Marenda, Mattia. “Rheology and viscoelasticity of proteins and nucleic acids condensates”. *JACS Au* 2.7 (2022), pp. 1506–1521.

[56] Abbas, Manzar et al. “Peptide-based coacervates as biomimetic protocells”. *Chem. Soc. Rev.* 50 (6 2021), pp. 3690–3705. URL: https://doi.org/10.1039/D0CS00307G.

[57] Renner-Rao, Max, Clark, Madelyn, and Harrington, Matthew J. “Fiber Formation from Liquid Crystalline Collagen Vesicles Isolated from Mussels”. *Langmuir* 35.48 (2019), pp. 15992–16001.

[58] Jehle, Franziska et al. “Hierarchically-structured metalloprotein composite coatings biofabricated from co-existing condensed liquid phases”. *Nature communications* 11.1 (2020), p. 862.

[59] Harrington, Matthew J. et al. “Iron-Clad Fibers: A Metal-Based Biological Strategy for Hard Flexible Coatings”. *Science* 328.5975 (2010), pp. 216–220.

[60] Kim, Sangsik et al. “Salt triggers the simple coacervation of an underwater adhesive when cations meet aromatic π electrons in seawater”. *ACS nano* 11.7 (2017), pp. 6764–6772.

[61] Zeng, Hongbo et al. “Strong reversible Fe¡sup¿3+¡/sup¿-mediated bridging between dopa-containing protein films in water”. *Proceedings of the National Academy of Sciences* 107.29 (2010), pp. 12850–12853.

[62] Liu, Yalin, Winter, H. Henning, and Perry, Sarah L. “Linear viscoelasticity of complex coacervates”. *Advances in Colloid and Interface Science* 239 (2017). Complex Coacervation: Principles and Applications, pp. 46–60.

[63] Krogsgaard, Marie, Nue, Vicki, and Birkedal, Henrik. “Mussel-Inspired Materials: Self-Healing through Coordination Chemistry”. *Chemistry – A European Journal* 22.3 (2016), pp. 844–857.

[64] Zhao, Yong-Yan et al. “Mussel-Inspired Polydopamine Coating for Flexible Ternary Resistive Memory”. *Chemistry – An Asian Journal* 13.13 (2018), pp. 1744–1750.

[65] Mesko, Mihai et al. “Catechol-vanadium binding enhances cross-linking and mechanics of a mussel byssus coating protein”. *Chemistry of Materials* 33.16 (2021), pp. 6530–6540.

[66] Valentine, MT et al. “Colloid surface chemistry critically affects multiple particle tracking measurements of biomaterials”. *Biophysical journal* 86.6 (2004), pp. 4004–4014.

[67] Schindelin, Johannes et al. “Fiji: an open-source platform for biological-image analysis”. *Nature methods* 9.7 (2012), pp. 676–682.

[68] Tinevez, Jean-Yves et al. “TrackMate: An open and extensible platform for single-particle tracking”. *Methods* 115 (2017), pp. 80–90.

[69] Ershov, Dmitry et al. “TrackMate 7: integrating state-of-the-art segmentation algorithms into tracking pipelines”. *Nature Methods* 19.7 (2022), pp. 829–832.

[70] Inc., The MathWorks. *MATLAB version: 9.10.0.2198249 (R2021a)*. Natick, Massachusetts, United States, 2024. URL: `https://www.mathworks.com`.

[71] Evans, R Mike L. *moduli.m*. URL: `https://sites.google.com/site/rmlevans/home/rheology/moduli-m` (visited on 02/01/2024).

[72] Hendricks, Adam G and Goldman, Yale E. “Measuring molecular forces using calibrated optical tweezers in living cells”. *Optical Tweezers: Methods and Protocols* (2017), pp. 537–552.

[73] Cohen, Ora T and Hendricks, Adam G. “Two dominant timescales of cytoskeletal crosslinking in the viscoelastic response of the cytoplasm”. *Physical Review Research* 4.4 (2022), p. 043167.

[74] Sheely, Madison L. “Glycerol Viscosity Tables”. *Industrial & Engineering Chemistry* 24.9 (1932), pp. 1060–1064.

[75] Ghosh, Archishman, Kota, Divya, and Zhou, Huan-Xiang. “Shear relaxation governs fusion dynamics of biomolecular condensates”. *Nature communications* 12.1 (2021), p. 5995.

[76] Wu, Pei-Hsun et al. “A comparison of methods to assess cell mechanical properties”. *Nature methods* 15.7 (2018), pp. 491–498.

[77] Moeendarbary, Emad and Harris, Andrew R. "Cell mechanics: principles, practices, and prospects". *WIREs Systems Biology and Medicine* 6.5 (2014), pp. 371–388.

[78] Howard, Jonathon. *Mechanics of motor proteins and the cytoskeleton*. Sunderland, Massachusetts: Sinauer Associates, 2001.

[79] Suresh, S. et al. "Reprint of: Connections between single-cell biomechanics and human disease states: gastrointestinal cancer and malaria". *Acta Biomaterialia* 23 (2015), S3–S15.

[80] Alibert, Charlotte, Goud, Bruno, and Manneville, Jean-Baptiste. "Are cancer cells really softer than normal cells?" *Biology of the Cell* 109.5 (2017), pp. 167–189.

[81] Weber, Andreas et al. "Microtubule disruption changes endothelial cell mechanics and adhesion". *Scientific Reports* 9.1 (2019), p. 14903.

[82] Robison, Patrick and Prosser, Benjamin L. "Microtubule mechanics in the working myocyte". *The Journal of physiology* 595.12 (2017), pp. 3931–3937.

[83] Seetharaman, Shailaja et al. "Microtubules tune mechanosensitive cell responses". *Nature Materials* 21.3 (2022), pp. 366–377.

[84] Janke, Carsten and Chloë Bulinski, Jeannette. "Post-translational regulation of the microtubule cytoskeleton: mechanisms and functions". *Nature reviews Molecular cell biology* 12.12 (2011), pp. 773–786.

[85] Brouhard, Gary J and Rice, Luke M. "Microtubule dynamics: an interplay of biochemistry and mechanics". *Nature reviews Molecular cell biology* 19.7 (2018), pp. 451–463.

[86] Roll-Mecak, Antonina. "The tubulin code in microtubule dynamics and information encoding". *Developmental cell* 54.1 (2020), pp. 7–20.

[87] Portran, Didier et al. "Tubulin acetylation protects long-lived microtubules against mechanical ageing". *Nature Cell Biology* 19 (2017), pp. 391–398.

[88] Xu, Zhenjie et al. "Microtubules acquire resistance from mechanical breakage through intralumenal acetylation". *Science* 356.6335 (2017), pp. 328–332.

[89] Li, Lin and Yang, Xiang-Jiao. "Tubulin acetylation: responsible enzymes, biological functions and human diseases". *Cellular and molecular life sciences* 72 (2015), pp. 4237–4255.

[90] Janke, Carsten and Montagnac, Guillaume. "Causes and consequences of microtubule acetylation". *Current Biology* 27.23 (2017), R1287–R1292. URL: https://doi.org/10.1016/j.cub.2017.10.044.

[91] Dogterom, Marileen and Koenderink, Gijsje H. "Actin–microtubule crosstalk in cell biology". *Nature reviews Molecular cell biology* 20.1 (2019), pp. 38–54.

[92] Nekooki-Machida, Yoko and Hagiwara, Haruo. "Role of tubulin acetylation in cellular functions and diseases". *Medical molecular morphology* 53.4 (2020), pp. 191–197.

[93] Lieleg, O et al. "Transient binding and dissipation in cross-linked actin networks". *Physical review letters* 101.10 (2008), p. 108101.

[94] Pappu, Rohit V. et al. "Phase Transitions of Associative Biomacromolecules". *Chemical Reviews* 123.14 (2023). PMID: 36881934, pp. 8945–8987.

[95] Kim, Hyungbin et al. "Essential Role of Thiols in Maintaining Stable Catecholato-Iron Complexes in Condensed Materials". *Chemistry of Materials* 34.11 (2022), pp. 5074–5083.

[96] Ghosh, Archishman and Zhou, Huan-Xiang. "Determinants for Fusion Speed of Biomolecular Droplets". *Angewandte Chemie International Edition* 59.47 (2020), pp. 20837–20840.

[97] Wang, Jia and Scheibel, Thomas. "Coacervation of the Recombinant Mytilus galloprovincialis Foot Protein-3b". *Biomacromolecules* 19.9 (2018). PMID: 30071727, pp. 3612–3619.

[98] Yang, Byeongseon et al. "Coacervation of Interfacial Adhesive Proteins for Initial Mussel Adhesion to a Wet Surface". *Small* 14.52 (2018), p. 1803377.

[99] Valois, Eric, Mirshafian, Razieh, and Waite, J. Herbert. "Phase-dependent redox insulation in mussel adhesion". *Science Advances* 6.23 (2020), eaaz6486.

[100] Dos Remedios, C. G. et al. "Actin Binding Proteins: Regulation of Cytoskeletal Microfilaments". *Physiological Reviews* 83.2 (2003). PMID: 12663865, pp. 433–473.

[101] Mohan, Renu and John, Annie. "Microtubule-associated proteins as direct crosslinkers of actin filaments and microtubules". *IUBMB Life* 67.6 (2015), pp. 395–403.

[102] Balabanian, Linda, Berger, Christopher L, and Hendricks, Adam G. "Acetylated microtubules are preferentially bundled leading to enhanced kinesin-1 motility". *Biophysical journal* 113.7 (2017), pp. 1551–1560.

[103] Lungu, Oana I et al. “Designing photoswitchable peptides using the AsLOV2 domain”. *Chemistry & biology* 19.4 (2012), pp. 507–517.

[104] Haggarty, Stephen J et al. “Domain-selective small-molecule inhibitor of histone deacetylase 6 (HDAC6)-mediated tubulin deacetylation”. *Proceedings of the National Academy of Sciences* 100.8 (2003), pp. 4389–4394.